New phenomenon in the Gulf of Guinea sheds light on 70 year old mystery

Dissertation

with the aim of achieving a doctoral degree

at the Faculty of Mathematics, Informatics and Natural Sciences

Department of Earth Sciences

at Universität Hamburg

submitted by

Charlotte Bruland

Hamburg, 2022

Department of Earth Sciences

Date of Oral Defense:	01.07.2022
Reviewers:	Prof. Dr. Celine Hadziioannou
	Dr. Laurent Stehly
Members of the examination commission:	Chair Prof. Dr Celine Hadziioannou
	Dr. Laurent Stehly
	PD Dr. Thomas Pohlmann
	Dr. Lea Scharff
	Prof. Dr. Gerhard Schmiedl

Chair of the Subject Doctoral Committee Earth System Sciences:	Prof. Dr. Hermann Held
Dean of Faculty MIN:	Prof. Dr. Heinrich Graener

Eidesstattliche Versicherung | Declaration on Oath

Hiermit erkläre ich an Eides statt, dass ich die vorliegende Dissertationsschrift selbst verfasst und keine anderen als die angegebenen Quellen und Hilfsmittel benutzt habe.

|

I hereby declare upon oath that I have written the present dissertation independently and have not used further resources and aids than those stated.

Ort,den | City,date

Unterschrift | Signature

Preface

This thesis is based on two manuscripts; one submitted, one in preparation. The first paper, titled "Gliding tremors from the Gulf of Guinea shed light on 70 year old mystery" is on the discovery of globally observed gliding tremors originating in the Gulf of Guinea and potential source mechanisms. It is in revision with Communications Earth & Environment. The second manuscript, "New insights into the source mechanism for the 26 s microseism from three component beamforming" is on the wavetypes radiated, seasonal variation, location and temporal evolution of the seismic sources using 3-C beamforming and focuses on the physical source mechanisms of the 26 s microseism. It is currently in preparation for submission to Earth and Planetary Science Letters.

Part of the code used was written in previous projects by Sarah Mader and Carina Juretzek and was adapted for this study. Processing of 4 months of data from the Morocco array was carried out by Sarah Mader. The matched field processing is carried out by Sven Schippkus. Any other code, processing, analysis and interpretation is done by C.B.

Acknowledgements

First, I would like to thank my supervisor, Celine Hadziioannou, for inspiration and guidance. I am grateful to Joachim Wassermann, Éléonore Stutzmann, Lise Retailleau, Christoph Sens-Schönfelder, Torsten Dahm and Stephen McNutt for helpful discussions and comments. I would also like to thank Stefan Kern for assisting with satellite data. To my family and friends, thank you for the motivation and support.

New phenomenon in the Gulf of Guinea sheds light on 70 year old mystery

Charlotte Bruland

Abstract

More than 70 years ago, seismologists discovered 26 second signal that can be detected on seismic stations almost globally. The signal is excited seemingly continuously from an area in the Gulf of Guinea. Even after 70 years, we still don't know what is causing this 26 second signal or what physical mechanism is responsible for it. We investigate its evolution, and discover that energetic bursts of higher amplitude in the 26 s signal are often accompanied by a spectral glide effect. We apply array methods to constrain the source location and wave types of the sustained seismic signals, and find that the source of both signal types excites Love and Rayleigh waves and are connected spatially, with a fixed source location. The gliding tremor has a very low frequency onset, lasts for days and is extremely repeatable. Similar to the 26 s microseism, the glides are occasionally so strong they can be detected almost globally. The gliding tremor reminds us of signals detected close to active volcanoes. After careful consideration of different oceanic and volcanic mechanisms, we propose a combined source mechanism for the gliding and continuous tremor, of a hydrothermal system consisting of a layered structure or channel with a resonance period of 26 s. The channel is sealed off by a fractured plug that acts as valve through which gas can escape intermittently, thereby producing pressure pulses with a repetition period stabilized by the resonance of the channel. However, the low frequency, decades long duration that these phenomena appear to have been active and the repeatability of the glides cannot be explained by known volcanic tremor mechanisms. This points towards the need to view tremor in a new way. Since volcanic tremor is an important tool for monitoring volcanic activity, our discovery may affect future forecasting of activity at volcanoes.

Contents

List of Figures

1 Introduction

In addition to earthquakes, seismometers all around the world continuously record faint vibrations. This is known as ambient seismic noise. Before, seismic noise was viewed as an obstacle, standing in the way of detecting the seismic signals from earthquakes or other impulsive sources. Today, it has become a useful tool to probe the internal structure of the Earth without the need for earthquakes or active sources. Let us start by taking a closer look at a seismic noise record for 5 days from a station in Africa (Figure 1).

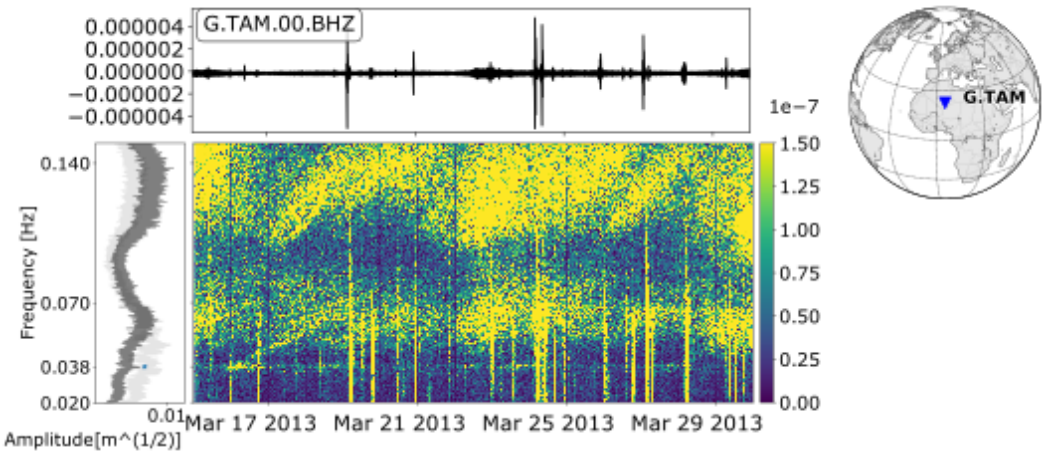

Figure 1: Seismic noise recorded by TAM (Algeria) a seismic station in the GEOSCOPE network represented in time (top panel), frequency (left panel) and frequency over time (main panel). In light grey and darker grey we have the spectral amplitude before and after earthquake removal, respectively. In addition to the two broad peaks that dominate the spectra, we also see a narrow peak at 0.038 Hz (blue dot), which can also be spotted as a horizontal line in the spectrogram. This signal is known as the 26 s microseism and can be detected on seismic stations globally.

Figure 1 shows the seismic noise recorded on the vertical component on station TAM. The top panel shows the seismic trace in time, the bottom left panel displays the amplitude spectrum, for frequencies in the range between 0.02 and 0.15 Hz, while the bottom right shows the frequency content over time, called a spectrogram. The vertical yellow lines in the spectrogram, starting at low frequencies, are earthquakes, which correspond to the spikes in the seismic trace at the same time. Looking at the variation in frequency content reveals many different signals hidden in the ambient noise. These signals carry information about the sources that generate them.

The amplitude spectrum for the seismic trace after removing the earthquakes is shown in dark grey (with earthquakes in light grey). In this frequency band, seismic noise is mainly generated by ocean waves, called ocean microseisms. Microseisms are characterized by the two bumps in the ambient noise spectrum. In addition to the two broadband peaks, there is also a narrowband peak at lower frequencies, which appears as a horizontal line in the spectrogram. The very low frequencies (below about 0.05 Hz) of the ambient noise spectrum is the part we know the least about. The peak at 0.038 Hz or 26 s, is called the '26 s microseism'. It is believed to be generated continuously from a fixed location for the past 70 years, and can be detected on seismic stations globally. Both oceanic and volcanic origin have been proposed, but no known physical mechanisms can explain the signal. The generation mechanism of the 26 microseism remains one of the unsolved mysteries in modern seismology, and is the main focus of this work.

Persistent localized sources, such as the 26 s source, can affect the outcome of ambient noise-based methods, but also have potential for imaging the subsurface. Knowing where seismic noise sources are located and how they behave can help us understand the processes and physical mechanisms driving them and improve applications of ambient noise. In this work, we investigate the location, characteristics and evolution over time of the 26 s signal. We discover a repeatable, long duration and very low frequency gliding tremor associated with the 26 s source, which resembles gliding volcanic tremor observed leading up to volcanic eruptions. We can see an example of a glide around May 17th 2013 in the spectrogram in Figure 1. The tremor occurs at a frequency that is too low to be explained by the common volcanic or hydrothermal tremor mechanisms, and points towards a phenomenon that occurs on a large spatial scale. This highlights the gap in knowledge of very long period seismic signals. The strong repeatability of the gliding tremor, its very low frequency range, and the decades-long timescales where this phenomenon seems to have been active all point towards the need to view tremor in a new way. Since volcanic tremor is an important tool for monitoring volcanic activity, this discovery may affect future forecasting of activity at volcanoes.

This section provides an introduction to the main concepts of ambient noise, including ocean microseism generation and ambient noise applications, the 26 s microseism and volcanic tremor. First we provide a brief overview of how seismic noise is generated and its applications. This is followed by an introduc-

tion of the 26 s microseism, including geological setting, and historical overview and the accompanying gliding tremor. Then volcanic tremor characteristics and generation mechanisms are explained. Lastly, the main research objectives are presented together with the thesis outline.

1.1 Ambient noise

Different sources can excite seismic waves. Short period noise (above 1 Hz) is generally related to human activity. At long periods (below 1 Hz), ambient noise is mainly generated by natural sources. Here, we focus on the seismic noise with frequencies between 1 mHz and 1 Hz, which is the frequency band of the seismic hum and the ocean microseisms. The amplitude and frequency of the long period noise varies with the seasons, with higher amplitudes and lower frequencies in northern hemisphere winter. In the summer, the amplitudes we observe are lower and the frequency content tends to be higher [Stutzmann et al., 2009]. The ambient noise wave field is dominated by surface waves, but it also consists of a smaller contribution of body waves [Toksöz and Lacoss, 1968].

1.1.1 Source mechanisms of ambient noise

As wind blows over oceans, the wind generates gravity waves that couple into the water column. The energy is then transmitted into the ocean floor and converted into elastic waves travelling along the water-sediment interface.[Ebeling, 2012] The relationship between storms, ocean waves and microseisms is studied by different authors [Bernard, 1990, Wijesekera et al., 2010, Hadziioannou et al., 2012, Tanimoto, 2013, Meschede et al., 2017, Retailleau and Gualtieri, 2019, Fan et al., 2019]. Although these microseisms have low amplitudes, they are detected at any time in any location on Earth. The amplitude varies for different locations. In Figure 2, we consider an example of a typical seismic noise spectrum.

Figure 2 shows the seismic noise spectrum for the vertical component at the seismic station SANAE from Ebeling [2012]. The dashed lines show the new low noise model and the new high noise model, which represent to the minimum noise levels from quiet periods at continental seismic stations around the world and maximum noise levels from mainly island stations. The two peaks that dominate the seismic noise spectrum are referred to as the primary and secondary microseism. The weaker primary

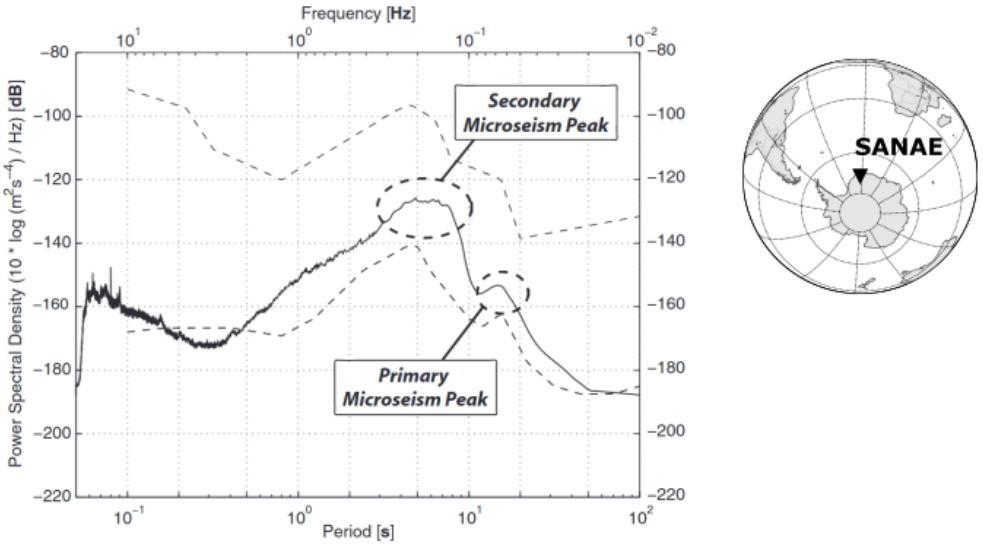

Figure 2: Typical ambient noise spectrum from Ebeling [2012] Mean power spectral density for vertical component of one month of data on SANAE seismic station April 2005. The spectrum is dominated by two broad peaks, called microseisms. The dotted lines represent high noise and low noise model from Peterson 1993.

microseism has frequencies between 0.02 to 0.1 Hz, while the secondary microseism has its peak between 0.1 and 1 Hz [Nishida, 2017]. The two peaks have different generation mechanisms, which explains the difference in amplitude and frequency.

Secondary microseism is generated when ocean waves of the same frequency propagating in opposite directions collide. This produces a standing wave that travels vertically towards the seafloor. When it couples into the seafloor, it generates seismic waves with double the frequency as the ocean waves we started with. Therefore it is also known as the double frequency microseism. A cartoon of its generation mechanism is shown in Figure 3a). Primary microseisms are generated directly from the non linear coupling between the ocean waves and the sea floor, as the ocean waves approach shallow water. The seismic waves generated by this mechanism have the same frequency as the ocean waves. An illustration of this mechanism is shown in Figure 3b). Ocean waves have a central period around 15 s over open oceans [Pierson Jr and Moskowitz, 1964]. Longer periods are associated with higher wind speeds [Pierson Jr and Moskowitz, 1964].

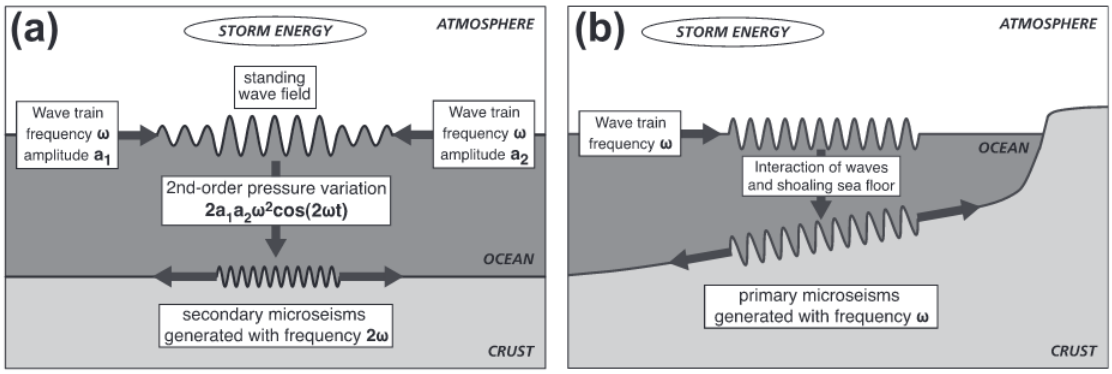

Figure 3: Microseism generation mechanisms from Ebeling [2012]: a) Secondary microseisms are generated when ocean waves of the same frequency travelling in opposite directions cross, producing a standing wave travelling vertically downwards and couples into the sea floor generating seismic waves with twice the frequency of the ocean waves responsible for its generation. b) Primary microseisms are generated from the nonlinear coupling of ocean wave energy into the sea floor as ocean waves approach shallow water. The resulting seismic waves have the same frequency as the ocean waves that generate them.

The theory of secondary microseism generation

The theory of secondary microseism generation is mainly based on the work of Longuet-Higgins [1950]. Here we present a brief overview of the theory based on a summary from Ebeling [2012]. We use a two coordinate system of horizontal and vertical coordinates x and z, where z is positive in the downward direction and measured from the mean of the ocean surface. We assume an incompressible ocean. Then the relation between pressure and potential and kinetic energies per unit volume can be written as the Bernoulli equation

$$\frac{p - p_s}{\rho} - gz = \frac{\partial \phi}{\partial t} - \frac{1}{2}(u^2 + w^2) + \theta(t) \tag{1}$$

Here p and p_s is the pressure and pressure at the free surface, respectively, ρ is the density of the fluid, g the gravitational acceleration, ϕ is the potential of the velocity u and contains a function of time t. $\theta(t)$ is the variation in pressure with t, while (u, w) are the velocity components. The velocity components can be written as $u = -\partial\phi/\partial x$ and $w = -\partial\phi/\partial z$.

Since ϕ, u and w diminish exponentially when increasing z in deep water approximation, the terms

containing these variable disappear at the sea floor. Then the previous equation can be simplified as

$$\frac{p - p_s}{\rho} - gz = \theta(t) \tag{2}$$

The pressure variation $\theta(t)$ at infinite depth can be expressed as

$$\theta(t) = \frac{1}{\lambda}\frac{\partial^2}{\partial t^2}\int_0^\lambda \frac{1}{2}\zeta(x,t)^2 dx \tag{3}$$

for periodic motion in the horizontal direction. Here, the wavelength is expressed as λ, $\zeta(x,t)$ the ocean surface elevation. For two ocean gravity waves with the same wavelength and period propagate in opposite directions in water with a constant depth, $\zeta(x,t)$ can be written as

$$\zeta(x,t) = a_1 \cos(kx - \omega t) + a_2 \cos(kx + \omega t) \tag{4}$$

The wavelength and period is related to the ocean depth through the dispersion relation given by $\omega^2 = gk\tanh(kh)$. When these two waves travelling in opposite directions cross paths, we get

$$\frac{\overline{p_h} - p_s}{\rho} - gh = -2a_1 \cos(kx - \omega t) + a_2 \cos(kx + \omega t) \tag{5}$$

where $\overline{p_h}$ represents the resulting mean pressure at the ocean bottom. By setting either a_1 or a_2 equal to zero, we consider a single propagating ocean gravity wave. In this case the pressure on the seafloor is constant. We get a standing wave when a_1 and a_2 are the same. The second-order pressure variations depend on the wavelength and direction of the two wave trains. When they are not in direct opposition, the generated pressure field decreases quickly as the angle between the wave trains increases. The amplitude of the second-order pressure variation on the sea floor is proportional to the product of the wave train amplitudes and it has a frequency of twice that of the crossing wave trains. Secondary microseisms are generated in deep waters as well as shallow.

The theory of primary microseism generation

The generation of primary microseism was proposed by Hasselmann [1963]. The wavelength of propagating surface gravity waves in deep water, can be approximated by $\lambda_\infty = gT^2/2\pi$, in which g is the gravitational acceleration and T is the wave period. Since ocean waves decay exponentially with depth, primary microseisms are limited to shallow water depths. As ocean waves approach shallow water, the ocean waves can interact directly with the sea floor, which is when the water depth D is less than about half of the wavelength.

Hasselmann [1963] demonstrated that the bottom pressure power spectral density scales linearly with the constant seafloor slope s. The wave induced pressure power spectrum for any bottom depth profile only assuming constant depth in the y direction, is given by Ardhuin et al. [2015]

$$F_{p,1}(k_x = 0, k_y = 0, f) = s\frac{\rho_\omega^2 g^4 [E_A(f, \theta_n) + E_A(f, \theta_n + \pi)]}{k_A (2\pi f)^4 3200 \times L_x} \tag{6}$$

where s is the effective slope containing the effects of bottom topography and is dependent on the depth profile and wave frequency of the ocean surface gravity waves f. k_x and k_y are the cross shore and along shore wave number components of the ocean surface gravity waves. θ_n represents the local shore-normal direction and Lx the length over which the spectrum is evaluated. $E_A(f, \theta)$ is the frequency direction dependent ocean wave energy spectral density for a water depth D_A for ocean waves travelling in directions normal to the coast. The wave field is normalized to a reference ocean wave amplitude for the reference water depth set to $D_A = 4000m$, with the corresponding wavenumber k_A and frequency f, related by the dispersion relation for linear ocean waves over a flat bottom

$$(2\pi f)^2 = g k_A \tanh(k_A D_A). \tag{7}$$

The seismic hum

At lower frequencies (1-20 mHz) we find the 'seismic hum'[Nishida, 2017]. The hum is the part of the seismic noise spectrum that we know the least about. As for microseisms, the amplitude of the hum correlates with the ocean swell that reaches the coast, with climate and varies with the seasons [Bromirski, 2009, Aster et al., 2008, 2010].

Below 20 mHz, ocean infragravity waves can reach the deep ocean floor. Watada and Masters [2001] observed that ocean infragravity waves can excite seismic hum. Comparing the source regions with an ocean wave model, showed that the dominant sources are ocean infragravity waves [Rhie and Romanowicz, 2004, 2006, Traer et al., 2012, Bromirski and Gerstoft, 2009]. The sources can be represented by a random shear traction at the seafloor due to topographic coupling between the ocean infragravity waves and the background seismic surface waves[Fukao et al., 2010, Nishida et al., 2008, Saito, 2010]. Ardhuin et al. [2015] showed quantitatively for Rayleigh waves that the seismic hum can be explained by the same mechanism as primary microseism.

Below 5 mHz, the spectrum shows two peaks at 3.7 mHz and 4.4 mHz. The peaks in the spectrum of the seismic hum can be explained by acoustic resonance between Rayleigh waves propagating in the subsurface and low frequency acoustic waves in the atmosphere [Watada and Kanamori, 2010]. This suggests that below 5 mHz, also atmospheric sources play a role in exciting the seismic hum [Kobayashi and Nishida, 1998, Tanimoto, 1999, Fukao et al., 2002].

Source locations of ocean microseisms

The sources of secondary microseisms are located both in shallow coastal areas and pelagic areas. Globally, strong sources are located in the North Pacific from July to September and the Antarctic ocean from December to February Hillers et al. [2012], Landès et al. [2010], gal. On local and regional scales, these source locations are correlated with storm activity [Kedar et al., 2008, Ardhuin et al., 2011, Hillers et al., 2012, Obrebski et al., 2013, Stutzmann et al., 2012, Gualtieri et al., 2013, Ardhuin et al., 2015, Neale et al., 2017]. Below 0.2 Hz, sources are mainly located in coastal areas. Above 0.2 Hz, the sources are mainly located in pelagic areas [Bromirski et al., 2005].

The sources of primary microseism are mainly located in shallow coastal areas [Cessaro, 1994, Friedrich et al., 1998, Traer et al., 2012, Cessaro and Chan, 1989, Haubrich and McCamy, 1969, Juretzek and Hadziioannou, 2016] This is the case for both Love and Rayleigh waves. In Europe, the strongest source area is in the near-shore region of the North Atlantic ocean [Cessaro, 1994, Friedrich et al., 1998, Juretzek and Hadziioannou, 2016, Kimman et al., 2012]. Strong sources in the North Atlantic can even be detected in Japan [Matsuzawa et al., 2012]. Other major sources of microseism activity are located at the west coast of North America, Polynesia and in the South Pacific [Cessaro, 1994, Traer et al., 2012].

For the seismic hum, dominant sources are located in the North Pacific Ocean from July to September, and in the Antarctic ocean from December to February [Rhie and Romanowicz, 2004, Nishida et al., 2008, Traer et al., 2012, Kurrle and Widmer-Schnidrig, 2006, Bromirski and Gerstoft, 2009].
Most studies indicate that the dominant sources are in shallow coastal areas [Rhie and Romanowicz, 2006, Traer et al., 2012, Bromirski and Gerstoft, 2009], while others propose that the sources are distributed on the deep sea-floor [Nishida and Fukao, 2007]. Stronger sources are located in coastal areas, while weaker sources are distributed on the deep seafloor.

1.1.2 Ambient noise applications

Since the seismic ambient field holds information about the interactions between the atmosphere, the oceans and the solid earth, it can also be used for climate studies [Bernard, 1990, Grevemeyer et al., 2000, Gualtieri et al., 2018]. Seismic observations have been linked to oceanic observations, as deep ocean temperature variations [Woolfe et al., 2015], sea levels and wave activity [Bromirski, 2009] and can be used to track major storms [Davy et al., 2014].

Studying ambient noise has become a common tool to obtain information about the Earth. Through cross-correlation of ambient noise records we can retrieve information about the subsurface [Shapiro and Campillo, 2004, Sabra et al., 2005a], including imaging the Earth structure through surface wave tomography [Sabra et al., 2005b, Stehly et al., 2009]. It has also been applied for imaging and monitoring in exploration [Bussat and Kugler, 2011, Mordret et al., 2013, De Ridder et al., 2014]. Ambient noise-based applications also include monitoring seismic velocity changes for volcanoes and faults [Brenguier et al., 2008, 2011, Wegler and Sens-Schönfelder, 2007].

Most seismic ambient noise studies rely on the assumption of a homogeneous distribution of noise sources [Gouédard et al., 2008]. Many studies use noise in the frequency band of ocean microseisms, but oceanic noise sources are localized and unevenly distributed [Froment et al., 2010, Tsai, 2009, 2011]. In addition to the primary and secondary peaks, we have the 26 s microseism, which is excited continuously from a fixed source location and can grow so strong it is detected on seismic stations almost globally. This can affect the outcome of noise based studies, and needs to be accounted for in ambient noise applications [Shapiro et al., 2006, Zheng et al., 2011]. But, if we know where the source is located and how it behaves over time, this source can potentially be used for imaging the subsurface. [Xie et al., 2021]

1.2 The 26 s microseism

The 26 s signal is the most known example of a persistent localized source, partly because it can be detected on stations almost globally, partly because we have known about its existence for more than half a century, and we still have no explanation for it. The source is located somewhere in the Gulf of Guinea. Recently, several similar signals, although not as energetic, have been discovered in the gulf.

1.2.1 Geological setting

The Gulf of Guinea is situated in the Atlantic on the west coast of Africa, off the coast of Cote d'Ivoire, Ghana, Togo, Benin, Nigeria, Cameroon, Equatorial Guinea and Gabon(Figure 4). It is divided into two smaller parts; the Bight of Benin and the Bight of Bonny. The rivers Niger and Volta drain into the gulf. In the Gulf we can find a line of volcanic islands, with among others, Annobón, Bioko, Príncipe and São Tomé. The coast has a steep slope outwards to depths of over 5000 m.

The major geological features around the Gulf of Guinea include the Cameroon volcanic line and the Benue Trough, shown in Figure 4. The Cameroon volcanic line is a 1600-kilometer-long volcanic chain consisting of sea mounts and volcanoes, that starts with a linear trend that stretches from the Atlantic ocean to the continental part of the African plate, where it extends across Cameroon and splits into a Y shape. [Fitton and Dunlop, 1985] The origin of the Cameroon volcanic line is still debated. Linear volcanic mountain chains, such as Hawaii, are generally explained by rising mantle plumes or hot spots. Such hot spot volcanic chains show a distinct age progression resulting from the plate passing over the hot spot. The Cameroon volcanic line does not exhibit this characteristic chronological progression. Instead it appears to have been randomly active along almost the whole length of the volocanic line, and can therefore not be explained by a simple hot spot model [Fitton, 1987, 1980]. Alternative models have been proposed as the driving mechanism for the magmatism, as a wall or "hot line" of upwelling mantle material [Meyers et al., 1998], multiple closely spaced plumelets [Ngako et al., 2006] or a single plume spreading out [Burke, 2001] and decompression melting under fault zones [Fairhead, 1988]. Previous studies indicate a low velocity region under the entirety of the Cameroon volcanic line, that overlaps with the volcanic activity, and is used to argue for an edge-flow convection model for the Cameroon volcanic line [Reusch et al., 2010].

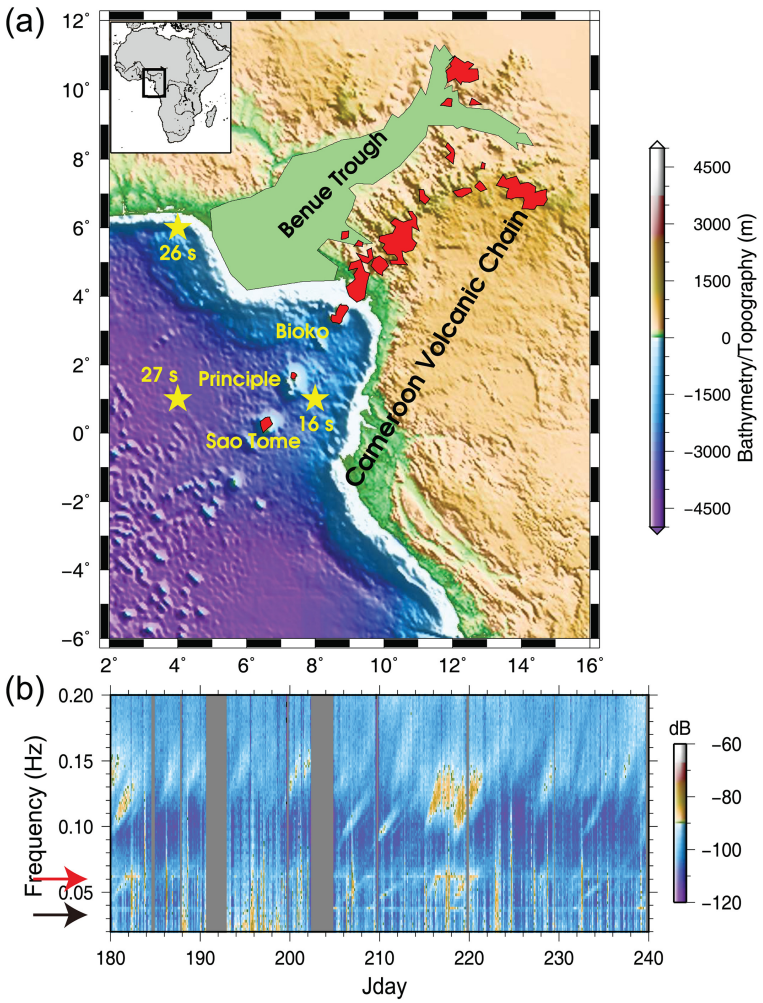

Figure 4: Overview of the main geological features of Gulf of Guinea, as well as location and frequency of the persistent localized tremors from Xia and Chen [2020]: a) Location of the Gulf of Guinea. Its main geological features include the Cameroon volcanic line (red) and the Benue Trough (green). The location of the 26 s, 27 s and 16 s source as determined in the study by Xia and Chen [2020] is marked with yellow stars. b) The persistent localized tremors shown in time and frequency. The red arrow points to the 16 s (0.062 Hz), while the black arrow points towards the 26 and 27 s signals.

Parallel and to the west of the Cameroon volcanic line we have the Benue Trough, a 1000-km-long rift system filled with sediments, that also exhibits a Y shape, similar to the volcanic line, but it is older [Fitton, 1980, Fitton and Dunlop, 1985]. The Niger Delta is positioned on the continental margin at the

apex of the Gulf of Guinea, on the same axis as the Benue Trough. The delta holds many hydrocarbon resources and is an active area for the oil industry. Both active and extinct mud volcanoes are reported in the area [Graue, 2000], and extinct volcanoes have been reported underneath the thick sediments of the Niger delta [Davies et al., 2005]. The location of the 26 s source found by Xia and Chen [2020] is shown in Figure 4. The areas where mud volcanoes and extinct volcanoes have been located (Figure 5 and 6), is not close to the 26 s source.

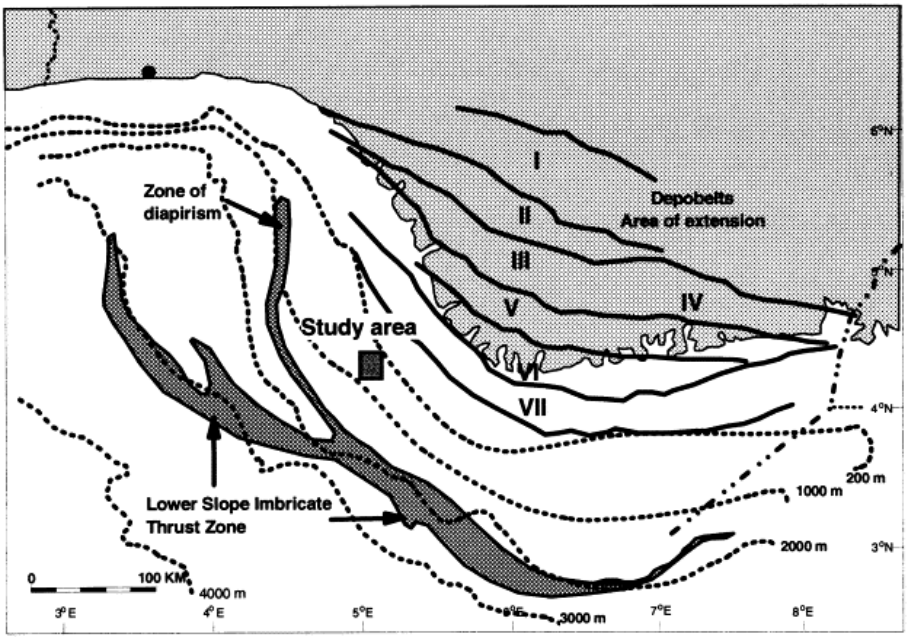

Figure 5: Study area from Graue [2000]. Both active and extinct mud volcanoes are reported in the study area.

1.2.2 Historical overview

In the early 1960's, Oliver [1962] discovered a "storm" of microseisms with periods 26 to 27 s on seismograms worldwide. In this case, "storm" just refers to microseismic amplitudes that are significantly larger than normal. Oliver [1962] located the signal in the Gulf of Guinea, and suggested that the seismic waves were generated from dispersed long period ocean waves striking the coast of the gulf. Such long period ocean waves, needed to generate a 26 s signal, are unusual and are only generated under extreme weather conditions[Oliver, 1962]. Oliver [1962] hypothesized that the long period ocean waves could be associated with a severe storm in the South Atlantic a few days before.

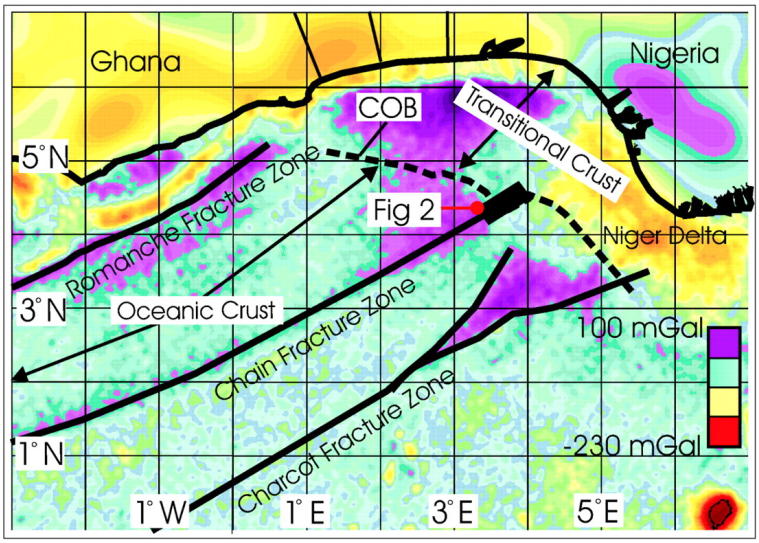

Figure 6: Figure from Davies et al. [2005] showing free-air gravity data from Sandwell and Smith [1997] over Romanche, Chain, and Charcot Fracture Zones and Niger Delta. The black box shows the study area for Davies et al. [2005], where extinct volcanoes were reported underneath the thick sediments of the Niger delta.

Later, Holcomb [1980] showed that this observation of the 26 s signal was not an isolated case, but a persistent part of the ambient noise spectrum; a narrow band peak existed in the seismic noise spectra on stations globally around 26 s. Holcomb [1980]'s observations showed a 26 s spectral peak that was persistent in time, without the dispersive characteristic described by Oliver [1962]. The spectral amplitude, however, modulates over time. Occasionally, the signal becomes so strong that it can be detected on seismic stations almost globally. Such "bursts" can typically last for hours or days, and is as strong as an M5 earthquake. [Xia et al., 2013] The amplitude of the peak was also shown to vary with the seasons, and was larger during the southern hemisphere winter. [Holcomb, 1998].

Shapiro et al. [2006] investigated the signal on cross-correlations of seismic noise records between different stations and confirmed that the source originated in the Gulf of Guinea with maximum amplitudes in the southern hemisphere winter. Shapiro et al. [2006] proposed a generation mechanism of long period waves interacting and possibly reflecting from the continental shelf could constructively interfere in a narrow frequency band in the deep ocean. In addition, a weaker source with similar spectral characteristics and no clear seasonal variation was found in the Fiji basin, which is almost the antipodal location of

the source in the Gulf of Guinea [Shapiro et al., 2006]. The antipodal location and weaker amplitudes, combined with the broader spectral peak lead to the hypothesis that these signals were excited from one single source in the Gulf of Guinea. However, the temporal variation of the two sources was different, suggesting that they are two independent sources [Zeng and Ni, 2014]. Zeng and Ni [2014] located the second 26 s source in the Vanuatu islands, close to the volcanoes in the Vanuatu Islands, and proposed that the signal was excited by magmatic processes, solely based on the tremor being located close to active volcanoes. No physical tremor mechanism has been offered. The location was later constrained to the active volcano Ambrym in the Vanuatu Arc, where persistent signals with periods of 25 and 18 s are recorded [Kawano et al., 2020]. The physical mechanism behind the source in the Gulf of Guinea remains unclear. Other observations of seismic signals in the Gulf of Guinea, may help put constraints on candidate source mechanisms.

The Gulf of Guinea tremors

Xia et al. [2013] reported a second persistent monochromatic source in the Gulf of Guinea, at slightly lower frequencies than the 26 s (0.038 Hz) source, at a frequency around 0.036 Hz (27 s). The source was shown to be independent from the 26 s source, and was located close to the Sao Tome volcano (Figure 4). Therefore it was suggested that its excitation was related to volcanic processes.

Recently, a third persistent localized source was discovered in the Gulf of Guinea.[Xia and Chen, 2020] This signal was at shorter periods than the previously reported sources, with a peak at a period of 16 s, close to the secondary microseismic peak. The 16 s source was also located close to the Cameroon volcanic line (Figure 4), suggesting that it is related to volcanic activity. Since, the source also exhibits seasonal variation consistent with long-period ocean wave activities in the Gulf of Guinea, Xia and Chen [2020] suggested that if the source is volcanic, it could be generated by a resonator that can be modulated by ocean waves. Although ocean waves cannot be ruled out as the source of the 26 s microseism, the Gulf of Guinea tremors share a lot of spectral similarities with very long period volcanic tremor [Kawakatsu et al., 2000, Cesca et al., 2020].

1.2.3 Gliding tremor

We discover a new phenomenon in the gulf that has previously not been reported in the literature. Gliding tremors often accompany bursts of energy in the 26 s signal. The gliding starts at the same frequency as the 26 s microseism and glides from 26 s to at least 20 s. The gliding lasts for about 2 days. Similar to the 26 s signal, the glides are narrow band and the gliding is visible on stations globally. The two phenomena appear to originate from the same source area. The glides are extremely repeatable, with the same change in frequency and duration. These observations could be what Oliver [1962] referred to as the "dispersive storm". Oliver [1962] detected the storm on ultra-sensitive seismographs for an interval of about 2 days of which the period decreased from about 28 to 20 s. This suggests that the gliding traces back to the time of the very first observation of the 26 s microseism that has been reported. The glides start at lower frequencies that what you typically would get from ocean related phenomena, and does not appear to be related to storms. But the glides resemble gliding volcanic tremor observed leading up to and following volcanic eruptions [Powell and Neuberg, 2003, Lesage et al., 2006, Hotovec et al., 2013].

1.3 Volcanic tremor

As magma ascends through the crust, interactions between magmatic fluids and the surrounding bed rock causes persistent seismic signals observed at seismometers close to active volcanoes. These ground motions are called volcanic tremors. The definition of volcanic tremor is a persistent seismic signal observed close to active volcanoes that lasts for several minutes to several days [Konstantinou and Schlindwein, 2003]. Most volcanoes show some kind of volcanic tremor during different stages of volcanic activity. However, it is often observed leading up to and/or following volcanic eruptions. Therefore it is an important tool for monitoring volcanic activity.

1.3.1 Tremor characteristics

Most volcanic tremor occurs at frequencies 1 to 5 Hz and has a duration of minutes [McNutt, 1992]. Inspecting tremor signals in time, they typically have an emergent onset, which make it difficult or impossible to pick the first arrival. Therefore traditional travel-time location methods that are used

for earthquakes cannot be applied to emergent volcanic tremor [Hofstetter and Malone, 1986]. There are some exceptions of volcanic tremor with clear impulsive onsets, for example at Kilauea [Aki and Koyanagi, 1981] and Mt. St. Helens [Fehler, 1983].

Tremor is often characterized by how the signal appears in time and frequency. For example, tremor bursts separated by quiet periods are characterized as banded tremor because it is visible as stripes or bands [McNutt, 1996] in spectrograms. Spasmodic tremor is characterized as a continuous tremor with large variation in amplitude, which is observed at Krafla [Brandsdóttir and Einarsson, 1992]. Short tremor bursts superposed on background earthquake activity, as observed at Etna [Seidl et al., 1990] is referred to as a tremor storm.

In frequency, the spectrum often consists of one single narrow peak or a series of peaks, either representing the fundamental and its harmonics or a random distribution. When the spectrum has one sharp peak, it is called monochromatic. If the series of spikes correspond to the fundamental frequency and overtones, it is referred to as harmonic [Konstantinou and Schlindwein, 2003]. Observed changes in frequency content over time of tremor is observed at volcanoes worldwide, such as Arenal [Hagerty et al., 2000], Semeru [Schlindwein et al., 1995], Redoubt [Hotovec et al., 2013], Lascar [Hellweg, 2000] and Montserrat [Neuberg, 2000]. More specifically, upwards gliding has previously been observed leading up to explosions at volcanoes as Arenal [Lesage et al., 2006], Soufriere Hills [Powell and Neuberg, 2003] and Redoubt [Hotovec et al., 2013] Changes in frequency is associated with changes in the source and is therefore important for forecasting volcanic eruptions.

Studies of the wavefield of volcanic tremor show that tremor is mostly composed of Love and Rayleigh waves [Ferrazzini et al., 1991, Ereditato and Luongo, 1994, Wegler and Seidl, 1997], but some studies also report body waves in addition to surface waves [Almendros et al., 1997]. It is possible to calculate the backazimuth of the incoming waves using polarization properties. This is used to find the source location of the tremor at Kilauea [Ferrazzini et al., 1991] and Masaya [Métaxian et al., 1997].

1.3.2 Tremor generation mechanisms

As volcanic tremor represents the interactions of materials with different physical properties, it is difficult to find its exact physical generation mechanism. Numerous tremor generation mechanisms have

been proposed, as well as combinations of mechanisms. However, different mechanisms can produce the same signals and multiple mechanisms can be active simultaneously in the same volcanic system for the same eruption [Soubestre et al., 2021, Lesage et al., 2006]. Here we give an overview of volcanic tremor generation mechanisms based the summary from Konstantinou and Schlindwein [2003]. The suggested mechanisms are grouped as fluid-flow-induced oscillations, excitation of fluid-filled cracks and hydrothermal boiling.

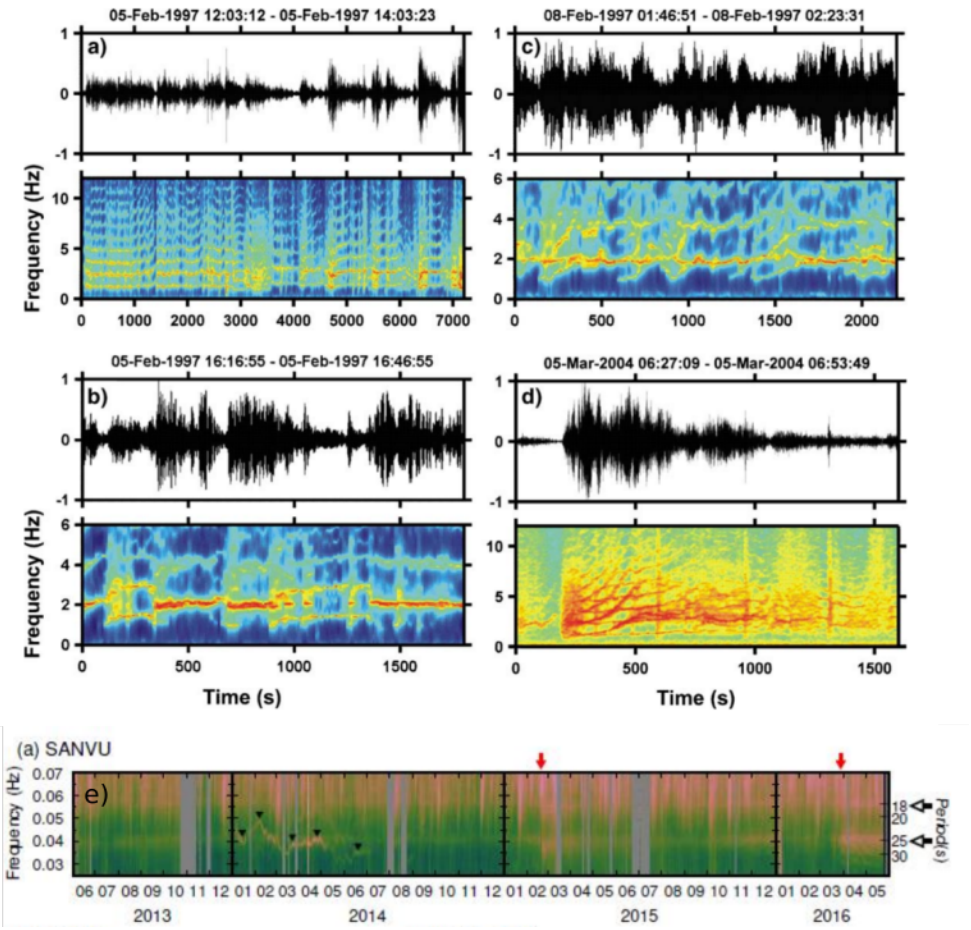

Figure 7: a)b)c)d) Complex gliding signals detected at Arenal volcano, Cosa Rica from Lesage et al. [2006] interpreted as a conduit sealed off by a fractured plug, with gliding related to pressure variations in the conduit. e) Long period monochromatic and gliding tremor at Ambrym volcano, Vanuatu from Kawano et al. [2020].

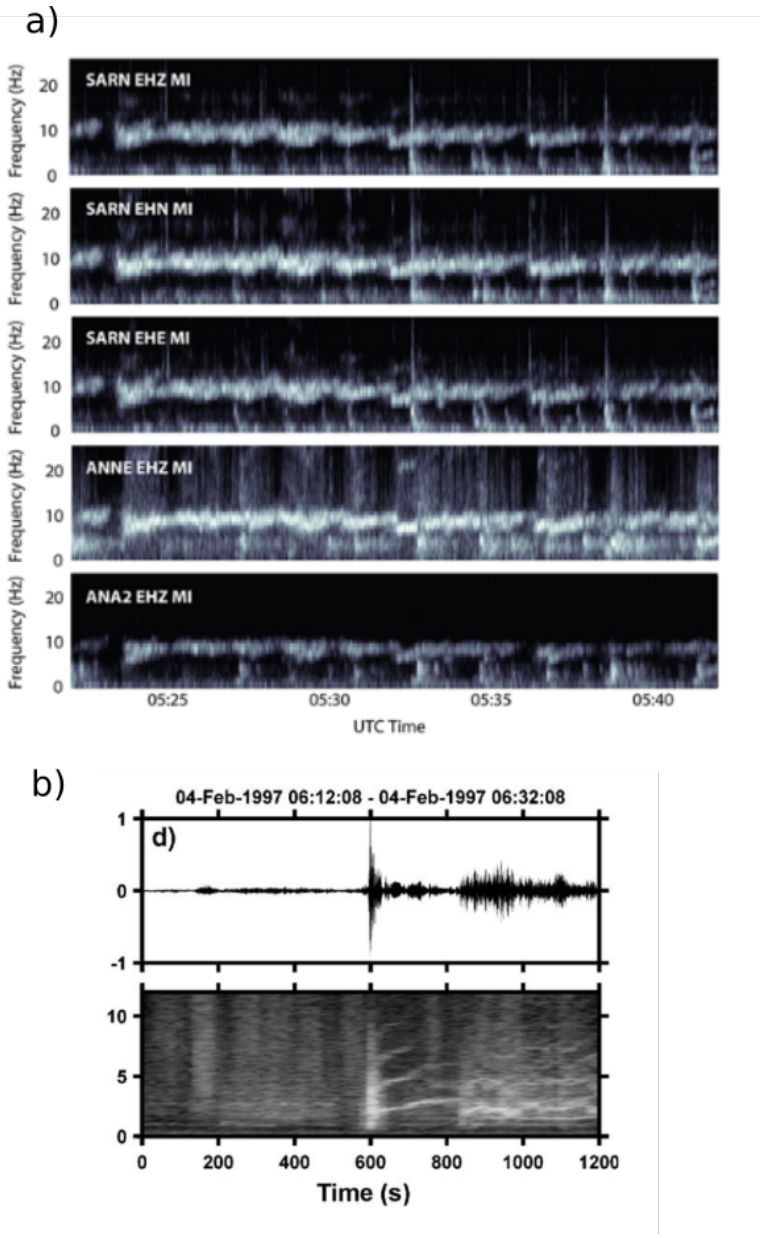

Figure 8: a) Series of upward glides in a saw tooth pattern preceding eruption at South Sarigan Seamount from Searcy [2013], interpreted as resonance of magma-gas mixture resulting from intrusion of magma into the conduit. b) Upward glide observed after eruption at Arenal from Lesage et al. [2006], interpreted as the upper end of a conduit sealing by cooling of superficial lava.

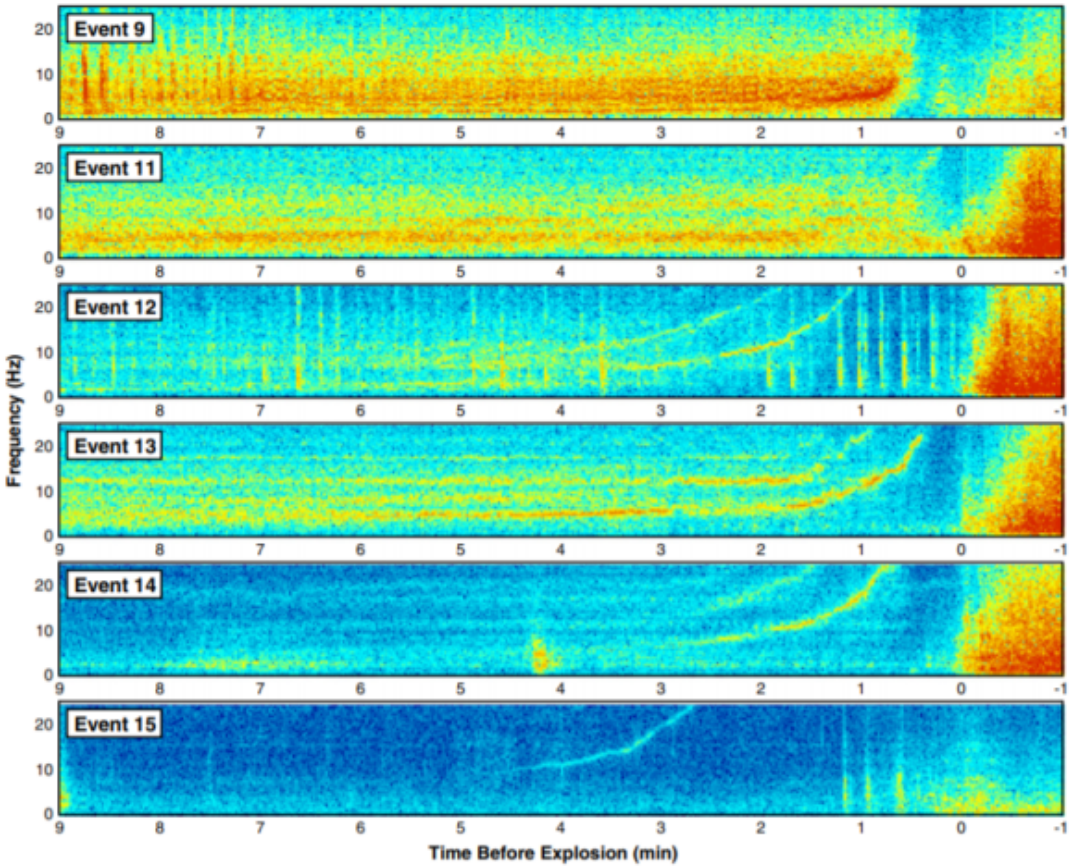

Figure 9: Repeated upward glides preceding explosion events at Redoubt volcano 2009 from Hotovec et al. [2013], produced by the superposition of increasingly frequent and regular stick-slip earthquakes.

Fluid-flow-induced oscillations

Here we consider volcanic tremor excited by magmatic fluid-flow in conduits. Tilt observations suggest that there is a connection between the magma flowing in and out out the reservoir and volcanic tremor generation[Dvorak and Okamura, 1985, Fukao et al., 1998, Oikawa et al., 1991]. To describe the flow inside a vertically extending crack connecting an upstream and downstream reservoir, Julian [1994] derived a third-order system of non-linear differential equations whose solutions are controlled by the fluid flow pressure (p). According to Bernoulli's theorem, the quantity $p + (\rho v^2)/2$ must remain constant. Here v is the flow speed and ρ is the fluid density. Therefore, for large flow speeds, the fluid pressure in the conduit decreases and the walls move towards each other, constricting the flow.

When constricting the flow, the pressure builds up again, which forces the walls apart. This results in periodic oscillations [Konstantinou and Schlindwein, 2003]. For low fluid pressure, numerical solutions indicate that for fluid pressure less than 10 MPa account for short-lasting oscillations, resembling the behaviour of low-frequency earthquakes, in the interval 10–15 MPa account for sustained oscillations, while fluid-pressure values greater than 15 MPa produces a large number of subharmonics, known as period-doubling cascades.

Fluid-flow induced tremor can also be generated if the fluid system is suddenly perturbed from its equilibrium state. The system can be perturbed by fracturing of the surrounding bedrock, sudden change in fluid supply or the formation of a new conduit. This generates a fluid transient. The transient causes pressure oscillations that move the conduit walls and generates elastic waves in the surrounding medium [St. Lawrence and Qamar, 1979, Ferrick et al., 1982]. The tremor characteristics depend on the physical properties of the fluid, the geometry of the conduit and the boundary conditions. The frequency response of the system is controlled by the characteristic impedance of the fluid and the orifice, denoted as Z_c and Z_{or}. The impedance of the fluid is given as $Z_c = agA$, where a is the pressure wave speed in the fluid, g is the gravitational acceleration and A is the area of the cross section of the conduit. The impedance of the orifice is defined as $Z_{or} = 2HQ$. Here H is the pressure head and Q is the fluid flow rate. For a small conduit opening ($Z_{or} > Z_c$) only a small quantity of fluid passes through, which resembles a closed-pipe system. The the frequencies are given by $\omega = n\pi a/2L)$. L represents the length of the conduit and $n = 1, 3, 5....$ When $Z_{or} < Z_c$, the system behaves as an open pipe. Then the frequencies are gives by the same equation with $n = 2, 4, 6...$ [Konstantinou and Schlindwein, 2003]. Such unsteady flow in conduits followed by tremor-like signals has been compared to water moving through outflow tunnels at Tarbela dam in Pakistan [McNutt, 1986].

Excitation of fluid-filled crack

As magma moves upward during different stages of volcanic activity, cracks are formed. Except for the duration, low frequency volcanic tremor and earthquakes are similar in both the frequency domain and time domain. This suggests that both signals could be generated by the same source mechanism, and that the type of signal is generated depends on the excitation mechanism [Fehler, 1983, Chouet, 1985, Hofstetter and Malone, 1986, Tsuruga et al., 1997, Almendros et al., 1997].

Chouet [1986, 1988] investigated the displacement of the walls of a fluid-filled crack, due to a pressure disturbance in the fluid, as a possible generation for both low frequency events and tremor. Chouet [1986, 1988]'s model assumes the vibration of a rectangular crack with inviscid fluid and surrounded by bedrock behaving as a Poisson solid. Then, the generated wavefield depends on the listed parameters: the crack geometry, the position and area over which the pressure disturbance occurs, boundary conditions for the stress on the crack's surface and the fluid flow at the crack perimeter, the crack stiffness C defined as

$$C = \frac{bL}{\mu d} \tag{8}$$

in which b is the bulk modulus of the fluid, L is the length of the crack, μ the rigidity of the solid and d the thickness of the crack, and the fluid solid impedance contrast Z given by

$$Z = \frac{\rho_s \alpha}{\rho_f a}. \tag{9}$$

Here, ρ_s represents the density of the solid and α is the P-wave velocity of the solid, while ρ_f represents the density of the fluid and a is the P-wave velocity of the fluid. The resulting spectrum is dominated by sharp peaks, representing the mixing of the longitudinal and lateral modes of the resonating crack, given by $2L/n$ and $2W/n$ where $n = 2, 3, 4...$ respectively. L and W are the length and width of the rectangular crack.

As a possible physical mechanism, Morrissey and Chouet [1997] studied shock waves from choked flow inside a crack, and found that unsteady shock waves near the crack wall can generate pressure transients that can set the crack into resonance.

Chouet [1988] found that the fundamental frequency for the resonating crack was lower than what was expected, due to a slow wave propagating along the fluid-solid boundary, called a crack wave. This opens for low frequency tremor from more reasonably sized structures. For example the 10 s tremor observed at Mt. Aso can be explained by a crack of 1 km length and 0.5 m thickness which would have a resonance period of 10 s assuming $\rho_s/\rho_f = 2.5$ and $\alpha/a = 1.5$. [Ferrazzini and Aki, 1987]

Hydrothermal boiling

Geysers and hydrothermal reservoirs can generate tremor-like signals associated with boiling groundwater [Kedar et al., 1996, Kieffer, 1984]. Boiling groundwater causes the formation and growth of bubbles in the liquid. The bubbles can collapse if they reach a region of lower temperature. Both bubble growth and collapse can generate seismic energy, but bubble collapse is more efficient[Leet, 1988]. Boiling groundwater generates a broad band seismic signal similar to white noise, with equal energy in each frequency band. We can get the characteristic sharply peaked tremor spectra, associated with volcanic tremor, if the boiling groundwater is contained in a channel. Then the boiling can excite the channel into resonance. The length of the channel is given by $L = a/2f$, where a is the sound velocity in the liquid, while f is the fundamental frequency. This generation mechanism is thought to be similar to the mechanism for tremor recorded in quiet periods at volcanoes, so-called 'non-eruption tremor'.[Leet, 1988]

1.3.3 Visual observations

To help determine the physical mechanism for specific tremor observations, visual observations, such as independent information from for example microphones or cameras can be used. Often the amplitude of the tremor shows a direct relationship with eruptive activity. For example, an increase in tremor happening at the same time as visual observation lava fountaining or dome building has been reported by McNutt [1986], Dvorak and Okamura [1985], Brandsdóttir and Einarsson [1992]. At Karymsky 'chugging' tremor, possibly generated by gas release through a plug, acting as a valve, was followed by steam like locomotive sounds [Johnson and Lees, 2000]. Strong tremor occurred while high temperature volcanic gas was emitted from the vent at Satsuma-Iwojima [Ohminato and Ereditato, 1997]. In other cases the amplitude variations are not accompanied by superficial activity. This suggests that these changes in amplitude are related to magma flow at large depths in the crust, instead of eruptive activity [Gasparini et al., 1992].

1.4 Research objectives and thesis structure

Information about ambient noise sources, such as how they evolve over time, where they are located and wavefield composition, is necessary to improve our knowledge about their generation mechanisms, and also to understand how changes in noise sources can affect applications of ambient noise. The low frequency range, below about 0.05 Hz, is the part of the ambient noise spectrum that we know the least about. Here, we focus on the 26 microseism, a monochromatic low frequency ambient noise signal that has been puzzling seismologists for decades. We study the location, wavetype radiation and temporal variation of the 26 s source to get closer to resolving its physical mechanism. We also investigate the temporal variation in the long period, long duration gliding tremor to find an explanation for the frequency gliding. Our gliding tremor observations cannot be explained by known oceanic or volcanic mechanisms, which highlights this gap in long period ambient noise generation. This discovery may help put constraints on generations mechanisms for long period ambient noise. Because volcanic tremor is a key tool for monitoring volcanic activity, this discovery may affect future forecasting of activity at volcanoes.

Firstly, a brief summary of the main methods used in this work is presented in Section 2. This thesis is composed of two different manuscripts which are separated into two different sections, Section 3 and 4. The first manuscript, presented in Section 3, comprises the discovery of gliding tremors associated with the 26 s seismic source in the Gulf of Guinea. In the second manuscript (Section 4), we constrain the source location and wave types of the 26 s tremor and gliding tremor, and the connection between the sources. This is followed by a discussion (Section 5), where we sum up the observations and arguments for physical mechanisms for the 26 s and gliding tremor. The conclusions are given in Section 6 Lastly, an outlook is presented in Section 7.

2 Methods

This section provides an overview of the methods used in this work. First we introduce a method to detect spectral peaks from the low frequency (0.02-0.05 Hz) part of the ambient noise spectrum. Then we explore different array processing methods for locating the source areas of ambient noise, namely beamforming and matched field processing, as well as the limitations associated with these methods.

2.1 Detection of spectral peaks

The 26 s peak is not always detectable, but occasionally it grows so strong that it can be detected on stations globally. Such bursts of energy typically lasts for hours. In order to find suitable time windows for investigating the 26 s source and look for temporal and seasonal variation, we find when and how often the peak is detected on stations across the continents. The peak detection is done by correlating the amplitude spectra of four permanent broadband stations (SSB, GRA1, TAM, BFO). The location of the stations is shown in Figure 10a). These stations were selected because they were previously used to study the 26 s source, and long time series was available with typically low noise levels making detection easier.

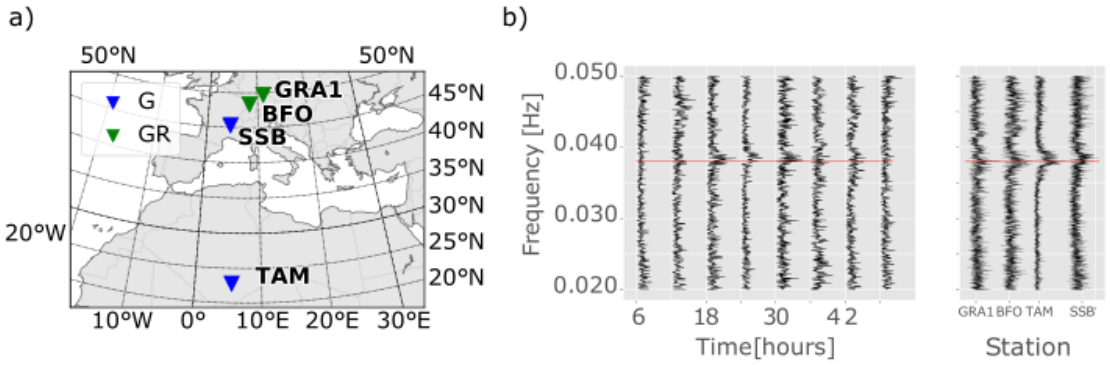

Figure 10: a) Stations used for peak detection. A peak is detected on 2013-01-07. First the spectral amplitdue variation is shown on station SSB for 48 hours, then the spectra for the whole day on the 4 stations in a) is shown.

To focus on the frequencies close to the 26 s microseism, we apply a band pass filter between 0.02 and 0.05 Hz. The spectra are calculated for each day, to have a good resolution in frequency and detect daily changes in the spectra. The days that had less than 4 hours data availability, were excluded from the analysis. We compute the correlation matrix for the four stations' spectra, calculated for overlapping frequency intervals (0.002 Hz), using the Pearson correlation coefficient. The mean and standard deviation for each matrix is calculated. The values are assigned to the center frequency of the window. When a spectral peak is coherent on all four stations, that results in a high value for the mean correlation coefficient at this frequency. Figure 10 shows the spectra for a 2013-01-07 for the 4 stations on a day when the peak is detected. Figure 11 shows two examples of the mean of the correlation as a function of frequency with corresponding standard deviation. For the case of a coherent peak across the stations, the day is a so-called "good day", while it is named a "bad day" without a peak detection. A spectral peak is automatically identified if: 1) the jump between neighboring frequencies is larger than the standard deviation (red vertical line), or 2) if the average of a portion of the spectrum (0.005Hz) is larger than the overall average (blue marked section). Both criteria is satisfied for the "good day" shown here.

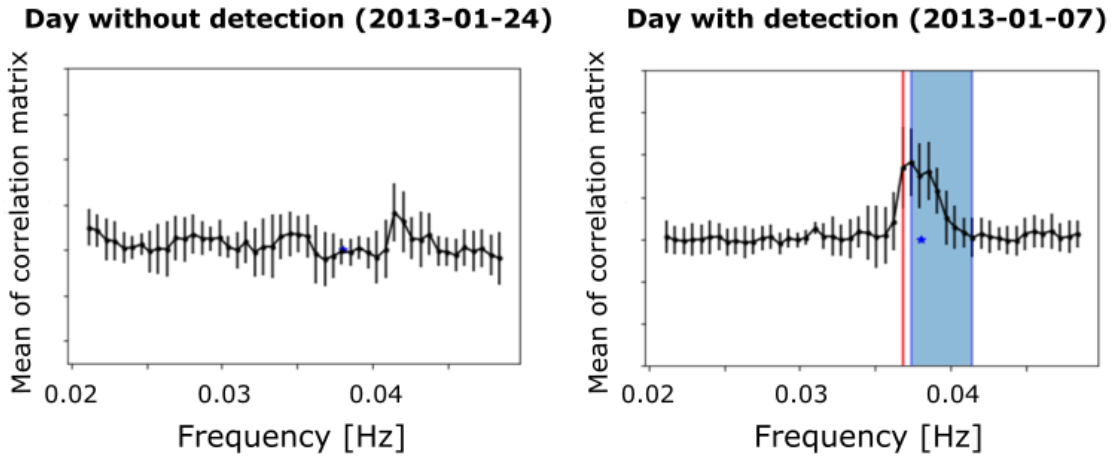

Figure 11: Mean of the correlation as a function of frequency with corresponding standard deviation for a day with detection and without a detection.

Limitations and seasonal variations

The approach identifies coherent spectral peaks between 0.02 and 0.05 Hz, and is not constrained to the 26 s peak. The amplitude of the 26 s peak is close to the amplitude of the surrounding noise levels. This can have an effect on the number of detections that are actually from the 26 speak. Since all the stations used for spectral peak detection are located on the northern hemisphere, this effect is stronger in winter, when higher ambient noise levels are present towards the upper half of our considered period band [Stutzmann et al., 2009]. To illustrate this, a comparison of the daily spectral amplitude for July and January for the years used in our peak detection is shown in Figure 12 with a spectral peak detected on July 2nd 2006.

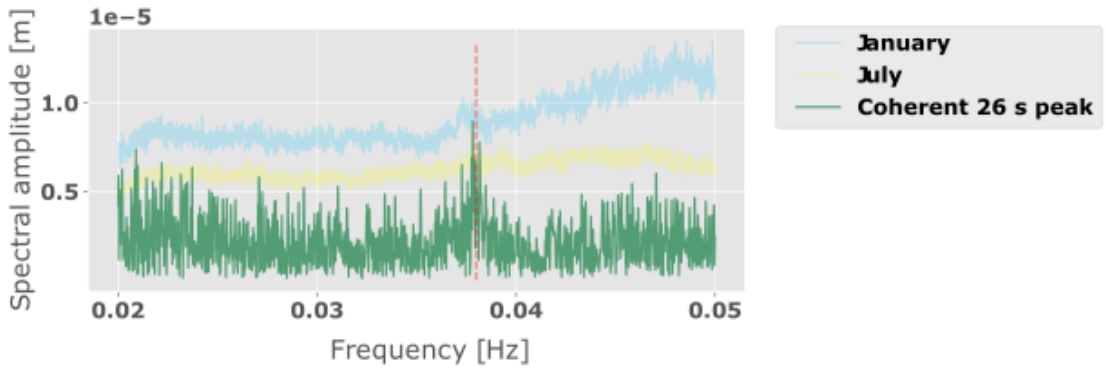

Figure 12: Comparison of the daily spectral amplitude for July and January for the years used in our peak detection with a spectral peak detected on July 2nd 2006.

2.2 Beamforming

Beamforming is an approach used to determine the wave type and the source location of an incoming signal from seismic data measured by an array of seismic stations. The method allows us to estimate the coherent seismic energy that propagates across the array and determine its propagation characteristics, as propagation direction, slowness and frequency. The resolution capabilities of the method at different frequencies strongly depend on array configuration.

In general, beamforming is a delay-and-sum process. If we assume a plane wave approaching an array from a given direction, it will arrive at the station that is the closest to the source first. The delay of the arrival of the signal at the different stations therefore depends on the apparent slowness/velocity of the signal. The array beam is formed by shifting the individual seismic traces recorded at different stations according to theoretical travel time differences Δt of an assumed plane wave propagating across the array from a given direction. Then, the shifted signals are summed to form the beam trace. When the signal is coherent, the constructive interference will lead to a larger amplitude of the beam trace.

The wavefront can be parameterized in terms of its direction of arrival θ, its horizontal slowness u_h. The horizontal slowness is given by $u_h = sin(i)/v = 1/v_{app}$ where v is the phase velocity v_{app} is the apparent horizontal phase velocity at the array site and and i is the incidence angle of a seismic ray measured relative to the vertical axis. The horizontal slowness in the direction of wave propagation is given by

$$\mathbf{u}_h = [u_x, u_y, u_z] = u_h[sin(\theta), cos(\theta), 1/tan(i)] \tag{10}$$

The theoretical delays in travel time between the different stations and a reference location can then be calculated for a plane wave approaching the array. This delay is given by $\Delta t_i = \mathbf{r}_i \mathbf{u}_h$, where $\mathbf{r}_i$ is the location vector from the reference point to the location of a given station i. This time difference corresponds to the travel time offset that needs to be corrected for at different stations to form a beam. This array beam $b(t)$ for one component in the time domain can be formed by correcting for the theoretical time shifts according to the incident wavefront properties $\mathbf{u}_h$ and θ and is expressed by Rost and Thomas [2002] as

$$b(t) = \frac{1}{N}\sum_{i=1}^{N}(a(t) + n_i(t + \mathbf{r}_i\mathbf{u}_h)) = a(t) + \frac{1}{N}\sum_{i=1}^{N} n_i(t + \mathbf{r}_i\mathbf{u}_h) \tag{11}$$

for recorded wave forms $x_i(t) = a(t - \mathbf{r}_i\mathbf{u}_h + n_i(t)$ for a signal model described by a plane wave signal $a(t)$ and uncorrelated local noise $n(t)$ at $i = [1, ..., N]$ stations. Then, the beam gives you the coherent signal and a reduced amount of incoherent noise.

In order to obtain the set of parameters that maximizes the beampower, indicating a coherent signal, a grid search through the parameters is done. When sources are close to the array, the assumption of an incoming plane wave is violated. In order to account for curved wavefronts we introduce matched field

processing in section 2.3.

If we consider the signal model of a plane wavefront in the frequency-wavenumber domain, the Fourier transformed vertical component array data is given by Esmersoy et al. [1985]

$$\mathbf{X}(\omega) = \mathbf{e}(\omega)\Lambda(\omega) \tag{12}$$

where $A(\omega)$ contains the amplitude and phase of the incoming signal. The phase delays due to wave propagation from the source to the stations relative to a reference location are described by the steering vector

$$\mathbf{e}(\mathbf{u}_h, \omega) = [e^{i\omega \mathbf{u}_h (r_1 - r_0)}, e^{i\omega \mathbf{u}_h (r_2 - r_0)}, ..., e^{i\omega \mathbf{u}_h (r_N - r_0)}]^T. \tag{13}$$

The cross-spectral density matrix **R** between the Fourier transformed data **X** is expressed by the expectation value $E\{.\}$ of $\mathbf{R} = E\{\mathbf{X}(\omega)\mathbf{X}^H(\omega)\}$ which is comprised of the auto-power spectral density at each station in the diagonal and the cross-power spectral densities and the phase relations corresponding to the approaching true signal in the remainder. In this case, H is the Hermitian transpose. The frequency-wavenumber/Bartlett beampower can be written as the linear stack of weighted recordings at all stations for array output y is given by Esmersoy et al. [1985]

$$P_{FK}(u_h, \omega) = E|y^2| = E|\mathbf{e}_w^H(u_h, \omega), \mathbf{X}(\omega)|^2 = \mathbf{e}_w^H(u_h, \omega)\mathbf{R}(\omega)\mathbf{e}_w(u_h, \omega). \tag{14}$$

The beampower is maximized when the phase delays in the data $\mathbf{R}(\omega)$ are accurately corrected for by the weight $e_w(u_h, \omega)$.

Array performance

To evaluate the performance of the different arrays used in this study ([Douglas Wiens, 2005, Thomas, 2010, Utrecht University (UU Netherlands), 1983], we evaluate the beam power in the case of a single monochromatic plane wave coming from right below the array. The resulting beam power is called the array transfer function, and is affected by the number of stations, the spatial configuration and the array aperture. The main lobe of the transfer function represents the power distribution in the true arrival direction of the signal, while the side lobes are the energy contribution at other slownesses. An ideal transfer function thus has a narrow main lobe, with low power contribution from the side lobes [Gal and Reading, 2019]. Figure 13 shows the resolution capability of the three arrays at a frequency of 0.038 Hz for the given array geometry. A description of the arrays is given in Table 9

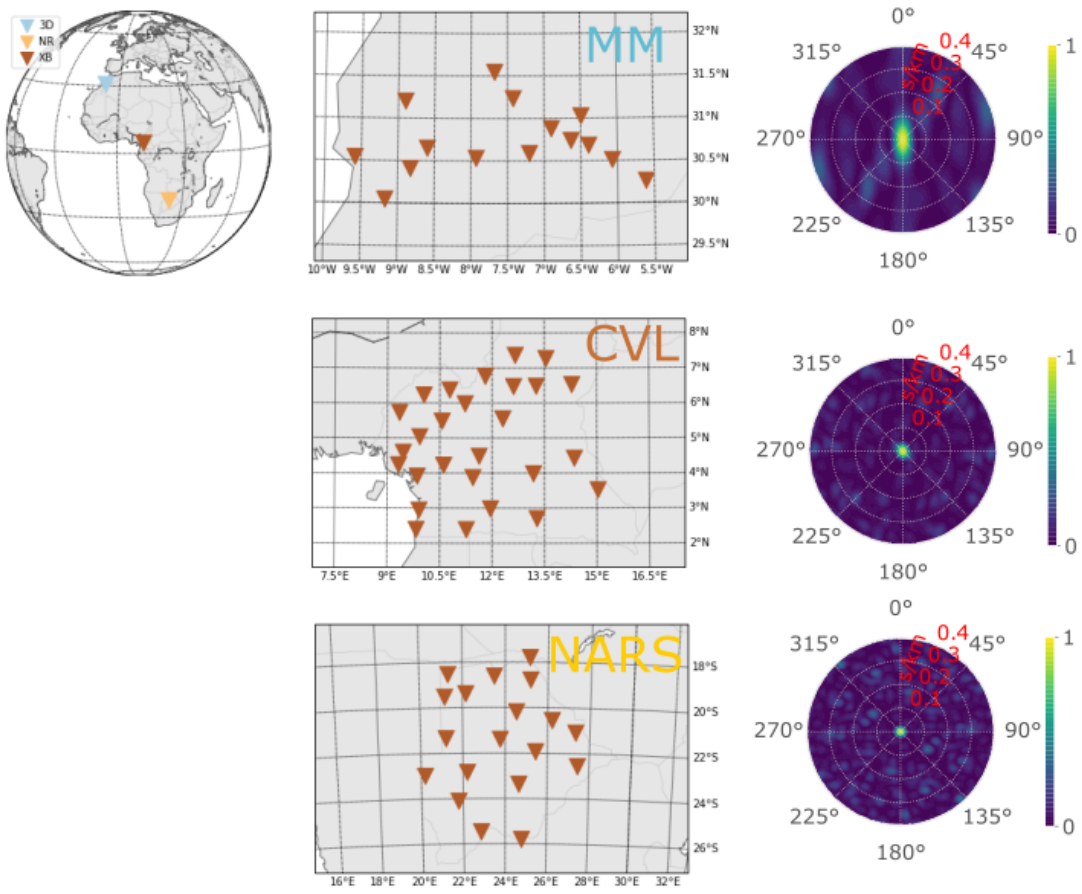

Figure 13: Resolution for arrays in Africa used for 3-C beamforming: The beamforming resolution is affected by the number of stations, spatial configuration and array aperture. To evaluate the performance of the different arrays, we study the beam power in the case of a single monochromatic plane wave coming from right below the array. The resolution capability of MM, NARS and CVL for at a frequency of 0.038 Hz for the given array geometry (a),c),e)) is shown in b), d) and f).

2.3 Matched field processing

Matched field processing is a generalization of beamforming, which allows arbitrary wavefronts. [Baggeroer et al., 1993] We start by assuming virtual sources at any given location. For each potential source location, a synthetic wavefield is computed and matched against the recorded wavefield, taking the co-

Table 1: Description of arrays used for 3-C beamforming

FDSN code	3D	NR	XB
Network name	MM	NARS	CVL
Timespan	2011-2013	2016	2006
Number of stations	15	19	27
Aperture (km)	383	888	679
Country	Morocco	Botswana	Cameroon
Latitude	30.79255	-21.80601	-19.401535
Longitude	-7.59595	23.82118	11.94225

herency of the wavefields across the stations into account. The computations are done in the frequency domain, and the spectra $d(\omega, \vec{x_j})$ are calculated from the seismograms recorded at each receiver location $\vec{x_j}$. The cross spectral density matrix is computed as

$$K_{jk}(\omega) = d^*(\omega, \vec{x_j}) d(\omega, \vec{x_j}), \tag{15}$$

where * is denoting the complex conjugate, and contains information about the recorded wavefield and the coherency across the stations. The synthetic seismograms computed for each receiver location $\vec{x}_j$ and virtual source location $\vec{x}_s$ is represented through the synthetic spectra $s(\omega, \vec{x}_j, \vec{x}_s)$. The synthetic spectra are computed from simple analytical Green's functions on the form

$$s(\omega, \vec{x}_j, \vec{x}_s) = e^{-i\omega t(\vec{x}_j, \vec{x}_s)}, \tag{16}$$

where $t(\vec{x}_j, \vec{x}_s)$ is the travel time between the source and the receiver. If we consider the most simple case of a single stationary source in an isotropic, homogeneous medium with constant velocity $v = const$ and only straight ray propagation of a single phase, the travel time can be expressed as $t(\vec{x}_j, \vec{x}_s) = \frac{\triangle x}{v}$. However, this requires that the velocity v is given. We also assume a constant velocity. How well this synthetic wave field matches the recorded wavefield is estimated by the beampower. The beampower is given as

$$B = \mathbf{s}^* \cdot \mathbf{K} \cdot \mathbf{s}, \tag{17}$$

The better the match, the higher the beampower. The position of the highest beampower represents the resolved source location. For limitations of this method we refer to Schippkus and Hadziioannou [2021]. If the array is far away from the source, matched field processing is essentially the same as beamforming since the wavefront that passes over the array is a plane wave. Therefore matched field processing and beamforming have the same limitations when the sources are in the far field.

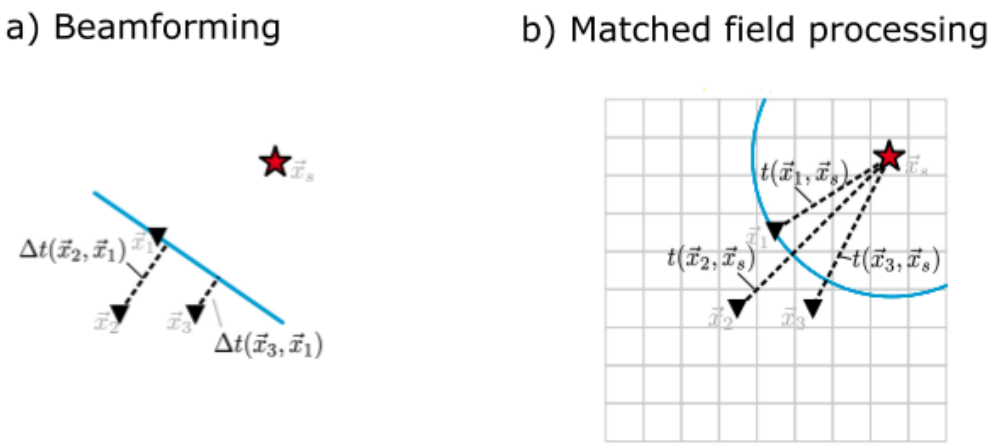

Figure 14: Approaches used for locating ambient noise sources from Schippkus et al. [2020]. The wavefronts are marked blue. a) Beamforming: Seismic traces on multiple stations are shifted in time corresponding to candidate plane-waves, and summed over. b) Matched Field Processing: assuming virtual sources at any given location.

3 Gliding tremors from the Gulf of Guinea shed light on 70 year old mystery

Charlotte Bruland, Celine Hadziioannou

Institute of Geophysics, Center for Earth System Research and Sustainability (CEN),

Universität Hamburg, Hamburg, Germany

In revision at Communications Earth & Environment.

Abstract

Since the 1960s, seismologists have known about a location in the Gulf of Guinea, which has been emitting monochromatic seismic waves at 26-second period, seemingly continuously for at least 70 years. The origin of these seismic waves remains enigmatic to date. We discover another, accompanying phenomenon to this '26-second microseism': every so often, an upward gliding tremor occurs. This tremor occurs at a frequency that is too low to be explained by the common volcanic or hydrothermal tremor mechanisms, and points towards a phenomenon that occurs on a massive spatial scale.

The strong repeatability of the gliding tremor, its extremely low frequency range, and the decades-long timescales where this phenomenon seems to have been active all point towards the need to view tremor in a different way.

Because volcanic tremor is an important tool to monitor volcanic activity, this discovery, and the implications for the size of magmatic and hydrothermal systems, and the tremor mechanisms involved, may affect future forecasting of activity at volcanoes.

3.1 Introduction

The mystery of the 26 s microseism has been puzzling geophysicists for decades. This sustained seismic signal is detected globally, with a constrained source location, but no observations so far seem to bring us closer to understanding which physical mechanism is causing this enigmatic signal. Here we present the unexpected discovery of exceptionally energetic, long-lasting, long period gliding tremors associated with the 26 s source.

The 26 s signal, with approximate coordinates (0,0), was discovered in the 1960's and is believed to be generated continuously, from a fixed location, since then [Oliver, 1962, Holcomb, 1980, Shapiro et al., 2006, Xia et al., 2013]. Still, the physical mechanism remains unclear. Several temporally persistent narrow-band signals have previously been located in the gulf, at 27 seconds and 16 seconds [Oliver, 1962, Xia et al., 2013, Xia and Chen, 2020]. As the sources at 27 s and 16 s are located close to the Cameroon volcanic line, magmatic origin has been proposed. However, there are no known volcanoes in the area where the 26 s source is located [Xia et al., 2013]. Uncovering the physical mechanism behind the frequency glides presented here, and their connection to the 26 s source, might help put constraints on the source mechanism behind the seismic signals in the Gulf of Guinea.

Usually, such sustained seismic signals are linked to volcanic activity, called volcanic tremor. [Konstantinou and Schlindwein, 2003] Nevertheless, various natural sources can generate gliding tremor, such as hydrothermal systems [Nayak et al., 2020, Franek et al., 2014], icebergs [MacAyeal et al., 2008], glaciers [Helmstetter et al., 2015], microtsunamis [MacAyeal et al., 2009], landslides and avalanches [Suriñach Cornet et al., 2005]. Artificial sources, such as trains [Fuchs and Bokelmann, 2018] and helicopters [Eibl et al., 2015], can also produce harmonic gliding tremor, similar to what is observed at active volcanoes.

These signals, however, have higher frequencies and shorter duration than the frequency gliding that we observe, and are typically only detected at short distances from the source. Tremor with characteristics such as those of the gliding tremors in the Gulf of Guinea have previously not been reported, and cannot

be explained by known tremor mechanisms. In this study, we aim to constrain the mechanism of the glides. Moreover, our new observations might help put constraints on possible mechanisms for volcanic and hydrothermal tremor in general.

3.2 Discovery of gliding frequencies associated with the 26 s microseism

Seismic observations reveal the presence of very long period frequency glides on broadband 3-component stations close to the Gulf of Guinea. Figure 15 shows an example of such frequency glides from vertical component data from a station in Cameroon (CM09) May 2006. The gliding is very narrow band and has an unusually long duration, up to several days. The frequency always glides up, from low frequency to higher frequencies. Closer inspection shows that the tremor starts at the same frequency as the 26 s microseism. Another remarkable observation is the linearity of the glides, as the frequency changes almost linearly from 0.038 Hz to at least 0.05 Hz. At this point, the primary ocean microseism drowns out the glide signal, and it can no longer be detected. The glides are harmonic, with a first visible fundamental frequency and an overtone with regular harmonic spacing, which appears to be maintained throughout the gliding episode. Both single glides and groups of glides are observed. Glide sequences can be long lasting, such as the sequence in Figure 15, which lasts for about 20 days. No clearly overlapping glides were observed.

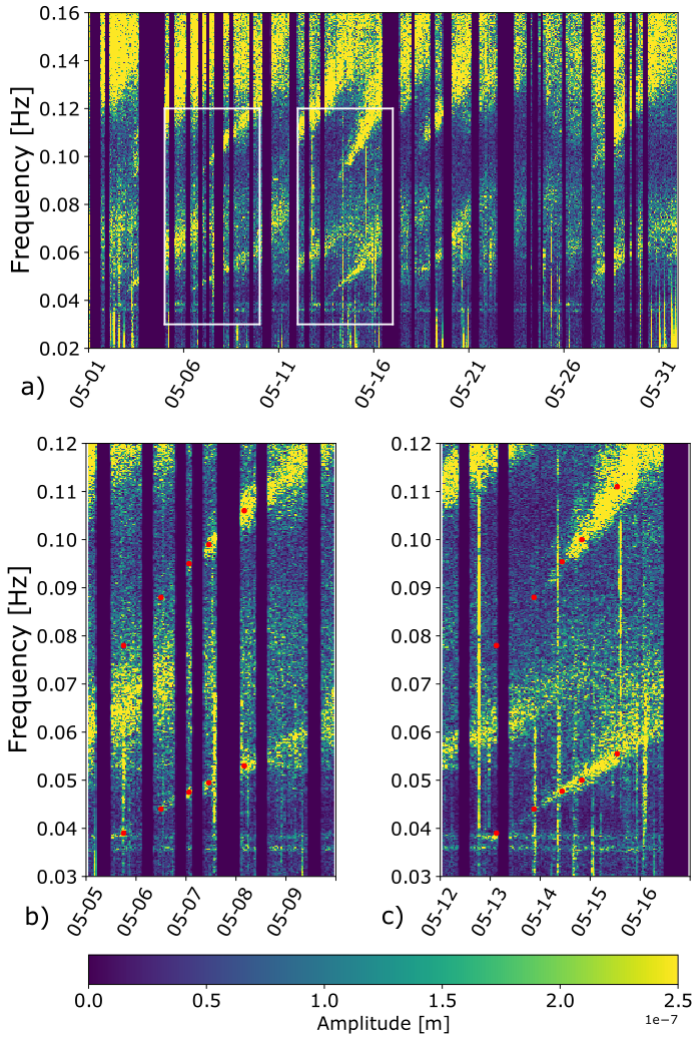

Figure 15: Harmonic frequency gliding on vertical component data from CM09 in Cameroon May 2006 a) White boxes mark the glides starting May 5th and 13th shown in **b)** and **c)**. The lower set of red dots correspond to the picked slope and the top red dots indicate the frequency of the overtone calculated from two times the fundamental frequency. The gliding starts at 0.038 Hz (26 s). We also see two persistent narrow-band tremors at 0.036 Hz and 0.038 Hz, reported by [Oliver, 1962] and Xia et al. [2013] respectively.

Inspecting seismic data from 13 consecutive years (2004 – 2016) shows that the frequency gliding is caused by a long-lived and ongoing process. Given that the 26 s microseism has been active since at least the 1960's [Oliver, 1962], and the glides are observed on data from 2004 to 2016, we infer that

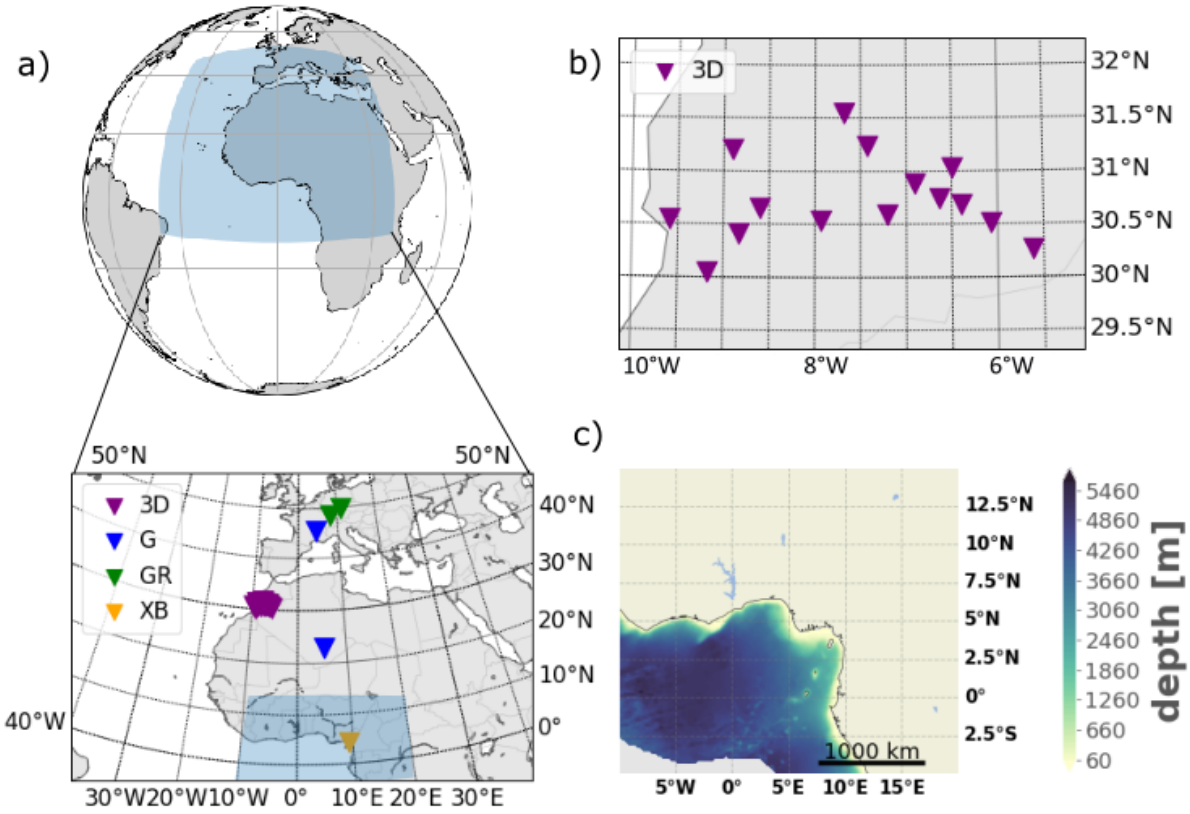

Figure 16: Study area and station locations. **a)** Study area in blue, with inset showing and location of seismic stations used in this study. **b)** Array geometry for the MM array in Morocco, consisting of 15 seismic stations used for beamforming. **c)** Bathymetry in the Gulf of Guinea.

both phenomena have been active for decades.

Using 19 particularly clean and energetic glides, we compare the slopes from the given time period from the permanent broadband station TAM, which tells us that the majority of the glides have similar slopes (Figure 17). This, together with the similar duration, points towards a common non-destructive physical process responsible for the seismic energy. The regular and repeatable, always upward gliding slope also limits the potential source mechanisms, for example excluding processes that include mass movement. A burst in the seismic energy of the 26 s microseism often precedes the glide, and continues after the glide has moved to higher frequencies, which supports a connection between the phenomena driving the glides and the 26 s source. Despite the change in frequency of the gliding tremor, the frequency

of the continuous signal remains stable. Hence, we have stable and varying spectral peaks generated simultaneously, likely emerging from the same, or coupled physical processes.

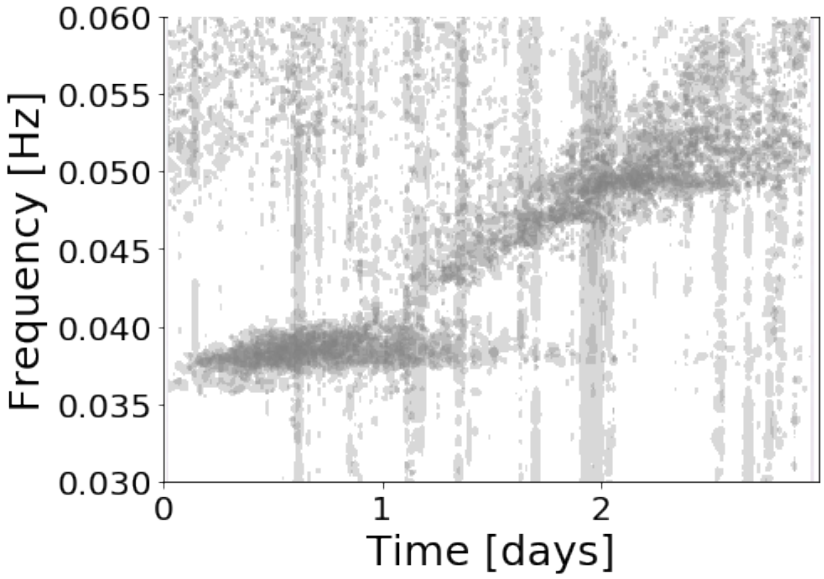

Figure 17: Repeated gliding tremor Comparison of slopes from 19 frequency glides recorded at TAM station from 2004 to 2016 is presented by superposing the the contour plots of spectral amplitudes higher than 1.75e-07 m. The glides exhibit a similar slope and are repeatable. The 26 s signal is also amplified before and after the glide.

Although the glides are the most prominent on seismic stations close to the Gulf of Guinea, the more energetic glides are also observed on quiet stations at great distance from the Gulf, including on stations in Europe. Seismic data from different stations in Europe and Africa (TAM, BFO, SSB, GRA1) exhibit the same 26 s spectral peak and simultaneous gliding. GRA1 is the furthest station from the source we consider here, so the tremor is detected at least up to a distance of around 4900 km. This is similar to the 26 s microseism, which occasionally grows strong enough to be detected globally. Such energetic bursts in the 26 s band usually lasts for hours and are as strong as a magnitude 5 earthquake [Xia et al., 2013].

To further constrain the relationship between the gliding and the continuous, 26 s signal, we use seismic array processing.

3.3 Are the two phenomena spatially connected?

We constrain the source region by applying three-component beamforming [Esmersoy et al., 1985, Riahi et al., 2013, Juretzek and Hadziioannou, 2016] using a temporary seismic array in Morocco (MM). The back projection along the estimated back azimuth points towards the Gulf of Guinea, and this dominant direction is equal for all 5 glides investigated from 2011 and 2012 (Table 7). In addition, there is no significant change in direction over the course of a glide. From this it follows that the signals are coming from a fixed location, and that this location is temporally stable over the two years investigated with array analysis. We also determine that this location is consistent with that found for the 26 s microseism [Holcomb, 1980, Shapiro et al., 2006, Xia et al., 2013]. Consequently, we infer that the two phenomena share a common source area.

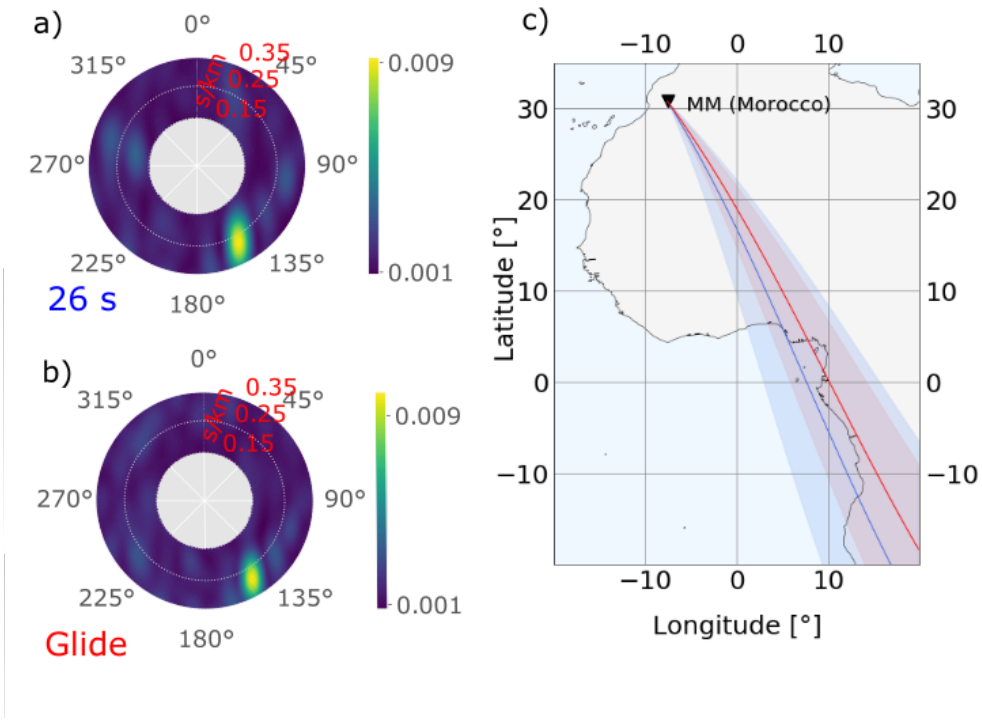

Figure 18: Projected back azimuth for the glide and 26 s source. The beam power as a function of slowness and back azimuth for the Rayleigh wave for the 26 s (blue, top) and the glide episode in January 2011 (red, bottom) is shown in (a) and (b), respectively. **c)** The back azimuth corresponding to the maximum beam power from the beamforming outputs points towards the Gulf of Guinea for the 26 s microseism and the glide, with uncertainties calculated from half of the maximum beam power.

3.4 Physical mechanisms for gliding tremor

Based on our observations, the physical mechanism generating the frequency glides should fulfill the following criteria: it should be repeatable, implying either reversibility or a recharge mechanism; it should be capable of continuously outputting energy for at least 60 years; it should be energetic enough to be observed globally; it should have a fixed location; and finally, since the glides are connected to the monochromatic, 26 s microseism in frequency, time and space, the mechanism should be able to generate both stable and varying frequency peaks simultaneously. In the following, we consider both oceanic and volcanic source mechanisms.

3.4.1 Ocean generated mechanisms

Linear gliding features in seismic spectrograms can be observed as a result of remote storms over the oceans. These storms generate ocean gravity waves, typically with periods ranging from 3 to 20 seconds [Bromirski and Duennebier, 2002]. When the dispersed ocean waves arrive at the coast, the low-frequency waves reach the shore first, followed by increasingly higher frequency waves [Haubrich et al., 1963]. As the swell couples into the seafloor and generate seismic waves, it produces a characteristic fan-like shape in seismic spectrograms, broadening towards higher frequencies, with a duration up to a few days [Chevrot et al., 2007]. The slope of the resulting shape gives an estimate of the distance to the storm [Bromirski and Duennebier, 2002]. Applying this to our glide on May 13th, we estimate a distance over 11200 km between storm and coast, which would place the storm in the south Pacific, south of the typical hurricane track latitudes [Knapp et al., 2010a]. The strong repeatability in our glide slopes would imply repeated storms at the same distance, if they were all to be explained by storm-generated seismic waves. Moreover, as the frequency of the ocean waves generated by a storm is determined by the wind speed [Pierson Jr and Moskowitz, 1964], intense storms with sustained wind speeds exceeding 20 m/s would be necessary to explain the low-frequency onset of our glides [Bromirski and Duennebier, 2002]. A comparison to meteorological data [Knapp et al., 2010a,b, Landsea and Franklin, 2013] does not show any correlation in storm occurrence and glide dates, even if global hurricane databases are considered, without restricting the occurrence to the South Pacific. We conclude that an oceanic origin for the frequency glides in the Gulf of Guinea is extremely unlikely.

3.4.2 Volcanic gliding tremor

Volcanic tremor is usually only recorded near the volcano, but can occasionally be observed globally [Cesca et al., 2020]. In addition, volcanic tremor typically occurs at much higher frequencies (1-5 Hz) and shorter duration (minutes) than the Gulf of Guinea gliding tremor [McNutt, 1992]. Still, long-lasting and long-period gliding tremor is detected at multiple locations [Hellweg, 2000, Dawson et al., 2010, Kawano et al., 2020]. However, in these cases, the change in frequency is irregular, not repeatable, with alternating frequency increases and decreases, in contrast to our linear upward glides. Whenever repeating upward gliding is observed, it is usually associated with volcanic eruptions [Hotovec et al., 2013, Lees et al., 2004, Lesage et al., 2006]. Although there are no known surface manifestations of volcanic eruptions in the area where the 26 s microseism and glide sources are located, it has been suggested that there are active volcanoes in the Gulf due to the persistent, localized and narrowband very long period tremors located in the gulf. [Xia and Chen, 2020] There is mud volcanic activity in the gulf [Graue, 2000], which can produce harmonic tremor [Franek et al., 2014]. However, such processes are usually only detected a couple of kilometers from the source and are unlikely to be energetic enough to produce the signals that we observe.

Here, we consider several mechanisms known to generate volcanic and hydrothermal tremor similar to those observed in this study. Processes known to generate volcanic tremor are (1) Resonating fluid-filled magma pathways (2) Repeated impulsive sources (3) Overpressure driven by gas accumulation (4) Combination of simultaneous mechanisms, similar to described by Unglert [2016]. Changes in frequency of volcanic tremor, such as the gliding we observe, are believed to reflect changes in source properties.

Resonating fluid filled-magma pathways

A fluid-filled resonator, for example gas resonating in a conduit, can explain the occurrence of harmonic tremor [Schlindwein et al., 1995, Kawakatsu et al., 2000] with the fundamental frequency (f_0) given by: $f_0 = c/2L$, where c is the acoustic velocity in the resonating medium, and L is the length of the crack or conduit [Hagerty et al., 2000].

In order to obtain a fundamental frequency of 0.038 Hz, even very low wave velocities would result in extremely large conduit lengths. For example, a velocity of 900 m/s (after Hagerty et al. [2000]) would give a length of 11.8 km. Chouet [1986] showed that a fluid-filled crack generates a very slow wave propagating along the crack wall. Even with such slow 'crack waves', the approximate resonator

size needed to generate 0.038 Hz is 6.6 km, for an assumed crack wave velocity of 500 m/s. To then change the tremor frequency, either the geometry of the conduit or the physical properties of the conduit materials should change A change in frequency from 0.038 Hz to 0.05 Hz would require a length change of more than 1.5 km in a matter of days, quickly resetting for the next glide to start (see figure 17). Due to the large dimensions required for such a resonator, the huge geometric changes necessary to explain the glides, and the strong repeatability of this process over decades, we conclude that the frequency glides are not likely due to changes in resonator length alone.

An alternative to geometric changes in the conduit are changes in the fluid properties, essentially changing the velocity. Small changes in gas fraction can produce large velocity changes [Lesage et al., 2006], and hence changes in the resonator frequency, which are easily reversible and can therefore accommodate the observed repeatability of the glides. For example, new material being injected into the conduit can produce repeated narrow band gliding tremor with roughly linear increase in frequency, which is observed at underwater volcanoes prior to eruptions [Searcy, 2013]

The injected material increases the gas content, which in turn decreases as gas is released from the vent, thus changing the wave velocity in the magma [Searcy, 2013, Dziak and Fox, 2002]. However, gliding observed tremor attributed to such changes in gas fraction typically has a short duration of minutes. Such a mechanism can explain a short tremor sequence leading up to an eruption, but to explain the glides in the Gulf of Guinea, we would need a constant flow, with injection and expulsion of material in a repeatable manner over the course of decades.

Tremor-like signals are also associated with hydrothermal systems [Kawakatsu et al., 2000, Ohminato, 2006]. For example, long period tremor with $\pm$15 s period is detected continuously at Aso, even when there is no surface activity. This tremor is attributed to inflation and deflation of a shallow water filled crack with a length of approximately 1 km, and it differs from the 26 s signal in its short duration of less than a minute [Kawakatsu et al., 2000, Yamamoto et al., 1999].

Nayak et al. [2020] reported gliding harmonic tremor at the Lone Star Geyser, Yellowstone. Boiling groundwater generates seismic energy through bubble growth and collapse. If the boiling is contained in a conduit, this process can excite the conduit into resonance and produce harmonic tremor [Leet, 1988]. The length of the conduit needed to excite a given frequency is given by the same equation as for a magma filled resonator, above, where c is the sound velocity in groundwater. Using a velocity of 50 m/s, the lowest velocity considered by Leet [1988], would give a conduit length of around 650 m, which is the

minimum size needed for such a system to excite a fundamental frequency of 0.038 Hz. A hydrothermal system thus gives more realistic length estimates than a magmatic system. However, for this mechanism, we need access to groundwater as well as a heat source below the groundwater table. Moreover, the system has to be shallow (source depth less than a few kilometers) to allow the vapor to separate from the fluid [Leet, 1988]. Seeing as the source location for our 26 s microseism and glides are beneath a $>$3 km layer of water, the pressure conditions for such a hydrothermal system would not be ideal.

Regular repeated sources

A repeated source, spaced regularly in time, such as earthquakes or repetitive pressure transients, are also known to produce a harmonic-like tremor [Hotovec et al., 2013, Lesage et al., 2006, Lees et al., 2004]. As the pulses move closer together, the harmonic tremor glides to higher frequencies. When the pulse spacing drifts further apart, the tremor glides to lower frequencies. To test this mechanism, we produce a synthetic model of repeated pulses. To fit our observations, the trigger frequency needs to gradually change from 0.038 Hz to 0.05 Hz, with a lag time between the pulses equal to the inverse of the frequency (see figure 38). Gases escaping through narrowing channels are a potential source of such repeated pressure pulsation, as shown by Julian [1994].

Overpressure driven by gas accumulation?

A physical model that can explain repeatable, upward glides in a volcanic setting is gas accumulating under a solid cap. Pressure builds up, until it overcomes the strength of the cap, producing a pressure pulse and resulting seismic signal as the volcanic fluids are released. After the gas is released, another cap starts to form. The signal stops as the top of the magma column has solidified, and the process repeats [Tepp and Dziak, 2021, Chadwick Jr et al., 2008]. In our case, we require a system that can reset quickly in a repeatable manner, which would require a constant availability of material to form a new cap. It is unlikely for such a situation to stay the same over decades.

According to Hellweg [2000], similar to gases leaking from a slightly opened soda bottle, gases escaping slowly from a reservoir closed off by a fractured plug can cause a cycle of pressure drop and bubble formation. In this case, the changing frequency would be governed by small, easily reversible changes in flow velocity, instead of changes in the geometry of the conduit, thus enabling repeatability of the glides. If the magma reservoir is large, we would have access to a large supply of gas, allowing the resulting tremor to continue for a long time. If the periodic degassing happens at depth, we might not be able

to see the effects at the sea surface. With the help of satellite data (sea surface height from Jason-3, Sentinel-3A, HY-2A, Saral/AltiKa, Cryosat-2, Jason-2, Jason-1, T/P, ENVISAT, GFO, ERS1/2 [CLS (France), 2012] and sea surface temperature from OSTIA SST analysis combining satellite data from the GHRSST project and in-situ observations to determine sea surface temperature [CNR (Italy), 2009]) we searched for evidence of sea surface disturbance by rising bubbles at the time of several glides, and did not detect anything. The mechanisms described above could potentially explain our repeatable, upward gliding tremor, but we need an explanation for the simultaneous monofrequent signal as well. To explain the two phenomena, one tremor mechanism might not be sufficient.

Combination of simultaneous mechanisms

Different mechanisms can produce similar signals, and multiple mechanisms can be active simultaneously in the same volcanic system for the same eruption [Soubestre et al., 2021, Lesage et al., 2006]. Stable and varying frequency peaks existing simultaneously have previously been observed at Kilauea. The stable, long-period peak was explained as the breathing mode of the volcanic system caused by synchronous inflation-deflation of cracks, while the variable higher frequency peak were interpreted as higher modes of resonance of the system Dawson et al. [2010]. The continuous, stable peak at 26 s that we observe coming from the Gulf of Guinea could be a result of a large, magmatic or hydrothermal system, such as a reservoir, continuously degassing, exciting the system into resonance, while the frequency glides could be related to the gas escaping through a narrow conduit.

The clarinet model proposed by Lesage et al. [2006] to explain the tremor observed at Arenal, consists of a conduit closed of by a fractured plug. Harmonic tremor is produced by repetitive pressure pulses, which a repeat period that stabilizes through feedback with the resonance of the conduit. Such a feedback mechanism could explain why our glides start at the same frequency as the 26 s microseism, with the source of the glide possibly being connected to or controlled by the 26 s source.

Our suggested mechanism

A picture is starting to emerge: we propose a hydrothermal system consisting of a layered structure or channel with a minimum length of 650 m, likely much larger, that is set into resonance by an internal mechanism such as boiling groundwater or gas release. The channel is sealed off by a fractured plug that acts as valve through which gas can escape intermittently, thereby producing pressure pulses with

a repetition period stabilized by the resonance of the channel.

Since the source is hidden from view and there are no known surface manifestations such as gas bubbles, sea surface disturbances or thermal anomalies, it is difficult to confirm that degassing occurs at depth. Although the discovery of the frequency glides provides us with another piece of the puzzle surrounding the 26 s microseism, it still raises more questions than it answers. There is still no physical model that can explain the glides in terms of repeatability, strength, linear change in frequency, and duration of the glides, nor can we explain how energy can be released in such a stable manner for decades. Moreover, no existing model can adequately explain both the glides and the 26 s signal simultaneously. Regardless, the astonishing nature of the Gulf of Guinea tremors forces us to broaden our thinking about the mechanisms and systems causing gliding tremor, and about the mysterious signals the Earth produces.

Acknowledgements

We are grateful to Joachim Wassermann, Éléonore Stutzmann, Lise Retailleau, Christoph Sens-Schönfelder, Torsten Dahm and Stephen McNutt for helpful discussions and comments. We would also like to thank Stefan Kern for assisting with satellite data.

3.5 Methods

Data availability and processing

To study the glide episodes, we use available data from permanent three-component broadband stations in Germany (BFO, GRA1) from the national seismological network in Germany (GR) [Federal Institute for Geosciences and Natural Resources, 1976], and France (SSB) and Algeria (TAM) from the global seismological network GEOSCOPE (G) [Institut De Physique Du Globe De Paris (IPGP) and Ecole Et Observatoire Des Sciences De La Terre De Strasbourg (EOST), 1982]. We also use data from station CM15 from the temporary installation Broadband Seismic Investigation of the Cameroon Volcanic Line (CVL) [Douglas Wiens, 2005], from 2006. Three-component data from the Morocco-Muenster array (MM), a temporary array located in Morocco from 2011 to 2013 [Thomas, 2010], is used for three-component beamforming. All data is available through FDSN.

The data used for beamforming is processed in 1-day segments. First, the daily traces are corrected for

instrument response and resampled to 1 Hz. Then, the mean and trend are removed, and the traces are band-pass filtered between 0.01-0.06 Hz.

To remove the influence of earthquakes, we use a catalog of global earthquakes. The catalog includes global earthquakes above M=5.5, and is based on the ISC On-line Bulletin [2021]. Following the approach of Tanimoto et al. [2016], after each earthquake we removed a section of the signal. The length of the removed section was adapted to the magnitude of the earthquake, removing particularly long time windows after high magnitude earthquakes to account for the excitation of the normal modes of the Earth. We remove 6 hours for earthquakes between magnitude 5.5 and 6, starting at the time of the earthquake. For magnitudes up to 8, 12 hours are removed, above magnitude 8 we remove 24 hours, and for earthquakes larger than magnitude 9 we remove 36 hours. To further eliminate the effects of smaller, local earthquakes and spikes in the data, an STA/LTA trigger is also included with STA=500 s and LTA=24 hours. All data processing is done with ObsPy [Beyreuther et al., 2010, Krischer et al., 2015, Team, 2020].

3-component beamforming

We use a three-component beamforming method [Esmersoy et al., 1985] in the frequency domain to separate between differently polarized waves and obtain estimates of beam power, direction of arrival (back azimuth) and slowness of the incoming coherent signals. The method has previously been applied to ambient noise by Riahi et al. [2013], Juretzek and Hadziioannou [2016, 2017] and Löer et al. [2018]. For detailed description of the method, we refer to Riahi et al. [2013]. We perform beamforming on 500 s time windows, with slowness increments of 0.02 s/km and 2 degree steps for back azimuth for both Rayleigh and Love waves. The beam power spectral density is normalized by the average station power spectral density of all components. The beam power is calculated for 10-hour-intervals at frequency f=0.038$\pm$0.001 Hz and f=0.048$\pm$0.001 Hz, in order to separate between the glides and the 26 s microseism. For each beamformer output, the back azimuth corresponding to the maximum beam power is selected.

Array configuration and limitations

To evaluate the performance of the Morocco array [Thomas, 2010], we evaluate the beam power in the case of a single monochromatic plane wave coming from right below the array. The resulting beam power is called the array transfer function, and is affected by number of stations, spatial configuration

and array aperture. The main lobe of the transfer function represents the power distribution in the true arrival direction of the signal, while the side lobes are the energy contribution at other slownesses. An ideal transfer function thus has a narrow main lobe, with low power contribution from the side lobes [Gal and Reading, 2019]. Figure 19 shows the resolution capability of the Morocco array at a frequency of 0.038 Hz and 0.048 Hz for the array geometry shown in Figure 16. The array transfer function slightly differs at different frequencies, but the effect is not strong enough to affect our results.

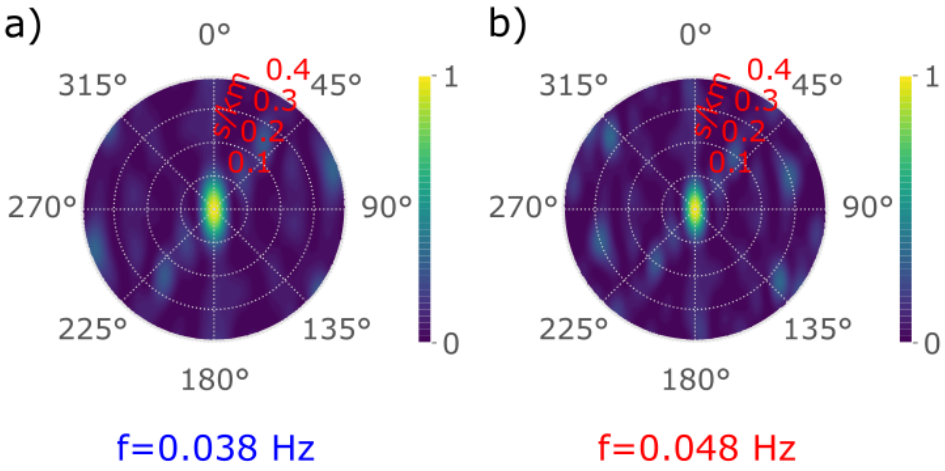

Figure 19: Beamforming resolution The resolution capabilities for the Morocco (MM) array for 0.038 Hz and 0.048 Hz, i.e. for the 26 s signal and the glide, is shown in **a)** and **b)** respectively, for the array geometry is given in Figure 16.

4 New insights into the source mechanism for the 26 s microseism from three component beamforming

Charlotte Bruland[1], Celine Hadziioannou[1], Sarah Mader[1,2]

[1]Institute of Geophysics, Center for Earth System Research and Sustainability (CEN), Universität Hamburg, Hamburg, Germany

[2]Karlsruher Institut für Technologie, Karlsruhe, Germany

Abstract

The distribution of ambient noise sources affects the outcome of ambient-noise based methods. Better constraints on location and behaviour of noise sources will help us understand the processes driving them and improve our applications of ambient noise. One of the most enigmatic noise sources is the 26 s microseism. This very monochromatic source was identified in the 1960's and is believed to be generated continuously from a fixed location in the Gulf of Guinea. The physical mechanism behind this signal is still unknown. We investigate the source characteristics of the 26 s signal using seismic data from Africa and Europe for spectral analysis and three component beamforming. The source is detected intercontinentally approximately 25 percent of the time, with no clear seasonal variation. Bursts of energy in the 26 s signal display a strong correlation with a very low frequency, long duration and repeatable gliding tremor. Our array analysis shows that the 26 s microseism and gliding tremor originate in a common, fixed source location in the Gulf of Guinea. Both sources excite Love and Rayleigh waves and are detected at large distances from the gulf. The very low frequency, the time scale of decades of which the sources appear to have been active and the repeatability of the glides cannot be explained sufficiently by known physical mechanisms. We propose a combined source mechanism for the simultaneous excitation of the frequency gliding and the 26 s microseism consisting of a hydrothermal or magmatic system composed of a fluid-filled conduit, with a natural period of 26 s, and a valve mechanism controlled by feedback with the resonance of the conduit. Our results point towards a phenomenon that occurs on a large spatial scale. The implications for repeatability and the size of the volcanic system and the mechanisms involved, challenges our understanding of volcanic tremor. Since volcanic tremor is an important tool to monitor volcanic activity, this may have an impact on monitoring volcanic activity in the future.

4.1 Introduction

Seismometers all around the world continuously record faint vibrations, which are mainly generated by ocean waves, known as ambient noise. Through cross-correlation of ambient seismic noise, we can retrieve information about the subsurface [Shapiro and Campillo, 2004, Sabra et al., 2005a]. Some ambient noise signals are temporally persistent and generated by spatially localized sources. Such persistent localized sources can affect the outcome of ambient noise-based methods [Shapiro et al., 2006, Zheng et al., 2011], but can also be used for imaging [Xie et al., 2021]. Better constraints on location and behaviour of noise sources will help us understand the processes driving them and improve our applications of ambient noise.

A well known example of such a persistent localized source is the 26 s microseism, identified by Oliver [1962]. This enigmatic signal is recorded on stations globally, with energy coming from the Gulf of Guinea [Holcomb, 1980, Shapiro et al., 2006, Xia et al., 2013]. The source has apparently acted continuously since it was discovered in the 1960's, with a constant peak period and bandwidth, and varying amplitude. Adding to the mystery, a weaker source with similar spectral characteristics was found at approximately the antipodal location of the previously reported source [Shapiro et al., 2006]. Nevertheless, it was shown to be independent from the source in the Gulf of Guinea and the likely source is the Ambrym volcano in the Vanuatu islands [Zeng and Ni, 2014, Kawano et al., 2020]. The physical cause of the 26 s microseism in the Gulf of Guinea is still enigmatic to date.

In this paper we explore the temporal evolution of the 26 s microseism in order to get closer to resolving the source mechanism responsible for the signal. Firstly, we use spectral analysis of data from permanent seismic stations in Africa and Europe to study the temporal distribution of days when the 26 s peak is coherent intercontinentally and seasonal variation. Then we apply 3-component beamforming to seismic data from three temporary arrays in Africa in order to determine the location of the source, location stability and wave types excited. Lastly, we investigate the connection between the 26 s source and gliding tremor source in the Gulf of Guinea.

4.2 When is the 26 s peak coherent on stations intercontinentally?

4.2.1 Data and pre-processing

To investigate the source characteristics of the 26 s microseism, we use data from permanent three-component broadband stations in Germany (BFO, GRA1), France (SSB) and Algeria (TAM). (Figure 20 a)) All seismic data used in this work is available through FDSN, and details for the different stations is provided in Table 8. We study the 26 s source from 2004 to 2016. Figure 20 b) shows the 26 s peak on TAM for the given time period.

We use ObsPy [Beyreuther et al., 2010, Krischer et al., 2015, Team, 2020] for pre-processing of the data. The data is processed in 1-day segments, and the daily traces are first corrected for instrument response and resampled (1 Hz). Then mean and trend is removed, and the data is filtered between 0.01-0.06 Hz. We use a global earthquake catalog to remove the influence of earthquakes in our data. The catalog includes global earthquakes above M=5.5 and is based on the ISC On-line Bulletin [2021]. We remove a section of the signal after each earthquake, following the approach of Tanimoto et al. [2016]. For earthquakes between magnitude 5.5 and 6, 6 hours is removed, starting at the time of the earthquake. For a magnitude between 6 and 8, 12 hours of data was removed, between 8 and 9 , 24 hours is removed. Above magnitude 9, we remove 36 hours. To further enhance the 26 s signal, we remove the effect of smaller, local earthquakes, as well as spikes in the data, by including an STA/LTA trigger with STA=500 s and LTA=24 h.

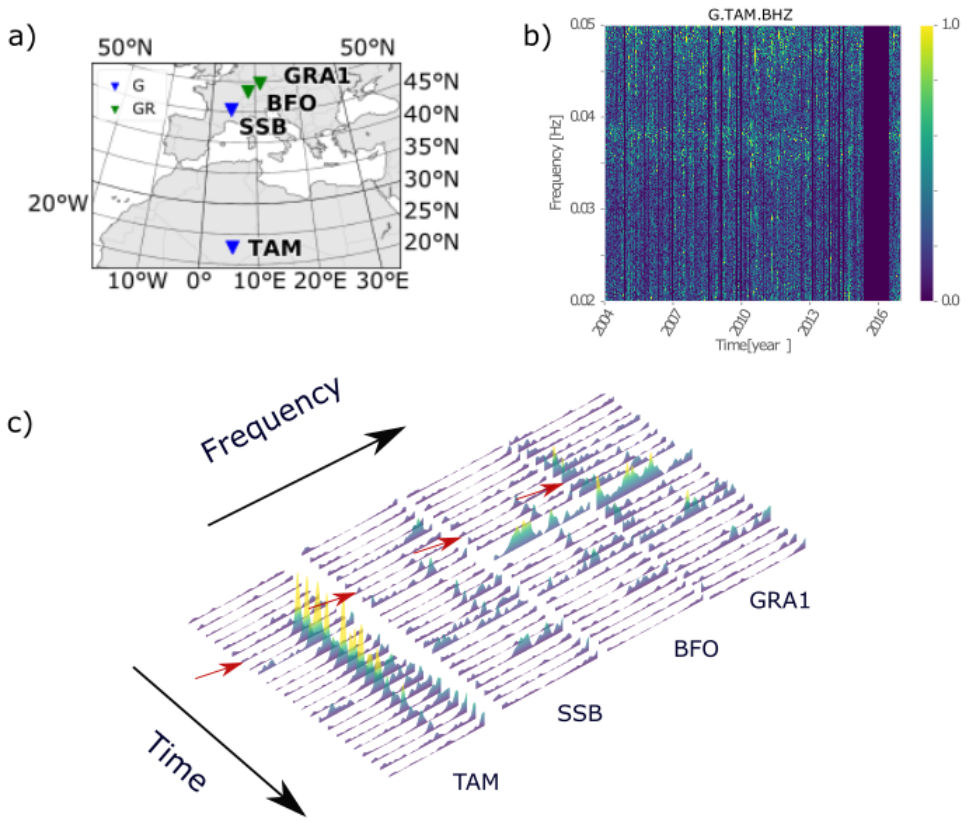

Figure 20: 26 s peak: a) Location of permanent 3-C broadband stations used for burst detection. b) Normalized spectrogram for vertical component data from TAM 2004 to 2016. The 0.036 and 0.038 Hz spectral lines appear persistently in the data with stable frequency and bandwidth, so the source is active and steady throughout this time. c) Amplitude spectra over time for TAM, SSB, BFO and GRA1 for a burst event January 6th 2013. Each spectra corresponds to 2 hours of data. The peak is visible on all stations. There is a strong variation in spectral amplitude over the 48 hours displayed.

4.2.2 Detection of spectral peaks

Occasionally the 26 s signal grows so strong it is detected on seismic stations globally. Such bursts of energy typically lasts for hours [Xia et al., 2013]. We define a burst as when the peak is detectable on stations TAM, GRA1, BFO and SSB simultaneously. Figure 20 c) shows the spectral amplitude variation for such a burst on 4 stations in Africa and Europe (TAM, GRA1, BFO, SSB). The peak is the most prominent on TAM, which is the closest to the source, but the bursts can also be detected on the stations in Europe. However, even in the absence of such energy bursts, the continuous 26 s spectral

line is often observed across Africa and Europe.

To find out when and how often the 26 s peak is detected on stations across continents, we correlate the amplitude spectra of the four permanent broadband stations (SSB, GRA1, TAM, BFO). We focus on the frequencies surrounding the 26 s-microseism by applying a band pass filter between 0.02 and 0.05 Hz. One-day-segments are used to calculate each spectrum, to ensure a good frequency resolution while keeping the ability to detect daily spectral changes. If less than 4 hours of data are available for a given day, that day is not considered. The correlation matrix for the four stations' spectra is calculated for different overlapping frequency intervals of 0.002 Hz, using the Pearson correlation coefficient, and the mean and standard deviation for each correlation matrix is calculated. Each value is assigned to the center frequency of the window, so we obtain the mean of the correlation as a function of frequency, with corresponding standard deviation. When a spectral peak is coherent on all four stations, that results in a high value for the mean correlation coefficient at this frequency. A spectral peak is therefore automatically identified if the jump between neighboring frequencies is larger than the standard deviation, or if the average of a portion of the spectrum (0.005Hz) is larger than the overall average. This approach identifies coherent spectral peaks between 0.02 and 0.05 Hz, and is not constrained to the 26 s peak. In order to evaluate whether any seasonal variation in burst occurrence exists, we carry out detection for five years (2004, 2006, 2011, 2013, 2016). These years were chosen to coincide with the availability of array data used in this study.

4.2.3 Temporal distribution and seasonal variation of the 26 s signal

The combined results from the peak detection carried out for five years (2004, 2006, 2011, 2013, 2016) is presented in Figure 21. While most detections are centered around 0.038 Hz ($\pm$26 s), two distinct horizontal lines form at around 0.036 and 0.038 Hz. For 2004, 2006, 2011, 2013 and 2016, coherent peaks were identified 26%, 28%, 24%, 32% and 19% of the time, respectively. Overall, we assume that the 26 s peak can be observed on seismic stations intercontinentally approximately 25 % of the time. 2016 only covers 4 months of data, and therefore may not be as representative as the other years.

The number of detections does not display any clear seasonal variation over the five years presented here. Although the mean frequency does not change significantly over the seasons, the detections are more

scattered in frequency for (northern hemisphere) winter months (Figure 39a, supporting information). The amplitudes of the coherent peaks are higher in winter months than summer months, and the values for spectral amplitude vary more in the winter months (Figure 39b, supporting information). However, the higher amplitude detections are often associated with higher frequency picks which have a higher occurrence during winter months, and do not correspond to coherent peaks around 0.036 and 0.038 Hz. The amplitude of the 26 s peak is close to the amplitude of the surrounding noise levels, and spectral peaks may drown in the noise, which can have an effect on the number of detections that are actually from the 26 s peak. This effect is stronger in winter, when higher ambient noise levels are present towards the upper half of our considered period band (e.g. Stutzmann et al. [2009]). To illustrate, a comparison of the daily spectral amplitude for July and January for the years used in our peak detection is shown in Figure 21 with a spectral peak detected on July 2nd 2006. Overall, the amplitude of detections is stable for the five years. This effect may be the reason for the more scattered spectral peak detections in winter.

While the spectral amplitude and frequency of the 26 s peak itself appears to be stable over the seasons, a glide towards higher frequencies is associated with the bursts of energy we sometimes observe on the 26 s peak (see Section 4.4). Both signals are detected on all three components of the seismic stations.

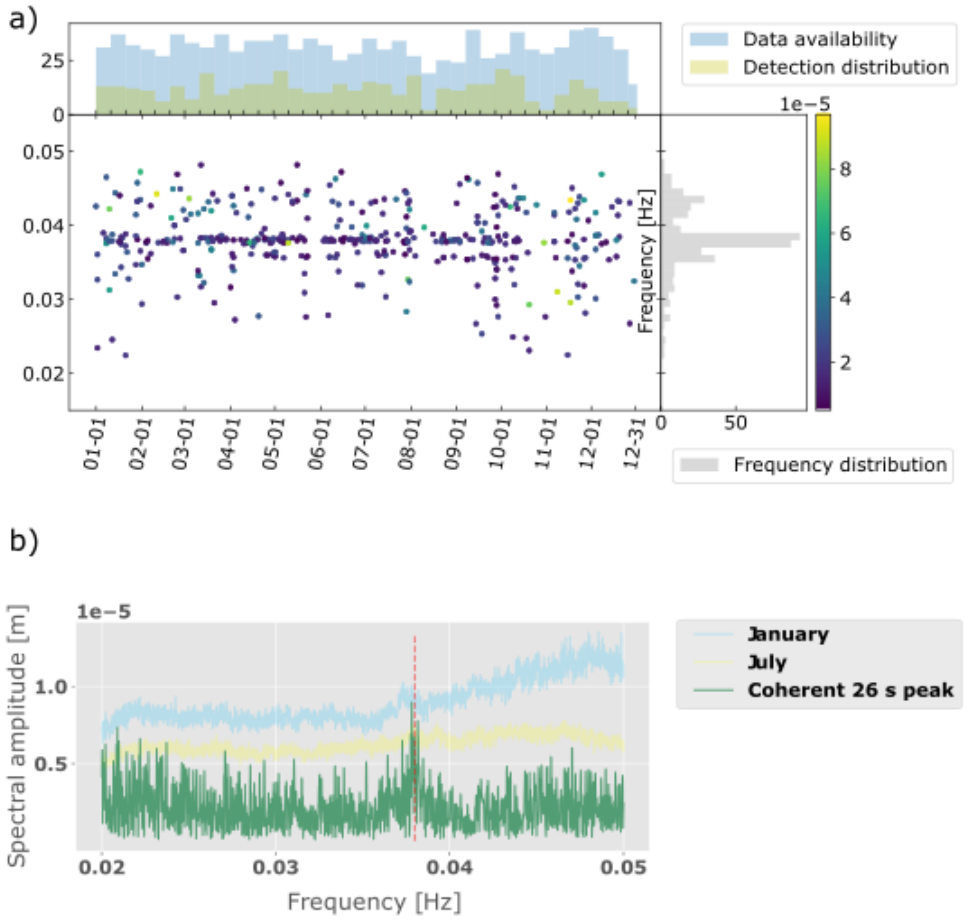

Figure 21: Results of spectral peak detection: a) Combined results for five years (2004, 2006, 2011, 2013,2016) of peak detection for vertical component data. Detections are centered around 0.038 and 0.036 Hz, especially during summer months, and the spectral amplitude of the spectral peaks is stable. b) The averaged daily spectrum for January (2004, 2006, 2011, 2013, 2016) in blue and the spectrum for July for the same years in yellow, with a vertical line at frequency equal to 0.038 Hz. The spectrum for a 26 s-peak on 2006-07-02 is shown in green. Since the amplitude of the peak is so close to the amplitude of the surrounding noise levels, such peaks are more likely to go undetected during the winter months.

4.3 Source location and wave types

4.3.1 Arrays and array processing

We apply array processing on three-component data from seismic arrays in Africa to obtain wave types excited and source location for the 26 s source. The data is from the temporary installation Broadband Seismic Investigation of the Cameroon Volcanic Line (CVL) [Douglas Wiens, 2005] from 2006, the Morocco-Muenster array (MM), a temporary array located in Morocco from 2011 to 2013 [Thomas, 2010] and the Network of Autonomously Recording Seismographs (NARS) 2016 [Utrecht University (UU Netherlands), 1983]. The data is from different time spans for the different arrays. A description of the arrays is provided in Table 9. All data is available through FDSN, and is pre-processed as described in part 4.2.1.

3-C beamforming

We use a three-component beamforming method [Esmersoy et al., 1985] in the frequency domain to differentiate between Rayleigh and Love waves and to obtain estimates of beam power, direction of arrival and slowness of the incoming coherent signals, which was previously applied to ambient noise by Riahi et al. [2013], Löer et al. [2018] and Juretzek and Hadziioannou [2016, 2017].

We assume a point source in the far field where the resulting wave front passes over the array as a straight line. For classical plane wave frequency-wave number beamforming, the beam power for an array consisting of N stations can be expressed as a function of frequency (f), back azimuth (θ), slowness (s) and polarization (ρ) by:

$$P(f,\theta,u,\rho) = \frac{1}{N^2}\mathbf{w}^*_{3N}(f,\theta,u,\rho)\mathbf{R}_{3N}(f)\mathbf{w}_{3N}(f,\theta,u,\rho), \tag{18}$$

where $\mathbf{R}_{3N}(f)$ is the cross-covariance matrix of the Fourier transform of the three-component data, $*$ is the conjugate transpose operator and $\mathbf{w}_{3N}$ is the weight vector given by:

$$\mathbf{w}_{3N} = [p_x e_1, ..., p_x e_N; p_y e_1, ...p_y e_N; p_z e_1, ..., p_z e_N]^T, \tag{19}$$

where $\mathbf{e}_N$ contains the delays for each sensor due to wave propagation and $\mathbf{p}_{xyz}$ contains the amplitude factors and delays for each component due to the polarization. We refer to Riahi et al. [2013] for a detailed description of the method.

The beamforming is carried out for 500 s windows, searching in increments of 0.02 s/km for slowness and 2 degree steps for back azimuth for both Rayleigh and Love waves. For Rayleigh waves we assume elliptical retrograde polarization and transverse polarization for Love waves. The amplitudes are disregarded and the beam power spectral density is normalized by the average station power spectral density of all components. The results are calculated for 1 day intervals and for frequency $f = 0.038 \pm 0.001$Hz. We focus on results that are inside of the expected surface wave slowness range($0.2s/km < s < 0.3s/km$). For each stacked 1-day and 10-day beamformer output, the slowness and back azimuth corresponding to the maximum beamformer power is selected, which is referred to as the dominating direction. The resolution and geometry for the different arrays can be found in Figure 40.

4.3.2 What types of waves are excited?

Since 3-C beamforming serves as a wave filter, we can use it to determine what wave types are radiated by the source. The source has previously been shown to emit Rayleigh waves [Oliver, 1962, Holcomb, 1980, Shapiro et al., 2006], which is confirmed by our array processing (Figure 22). Figure 22 shows the beampower as a function of slowness and back azimuth assuming Rayleigh waves for the MM, CVL and NARS array respectively. Whenever Rayleigh waves are detected on the MM array, Love waves coming from the same direction are also detected (Figure 22), hence the source emits both Love and Rayleigh waves. We get a Rayleigh wave velocity between 3.5 and 3.7 km/s and a Love wave velocity of 3.8-4.1 km/s. For the NARS and CVL array, noise levels usually do not permit the detection of Love waves, but Rayleigh waves are detected for both arrays (Figure 22). We look at the back azimuth over longer time scales to see if the results are stable.

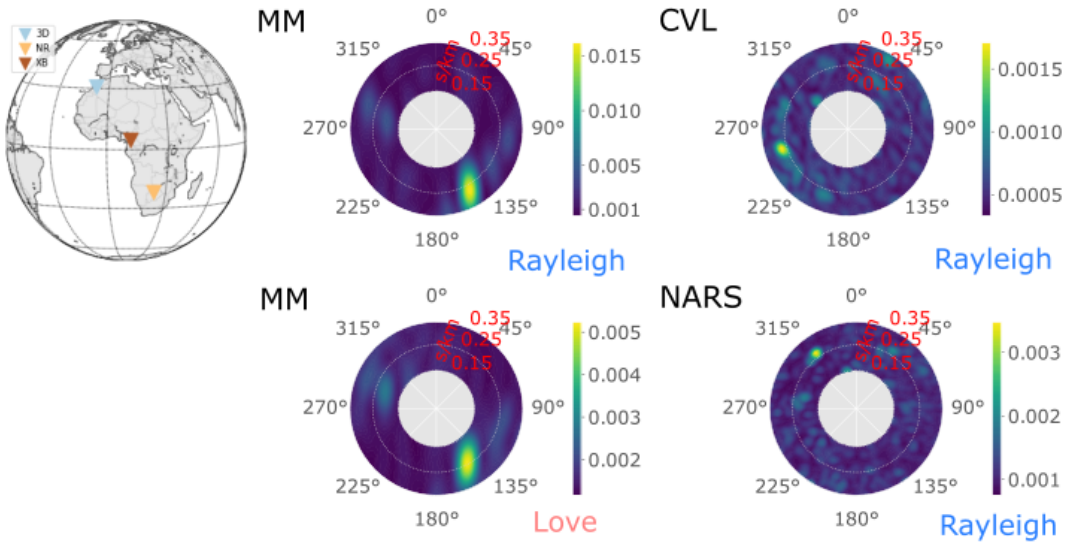

Figure 22: Beamforming for the 26 s source: The beam power as a function of slowness and back azimuth is calculated for 1 day of data for the arrays shown in a). MM array 2013-01-06 for Rayleigh (b) and Love (d) waves display the same dominating direction. Rayleigh waves are detected on CVL for 2006-05-13 (c) and NARS for 2016-01-28 (e)

4.3.3 Location stability

Our beamforming results are stable for the years investigated (Morocco 2011-April 2013) and Cameroon (May 2006). The results for the Morocco array for the entire year of 2011 for Rayleigh waves is displayed in Figure 23a). There is minimal variation in dominating direction for both Love and Rayleigh waves. The temporally stable back azimuth points towards a stationary source for the 26 s microseism. Therefore, the extracted back azimuths from the three arrays can be used to constrain the source location by triangulating the results from the different arrays, even though the data is collected from different time spans. The beamforming results from all arrays intersect the Gulf of Guinea (Figure 23b)). Another enigmatic phenomenon also appears to originate in the gulf; every so often a gliding tremor occurs.

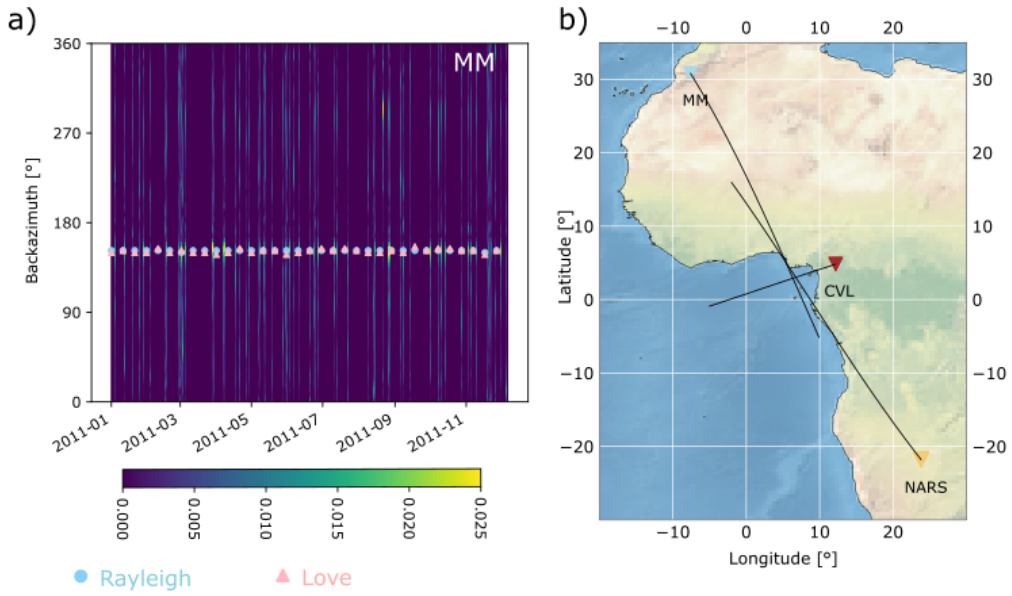

Figure 23: Fixed source location in the Gulf of Guinea: a) The beampower as a function of time and backazimuth for the Rayleigh wave for data from 2011 on the Morocco array (MM). The back azimuth corresponding to the maximum beampower for each 10 day segments is selected for Love (pink triangle) and Rayleigh waves (blue circle). This dominating direction is temporally stable for both wave types. b) Location of the 26 s microseism from triangulating results from 3-C beamforming.

4.4 Gliding tremor

The occasional frequency glide signal is observed on all permanent seismic stations used in our study (TAM, SSB, GRA1, BFO). The signal is emergent (Figure 41), starts at the same frequency and often accompanies a burst in the 26 s microseism. From previous work (Section 3), the gliding tremors have the following characteristics: 1) they have a long-duration (days), 2) they are narrow band, 3) they are low frequency with an almost linear increase in frequency from 0.038 to about 0.05 Hz and 4) always glide upwards. An example of such a glide on the MM array is shown in Figure 24. In most cases, the signal is harmonic. However, in the example selected here, the signal is inharmonic with a frequency higher than two times the fundamental, suggesting a non-linear phenomenon. This emphasizes the complexity of the source. Other variations of non-harmonic gliding peaks are shown in Figure 34 and 35. We detect these glides for all years investigated in this study on the permanent station TAM, so the gliding tremor appears to result from a long-lived process. Comparing 12 glides from 2004 to 2013 from TAM (white dots) reveals that the slope does not change significantly over this time period, pointing towards a common source mechanism for the glides that is repeatable and non-destructive. The slope of the glides detected at TAM also matches well with the slope of the glide detected at the MM array, so the frequency content of the signal does not change depending on the distance traveled to the station. Looking at the glide occurrence on TAM, it varies from year to year, however there is no clear pattern in this variation. Similar to the bursts of energy in the 26 s band, there is a seasonal variation in glide occurrence, with more glides observed in the summer months, but this is likely also due to changes in noise level on TAM, not changes in glide activity. The occurrence of bursts and glides per year displays a clear correlation, so the phenomena appear to be related (Figure 25).

To constrain the source location of the gliding tremor, we again apply 3-C beamforming but at a higher frequency to be able to separate between the glide and the 26 s signal. The beam power is calculated for 10-hour-intervals and 3-hour-intervals at frequency f=0.048$\pm$0.001 Hz and f=0.05$\pm$0.001 Hz, for the Morocco and Cameroon array respectively. Our beamforming results show that the source also emits both Love and Rayleigh waves. For each beamformer output, the back azimuth corresponding to the maximum beam power is selected. The projected back azimuth points towards the Gulf of Guinea (Figure 26d)). This dominant direction is equal for all 5 glides investigated from 2011 and 2012 on the Morocco array, suggesting that the gliding tremor also has a fixed source location. From the similarity

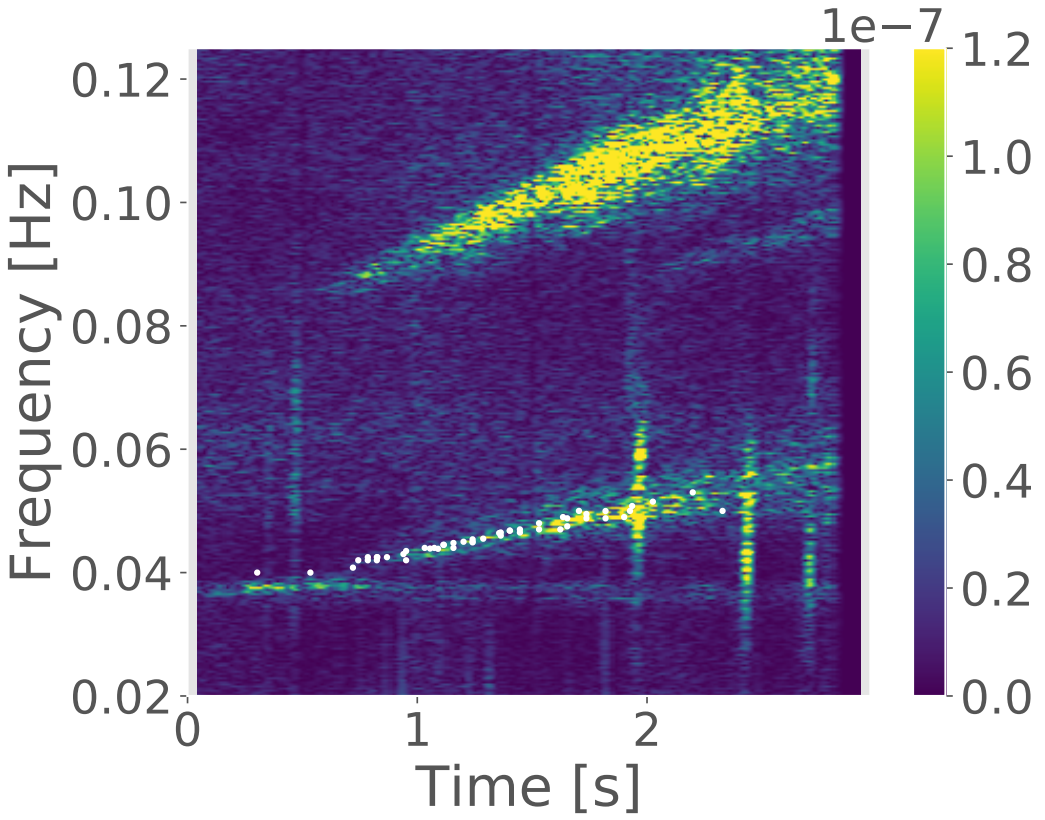

Figure 24: Gliding tremor: We use the velocity (3.7 km/s) and the backazimuth (152 degrees) obtained from beamforming to delay and sum the traces from the stations of the Morocco array to enhance the gliding tremor on 2012-07-30. Here we show the spectrogram of the resulting stacked waveform computed for 2 hour windows. The white dots represent the picked peak frequency from 12 glides on TAM from 2004 to 2013. The slope of the glides does not change significantly for the different glides, suggesting a common source mechanism. This slope also matches well with the slope of the glide detected on the Morocco array.

between the results for the 26 s source (0.038 Hz) and the glide (0.048/0.05 Hz) it appears that the two sources are spatially connected.

Figure 25: a) Number of glides detected on TAM for the years used for spectral peak detection. b) Correlation of glide occurrence versus spectral peak occurrence. The red line shows a linear regression weighted by the amount of data available (shown different sizes depending on data availability). The spectral peak and glide occurrence is clearly correlated.

4.5 Discussion and conclusion

We show that the 26 s tremor has stable properties for the 5 years investigated and that it is detected globally about 25 percent of the time. The seismic waves originate from a fixed location and contain both Love and Rayleigh waves. This has the following implications for possible source mechanisms: the source process should be capable of having stable source properties over the course of years, with a fixed location and energetic enough to be observed globally/continuously outputting enough energy to be observed globally for decades. Processes known to produce such energetic sustained seismic signals over such time scales are mainly of oceanic origin.

4.5.1 Ocean generated mechanisms

Ocean waves typically have a central period of 15 seconds over open oceans. Higher windspeeds are associated with longer periods [Pierson Jr and Moskowitz, 1964]. For the continuous 26 s signal, we would need ocean waves of 26 s or 52 s for primary and secondary microseism generation respectively. Longer period ocean waves also necessite a longer fetch, suggesting that a very large open body of water is needed to allow 26 or 52 s surface waves to form.

We consider the optimal depths for 26 s microseism generation. The generation of primary microseism depends on the gravity wave wavelength, wave amplitude and local bathymetry. Ocean gravity waves mainly couple into the seafloor at shallow water depths, and the depth where you would expect

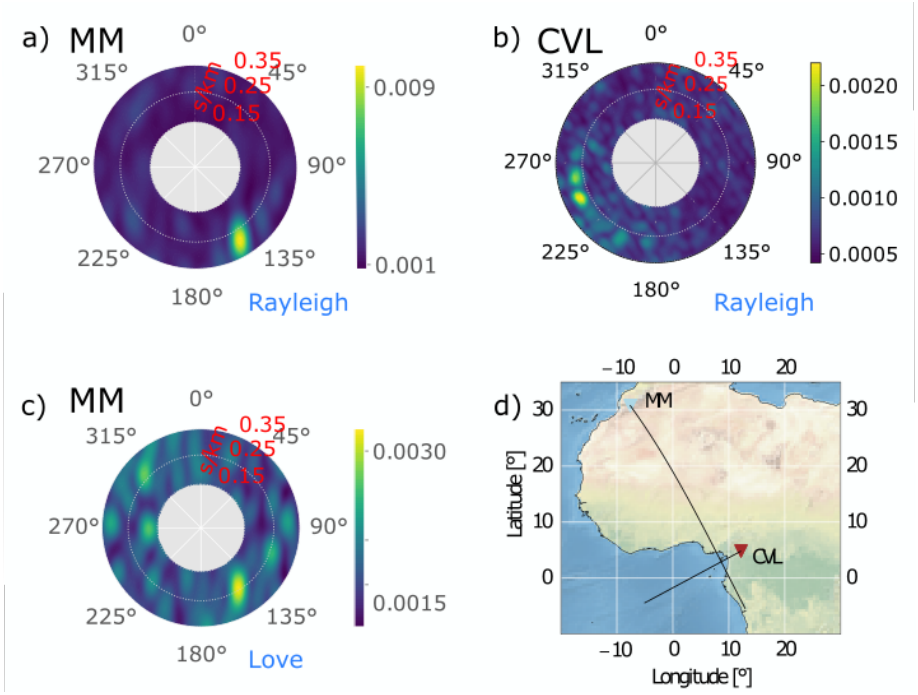

Figure 26: Beamforming results for gliding tremor Beampower as a function of back azimuth and slowness for Rayleigh waves on a) the Morocco array (MM) and b) the Cameroon array (CVL). The results are consistent for all glides detected on the MM array from a glide **date**. The results for the CVL array is stacked for 3 glides from May 2006. c) Love waves coming from the same direction are also detected on the MM all glide events. The results are calculated for frequency equal to 0.048 Hz for the Morocco array and 0.05 Hz for the Cameroon array.

primary microseism is when the water depth (h) is smaller than half of the deepwater wavelength (L_∞), approximated by $L_\infty = \frac{gT^2}{2\pi}$, and for 26 s waves, $L_\infty \sim$ 1000 m [Bromirski and Duennebier, 2002]. The ocean waves begin to interact with the seafloor when the water depth is less than half the deepwater wavelength, which in this case would be 500 m. Most primary generation probably occurs at water depths less that $L_\infty/4$ [Bromirski and Duennebier, 2002]. The depth where we locate the source is deeper than 500 m.

The optimal depth for secondary microseism excitation depends on the frequency of the microseismic noise [Longuet-Higgins, 1950], but in general, the optimal ocean depth is larger for lower frequencies. Tanimoto [2013] calculated that the ocean depth where 0.05 Hz secondary microseisms is most efficiently excited is 7.7 km, which is already deeper than the ocean depth in the Gulf of Guinea. The optimal

depth for 0.038 Hz must be even larger.

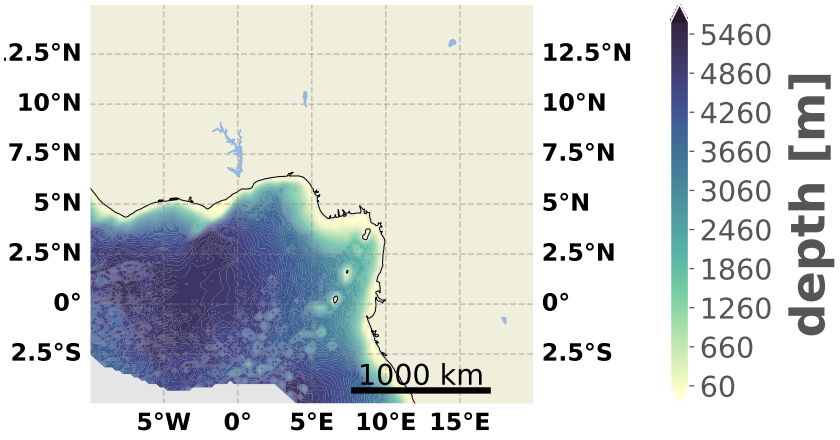

Figure 27: Bathymetry for the Gulf of Guinea.

Some authors report seasonal variation of the amplitude of the 26 s microseism [Holcomb, 1998, Shapiro et al., 2006], with the amplitudes maximizing in the southern hemisphere winter, pointing towards oceanic origin of the signal. Since the source is located close to the equator, we would expect a semi-annual pattern, with an increase in burst detections both for (norther hemispheric) summer and winter months, which is not represented in the data.

Linear gliding features in seismic spectrograms can be observed as a result of remote storms over the oceans. These storms generate ocean gravity waves, typically with periods ranging from 3 to 20 seconds [Bromirski and Duennebier, 2002]. When the dispersed ocean waves arrive at the coast, the low-frequency waves reach the shore first, followed by increasingly higher frequency waves [Haubrich et al., 1963]. As the swell couples into the seafloor and generate seismic waves, it produces a characteristic fan-like shape in seismic spectrograms, broadening towards higher frequencies, with a duration up to a few days [Chevrot et al., 2007]. The slope of the resulting shape gives an estimate of the distance to the

storm [Bromirski and Duennebier, 2002]. Applying this to our glide on May 13th, we estimate a distance over 11200 km between storm and coast, which would place the storm in the south Pacific, south of the typical hurricane track latitudes [Knapp et al., 2010a]. The strong repeatability in our glide slopes would imply repeated storms at the same distance, if they were all to be explained by storm-generated seismic waves. We stack the beamforming results for 4 glides detected on the Morocco array, starting 10 days before the start of the glide. The resulting beampower and backazimuth for frequency and time is shown in Figure 28. To emphasize the areas where most detectable signal is present, we placed a transparency mask over the backazimuth-frequency plot, with full transparency for the highest beampowers and less transparency for the lowest beampowers. There is no coherent energy from the same direction before the glides on stacked beamforming results.

Moreover, as the frequency of the ocean waves generated by a storm is determined by the wind speed [Pierson Jr and Moskowitz, 1964], intense storms with sustained wind speeds exceeding 20 m/s would be necessary to explain the low-frequency onset of our glides [Bromirski and Duennebier, 2002]. A comparison to meteorological data [Knapp et al., 2010a,b, Landsea and Franklin, 2013] does not show any correlation in storm occurrence and glide dates, even if global hurricane databases are considered without restricting the occurrence to the South Pacific. We conclude that an oceanic origin for the 26 s microseism and frequency glides in the Gulf of Guinea is unlikely.

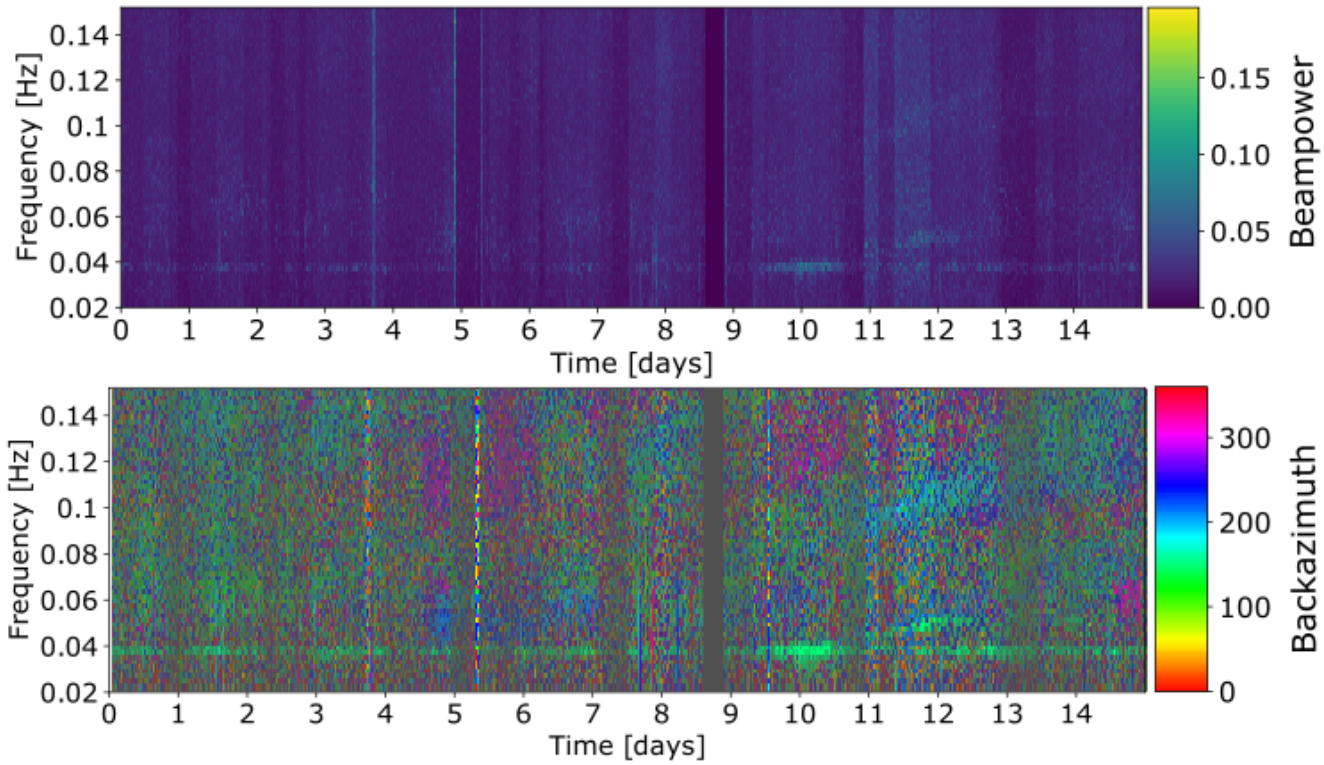

Figure 28: Beampower and backazimuth in frequency and time for stacked beamforming results for 4 glides detected on the Morocco array (2011-2012), starting 10 days before the start of the glide. To emphasize the areas where most detectable signal is present, we placed a transparency mask over the backazimuth-frequency plot, with full transparency for the highest beampowers and less transparency for the lowest beampowers.

4.5.2 Volcanic tremor mechanisms

A non-oceanic candidate to produce monochromatic sustained seismic signals is volcanic processes. The main arguments against volcanic origin of the 26 s microseism is: 1) volcanic tremor is usually at higher frequencies (1-5 Hz) and 2) shorter duration (minutes) and 3) it usually only recorded close to the source McNutt [1992]. Still, there are observations of volcanic tremor that is very long period and long lasting [Dawson et al., 2010, Kawano et al., 2020], and observed far away from the source [Kawakatsu et al., 2000, Yamamoto et al., 1999, Cesca et al., 2020]. As possible tremor generating processes, we consider resonating fluid-filled magma pathways, regular repeated sources and overpressure driven by gas accumulation.

Resonating fluid-filled magma pathways

Firstly, resonating fluid-filled magma pathways can produce harmonic tremor [Schlindwein et al., 1995, Kawakatsu et al., 2000]. We consider a simple organ pipe resonator, the fundamental frequency (f_0) given by: $f_0 = c/2L$, where c is the acoustic velocity in the resonating medium, and L is the length of the crack or conduit [Hagerty et al., 2000]. Given the very low frequency of the 26 s tremor, such a model would require unrealistic velocities or physical dimensions, as extremely large conduit lengths. For example, in order to obtain a fundamental frequency of 0.038 Hz, using a standard velocity of 900 m/s (after Hagerty et al. [2000]) would give a length of 11.8 km. A fluid-filled crack generates a very slow wave that propagates along the crack wall Chouet [1986], known as 'crack waves'. Even when using such slow 'crack waves', assuming a crack wave velocity of 500 m/s, the approximate resonator size needed to generate a tremor at 0.038 Hz is 6.6 km. A way to lower the wave velocities, and hence the length of the resonator, is to replace the magmatic fluids with water. Hydrothermal systems can produce tremor-like signals [Kawakatsu et al., 2000, Ohminato, 2006, Nayak et al., 2020]. A very long period hydrothermal tremor at $\pm$15 s period is detected continuously at Aso generated by inflation and deflation of a shallow water filled crack . This crack has a length of about 1 km, showing that long period tremor can be realized for a relatively small hydrothermal system. However, this tremor has a duration of less than a minute, which is a lot shorter than the 26 s signal. [Kawakatsu et al., 2000, Yamamoto et al., 1999]. Boiling groundwater generates seismic energy through bubble growth and collapse, which typically produces a broadband tremor. If the boiling is contained in a conduit, this process can excite the conduit into resonance and hence produce harmonic tremor [Leet, 1988]. The length of the conduit needed to excite a given frequency is given by the same equation as for a magma filled resonator, above, where c now is the sound velocity in groundwater. Using a velocity of 50 m/s, the lowest velocity considered by Leet [1988], would give a conduit length of around 650 m, which is the minimum size needed for such a system to excite a fundamental frequency of 0.038 Hz. However, this requires a shallow system (source depth less than a few kilometers) to allow the vapor to separate from the fluid [Leet, 1988]. Seeing as the source location for our 26 s microseism and glides are beneath a $>$3 km layer of water, the pressure conditions for such a hydrothermal system would not be ideal.

Regular repeated sources

A repeated source, spaced regularly in time, such as earthquakes or repetitive pressure transients, are

also known to produce a harmonic-like tremor [Hotovec et al., 2013, Lesage et al., 2006, Lees et al., 2004]. To fit our observations, we need repeated pulses with a lag time between the pulses equal to the inverse of the frequency. However, to produce harmonic tremor, we need stable lag times. The long duration of the stable 26 s tremor suggests that repeating events without a stabilizing mechanism is unlikely.

Physical mechanisms for gliding tremor

The bursts of the 26 s source are clearly correlated with gliding tremor. We show that both signals likely originate in the same location in the Gulf of Guinea, and are composed of the same wave types, further supporting the connection between the seismic sources. Frequency gliding is documented at volcanoes worldwide such as Arenal [Hagerty et al., 2000], Semeru [Schlindwein et al., 1995], Redoubt [Hotovec et al., 2013], Lascar [Hellweg, 2000] and Montserrat [Neuberg, 2000]. More specifically, upwards gliding has previously been observed leading up to explosions at volcanoes as Arenal [Lesage et al., 2006], Soufriere Hills [Powell and Neuberg, 2003] and Redoubt [Hotovec et al., 2013]. The changes in frequency of volcanic tremor are believed to reflect changes in source properties. Determining a specific source model for the gliding tremor in the gulf of Guinea, influences how we decode the changes in frequency over time.

Due to the large dimensions need for a fluid filled resonator, the huge geometric changes necessary to explain the glides, and the strong repeatability of this process over decades, the frequency glides are not likely due to changes in resonator length alone. Changes in the fluid properties, essentially changing the velocity, can also change the frequency of the tremor. Small changes in gas fraction can produce large velocity changes [Lesage et al., 2006], and hence changes in the resonator frequency, which are easily reversible and can therefore accommodate the observed repeatability of the glides. For example, new material being injected into the conduit can produce repeated narrow band gliding tremor with roughly linear increase in frequency, which is observed at underwater volcanoes prior to eruptions [Searcy, 2013] The injected material increases the gas content, which in turn decreases as gas is released from the vent, thus changing the wave velocity in the magma [Searcy, 2013, Dziak and Fox, 2002]. However, gliding observed tremor attributed to such changes in gas fraction typically has a short duration of minutes. Such a mechanism can explain a short tremor sequence leading up to an eruption, but to explain the glides in the Gulf of Guinea, we would need a constant flow, with injection and expulsion of material in a repeatable manner over the course of decades.

For a regular repeated source, a change in frequency of the tremor will be produced by changing the trigger frequency, the lag time between the pulses. As the pulses move closer together, the harmonic tremor glides to higher frequencies. When the pulse spacing drifts further apart, the tremor glides to lower frequencies. To fit our observations, the trigger frequency needs to gradually change from 0.038 Hz to 0.05 Hz, with a lag time between the pulses equal to the inverse of the frequency. To produce harmonics, we need stable lag times [Lesage et al., 2006]. This could be difficult to achieve simultaneously as changing the frequency of the pulses. The glides are also extremely repeatable, which would be hard to produce without some mechanism controlling the frequency.

Overpressure driven by gas accumulation

We require a physical system that can reset quickly in a repeatable manner. Gas accumulating under a solid cap can explain repeatable, upward glides in a submarine volcanic setting. The pressure in the conduit builds up, until it overcomes the strength of the cap, producing a pressure pulse resulting seismic signal as the volcanic fluids are released. After the gas is released, another cap starts to form. The signal stops as the top of the magma column has solidified, and the process repeats [Tepp and Dziak, 2021, Chadwick Jr et al., 2008]. Still, this would require a constant availability of material to form a new cap to produce repeatable glides. This situation will unlikely remain constant over decades. Gases escaping slowly from a reservoir closed off by a fractured plug can cause a cycle of pressure drop and bubble formation[Hellweg, 2000]. In this "soda bottle" scenario, the changing frequency would be governed by small, easily reversible changes in flow velocity, instead of changes in the geometry of the conduit, thus enabling repeatability of the glides. For the gliding to continue for decades, it would require a large supply of gas. This is possible if it originates from a large magma reservoir.

Combined source mechanism

The case of stable and varying frequency peaks existing simultaneously have previously been observed at Kilauea, where a continuous stable peak at 0.04 Hz, close to the frequency of our signal, was explained as the breathing mode of the volcanic system caused by synchronous inflation-deflation of cracks and a variable higher frequency peak was interpreted as higher modes of resonance of the system Dawson et al. [2010]. Similarly, this continuous, stable peak at 26 s that we observe coming from the Gulf of Guinea could be a result of a large, magmatic or hydrothermal system, such as a reservoir, continuously

degassing, exciting the system into resonance, while the frequency glides could be related to the gas escaping through a narrow conduit.

The spectral similarity of the simultaneous continuous tremor and glides, suggests the presence of a feedback mechanism between the two systems. A feedback mechanism has previously been used to explain harmonic tremor at Arenal [Lesage et al., 2006] .Lesage et al. [2006] proposed a model for harmonic tremor consisting of gases/fluids escaping from a conduit closed of by a fractured plug, producing repetitive pressure pulses, with a repeat period that stabilizes through feedback with the resonance of the conduit. This "clarinet model" could explain why the frequency gliding starts at the same frequency as the the 26 s microseism, with the source of the glide possibly being connected to or controlled by the 26 s source. We propose a combined source mechanism for the frequency gliding and the 26 s microseism, of a system composed of a fluid-filled conduit, with a natural period of 26 s, and a valve mechanism controlled by feedback with the resonance of the conduit. This indicates a phenomenon that occurs on a massive spatial scale.

Although the 26 s source and the glides cannot be explained by oceanic mechanisms, they are not sufficiently explained by known volcanic mechanisms either, due to the extremely low frequency range, the decades-long timescales where these phenomena seems to have been active and the strong repeatability of the gliding tremor. To confirm if there is actually a massive underwater volcanic system hidden from view in the Gulf of Guinea, we need more data from for example hydrophones, ocean bottom seismometers, buoys, etc in the actual source region. Offshore observations of this system is challenging, due to piracy and local resources. Regardless, this new phenomenon points towards a more complex source for the 26 s microseism than previously thought and further adds on to the mystery of the 26 s microseism.

Location	Frequency/Duration	Gliding/Overtones	Description	Mechanism
Mt. Semeru, Indonesia [Schlindwein et al., 1995]	1 Hz/seconds	Yes/Yes	Continuous tremor gliding up and down	Oscillations of a gas-filled vertical dike
Karymsky, Kamchatka, Russia [Lees et al., 2004]	1 Hz/Seconds	Yes/Yes	Continuous tremor gliding up and down preceeded by an initial explosion	Chugging: gas is released through a time-varying narrowing vent in a series of oscillations. Upward gliding caused by closing of cracks.
Lascar, Chile [Hellweg, 2000]	0.63 Hz/18 hours	Yes/Yes	Continuous tremor going up and down	Fluid-filled resonator/soda bottle/slug flow/eddy shedding
Kilauea, Hawaii [Dawson et al., 2010]	0.04, 0.4 Hz/months	Yes/No	Continuous tremors, both stable and variable peaks going both up and down	Stable peak at 0.04 Hz (breathing mode): synchronous inflation-deflation of the cracks. Variable peak around 0.4 Hz: change in the resonant characteristics of a fluid-filled crack (aperture/pressure)
Ambrym, Vanuatu [Kawano et al., 2020]	0.04 Hz/Months	Yes/No	Continuous tremor going up and down.	Unknown
26 s microseism, Gulf of Guinea	0.038 Hz/50 + years	No/No	Continuous tremor without changes in frequency, variable amplitude, observed globally	Unknown

Table 2: Tremor characteristics from volcanic and hydrothermal systems described throughout the literature

Table 3: Tremor characteristics from volcanic and hydrothermal systems described throughout the literature

Location	Frequency/Duration	Gliding/Overtones	Description	Mechanism
Redoubt, Alaska [Hotovec et al., 2013]	1-30 Hz/Minutes to hours	Yes/Yes	Repeatable upward gliding leading up tp explosion	Superposition of increasingly frequent and regular stick-slip earthquakes
Arenal, Costa Rica [Lesage et al., 2006]	1 Hz/Seconds	Yes/Yes	Several different gliding signals, both going up and down. Upward gliding often observed after explosions.	Intermittent gas flow through a fractured plug closing off a conduit filled with bubbly magma and repetition stabilized by the resonance of the conduit
South Sarigan Seamount, Mariana Islands [Searcy, 2013]	6-10 Hz/Minutes	Yes/Occasionally	Saw-tooth sequences, gradually gliding up and then abruptly falling back	Changes in magma velocity due to changes in gas content as new gas rich material is injected into the conduit and gas is released from the vent
Volcano Islands arc, Japan [Dziak and Fox, 2002]	10 Hz/Minutes	Yes/Yes	Tremor gradually gliding up and then abruptly falling back	Changes in magma velocity due to changes in gas content as new gas rich material is injected into the conduit and gas is released from the vent
Mayotte [Cesca et al., 2020]	0.06 Hz/minutes	No/-	Detected globally	Resonance caused by slow standing waves trapped at the fluid–solid interface of a fluid-filled crack or conduit

5 Discussion

Based on our observations, the physical mechanism generating the frequency glides should fulfill the following criteria: it should be repeatable, implying either reversibility or a recharge mechanism; it should be capable of continuously outputting energy for at least 60 years; it should be energetic enough to be observed globally; it should have a fixed location; and finally, since the glides and monochromatic 26 s microseism are connected in frequency, time and space, the mechanism should be able to generate both stable and varying frequency peaks simultaneously. Based on the observed features, we discuss 4 possible mechanisms for the tremors: 1) oceanic, 2) volcanic, 3) hydrothermal and 4) hydrologic and mud volcanic mechanisms.

5.1 Oceanic mechanisms

For the continuous 26 s signal, we would need ocean waves of 26 s or 52 s for primary and secondary microseism generation respectively. Ocean waves typically have a central period of 15 seconds over open ocean. Higher windspeeds result in longer periods [Pierson Jr and Moskowitz, 1964]. Longer period ocean waves also require a longer fetch, suggesting that a very large open body of water is needed to allow 26 or 52 s surface waves to form.

We consider the optimal depth for 26 s primary microseism generation. The depth where you would expect primary microseism is when the water depth (h) is smaller than half of the deepwater wavelength (L_∞), which 1000 m for 26 s waves [Bromirski and Duennebier, 2002]. The ocean waves begin to interact with the seafloor when the water depth is less than half the deepwater wavelength, which in this case would be 500 m. Most primary generation probably occurs at water depths less that $L_\infty/4$[Bromirski and Duennebier, 2002]. The depth where we locate the source is deeper than 500 m.

In general, the optimal ocean depth for secondary microseism excitation is larger for lower frequencies [Longuet-Higgins, 1950]. Tanimoto [2013] calculated that the ocean depth where 0.05 Hz secondary microseisms is most efficiently excited is 7.7 km, which is already deeper than the ocean depth in the Gulf of Guinea. The optimal depth for 0.038 Hz must be even larger.

Some authors report seasonal variation of the amplitude of the 26 s signal [Holcomb, 1998, Shapiro

et al., 2006], with larger amplitudes in the southern hemisphere winter, pointing towards oceanic origin of the signal. Since the source is located close to the equator, we would expect a semi-annual pattern, with an increase in burst detections both for (norther hemispheric) summer and winter months, which is not represented in the data.

Linear gliding features in seismic spectrograms can be observed as a result of remote storms over the oceans. These storms generate ocean gravity waves, typically with periods ranging from 3 to 20 seconds [Bromirski and Duennebier, 2002]. When the dispersed ocean waves arrive at the coast, the low-frequency waves reach the shore first, followed by increasingly higher frequency waves [Haubrich et al., 1963]. As the swell couples into the seafloor and generate seismic waves, it produces a characteristic fan-like shape in seismic spectrograms, broadening towards higher frequencies, with a duration up to a few days [Chevrot et al., 2007]. The slope of the resulting shape gives an estimate of the distance to the storm [Bromirski and Duennebier, 2002]. Applying this to our glide on May 13th, we estimate a distance over 11200 km between storm and coast, which would place the storm in the south Pacific, south of the typical hurricane track latitudes [Knapp et al., 2010a]. The strong repeatability in our glide slopes would imply repeated storms at the same distance, if they were all to be explained by storm-generated seismic waves. For this we would need coherent energy from the same direction before the glides, which we do not see. Moreover, as the frequency of the ocean waves generated by a storm is determined by the wind speed [Pierson Jr and Moskowitz, 1964], intense storms with sustained wind speeds exceeding 20 m/s would be necessary to explain the low-frequency onset of our glides [Bromirski and Duennebier, 2002]. A comparison to meteorological data [Knapp et al., 2010a,b, Landsea and Franklin, 2013] does not show any correlation in storm occurrence and glide dates, even if global hurricane databases are considered without restricting the occurrence to the South Pacific. We conclude that an oceanic origin for the 26 s microseism and frequency glides in the Gulf of Guinea is unlikely.

5.2 Volcanic mechanisms

Mostly, very long period signals are recorded in volcanic areas, suggesting magmatic origin. The main arguments against volcanic origin of the 26 s microseism is: 1) volcanic tremor is usually at higher frequencies (1-5 Hz) and 2) shorter duration (minutes) and 3) it usually only recorded close to the source [McNutt, 1992]. Still, there are observations of volcanic tremor that is very long period and long lasting

[Dawson et al., 2010, Kawano et al., 2020], and observed far away from the source [Kawakatsu et al., 2000, Yamamoto et al., 1999, Cesca et al., 2020] (see Table 2 and 3 for overview of tremor observations). From our observations and previous studies, the 26 s microseism has stable properties in terms of frequency, amplitude and location for decades, and is connected to a repeatable gliding tremor apparently originating in the same source area. This suggests that we need a stable part of the system, generating the 26 s signal, and another part of the system that can be excited again and again at the same frequency.

Recently, long duration ($\sim$ 20 minutes), very long-period monochromatic signals ($\sim$ 16 s) were observed globally originating near Mayotte volcano and interpreted as resonance of a large crack-like intrusion with a dimension of several kilometers [Cesca et al., 2020]. If we consider a simple organ pipe resonator as the 26 s source, the fundamental frequency (f_0) is given by: $f_0 = c/2L$, where c is the acoustic velocity in the resonating medium, and L is the length of the crack or conduit [Hagerty et al., 2000]. In order to obtain a fundamental frequency of 0.038 Hz, using a standard velocity of 900 m/s (after Hagerty et al. [2000]) would give a length of about 12 km. This is about the same length as assumed for Mayotte. At Mayotte the reservoir is drained, causing the overlying rock to to fail, which triggers the reservoir into resonance [Cesca et al., 2020]. Since the 26 s microseism has been stable for decades, it is more likely that an internal mechanism, such as degassing or groundwater boiling could trigger the system into resonance. Although different from what we have, shorter duration and higher frequency, it gives an estimate for the size that could be expected for the 26 s source, and what volcanic process could produce long period, long duration, globally observable volcanic tremor.

The dominant period of the very long period signals at Mayotte changes gradually from $\sim$ 15.2 s to $\sim$ 15.6 s and down again to $\sim 15.3s$, which is explained by thinning and shortening of the crack. The changes in fundamental frequency of the glides that we observe would require a large geometric change, which would not be able to quickly reset, as we need for our repeated glides. In the case of Mayotte, the frequency goes both up and down. If the length of the resonator increases and then decreases, we would expect the frequencies to glide both up and down. In the gulf of Guinea, we only have upward glides. Hence, the changes in frequency of the glide is likely not related to geometric changes alone.

Changes in the fluid properties, essentially changing the velocity, can also change the frequency of the tremor. Small changes in gas fraction can produce large velocity changes [Lesage et al., 2006], and

hence changes in the resonator frequency, which are easily reversible and can therefore accommodate the observed repeatability of the glides. For example, new material being injected into the conduit can produce repeated narrow band gliding tremor with roughly linear increase in frequency, which is observed at underwater volcanoes prior to eruptions [Searcy, 2013]. The injected material increases the gas content, which in turn decreases as gas is released from the vent, thus changing the wave velocity in the magma [Searcy, 2013, Dziak and Fox, 2002]. However, gliding observed tremor attributed to such changes in gas fraction typically has a short duration of minutes. Such a mechanism can explain a short tremor sequence leading up to an eruption, but to explain the glides in the Gulf of Guinea, we would need a constant flow, with injection and expulsion of material in a repeatable manner over the course of decades.

The case of stable and varying frequency peaks existing simultaneously have previously been observed at Kilauea, where a continuous stable peak at 0.04 Hz, close to the frequency of our signal, was explained as the breathing mode of the volcanic system caused by synchronous inflation-deflation of cracks and a variable higher frequency peak was interpreted as higher modes of resonance of the system Dawson et al. [2010]. Similarly, this continuous, stable peak at 26 s that we observe coming from the Gulf of Guinea could be a result of a large, magmatic system, such as a reservoir, continuously degassing, exciting the system into resonance, while the frequency glides could be related to the gas building up and escaping through a narrow conduit. Then, the glide should have a higher fundamental frequency than the 26 s signal, since it represents the resonance of a smaller part.

How do we explain that the tremors start at the same frequency? Lesage et al. [2006] proposed a model for harmonic tremor consisting of gases/fluids escaping from a conduit closed of by a fractured plug, producing repetitive pressure pulses, with a repeat period that stabilizes through feedback with the resonance of the conduit. This clarinet model could explain why the frequency gliding starts at the same frequency as the the 26 s microseism, with the source of the glide possibly being connected to or controlled by the 26 s source.

A magmatic system consisting of a conduit, can be triggered into resonance by an internal mechanism, such as gas release. The conduit is sealed off by a fractured plug that acts as valve through which gas can escape intermittently, thereby producing pressure pulses with a repetition period stabilized by the resonance of the conduit. However, due to the long period of the signal, this would lead to a very

large system when using standard values for fluid velocities, such as 2 km/s for volcanic melt [Kawakatsu et al., 2000]. Chouet [1988] showed that waves trapped in a fluid-filled crack can travel more slowly than the sound velocity in the fluid, which he called 'crack waves'. Such crack waves may explain the long period nature of the 26 s signal. Another way of lowering the wave velocity in the fluid is to replace the volcanic melt (2 km/s) with water (1.2 km/s) or vapor (300 m/s).

5.3 Hydrothermal mechanisms

Long period tremor have persistently been reported from Aso volcano in Japan, since it was discovered in the 1930's [Sassa, 1935, Kaneshima et al., 1996, Yamamoto et al., 1999, Niu and Song, 2020]. Kawakatsu et al. [2000] found that regardless of surface activity, long period tremor around 15 s with a short duration of less than 1 minute is excited continuously from 1-1.5 km below the crater. This long period tremor was explained by the inflation and deflation of a hydrothermal system consisting of an aquifer and a crack or fractures filled with water and fragmented rocks. In this case, heat is transferred upwards from a deep magma chamber. The source region buffers the heat transport, and leaks gas or water upwards to a crater lake. When the heat injection from below increases and stays high for a while, or the bottom of the crater lake is shut off by mud sedimentation, pressure increases in the source region, inflating the crack and the aquifer. When the pressure gets too high, gas and mud is released, resulting in explosive eruptions. Yamamoto et al. [1999] detected the crack like conduit beneath the active crater, which has the dimension of 1 km. Changing the previously proposed system into a hydrothermal system consisting of a layered structure or channel, set into resonance by groundwater boiling, would lower the length needed for the resonator [Leet, 1988]. The bulk sound velocity for a water-steam mixture can be as low as ~ 20 m/s, according to Kieffer [1984]. Due to the large dimensions of the magmatic conduit (and that it is not correlated with known volcanic eruptions), a hydrothermal system could be more likely.

5.4 Hydrologic mechanisms and mud volcanoes

Very long period tremor is also observed in volcanically inactive regions. For example, there is mud volcanic activity in the gulf [Graue, 2000]. Mud volcanoes can produce harmonic tremor [Franek et al., 2014]. However, such processes are usually only detected a couple of kilometers from the source.

Nishida and Shiomi [2012] discovered very long period (0.085 Hz) monochromatic tremors beneath the Shonai Plain in Japan. The tremor lasted for several days, and the tremor activity also occurred several times per month during the winter. This tremor was attributed to a subhorizontal crack coupled with a fluid reservoir, triggered by secondary microseism. The observation is similar to the 26 s microseism observed in the Gulf of Guinea, but much weaker.

Similarly, Chen et al. [2022] proposed that the 26 s signal is a result of resonance of a fluid-filled conduit, where the fluids are associated with the thick sediments from the Niger delta, modulated by the primary microseism and occasionally ocean swell. Chen et al. [2022] suggested that dispersive signals accompanying bursts in the 26 s source were ocean swells passing by the 26 s source, triggering the 26 s signal. If this was the explanation for the simultaneous excitation of the gliding tremor and the 26 s microseism, we would still need large storms at the same distance from the Gulf of Guinea to explain the low frequency onset and repeatability, which is not the case 3.4.1. In any case, such hydrologic processes are unlikely to be energetic enough to produce the signals that we observe almost globally.

6 Conclusion

We study the location, wavetypes radiated and evolution of the 26 s microseism, and find out that the source has stable properties over the time scales investigated. We discover that energy bursts in the 26 s signal are often accompanied by a spectral glide effect. This points towards a more complex source mechanism for the 26 s source than previously imagined. Our discovery of the glides helps put constraints on possible source mechanisms for the 26 s signal, and provides a reference for comparison with other geophysical data.

We show oceanic origin of the phenomena is unlikely, as there are large storm associated with the occurrence of the gliding tremor. Our research points towards a massive magmatic or hydrothermal underwater system in the Gulf of Guinea. Our suggested model is a hydrothermal system, consisting of a layered structure or channel, sealed off by a fractured plug that acts as valve with a repetition period stabilized by the resonance of the channel.

There is still no physical model that can fully explain the glides in terms of repeatability, strength, linear change in frequency, and duration of the glides, nor can we explain how energy can be released in such a stable manner for decades. Moreover, no existing model can adequately explain both the glides and the 26 s signal simultaneously. Still, the nature of the Gulf of Guinea tremors forces us to broaden our thinking about gliding tremor and about the mysterious signals the Earth produces.

7 Outlook

To confirm if there is actually a massive underwater volcanic system hidden from view in the Gulf of Guinea, we need more data, especially from the actual source region from for example hydrophones, ocean bottom seismometers, buoys, etc in the actual source region. Offshore observations of this system is challenging, due to piracy and local resources.

7.1 More precise source location and imaging

Where the sources are located, play a large part in how their physical mechanism is interpreted. For example, the 27 s and 16 s source are often suggested to be generated by volcanic mechanisms, because they are located close to the Cameroon line. As this is not the case for the 26 s source, it is typically not attributed to volcanic activity, but to oceanic mechanisms. Therefore it is important to get more precise source locations.

In this work we use data from three seismic arrays in Africa. Additional seismic arrays can help improve the locations of the persistent localized sources in the gulf. Since the 26 s microseism and glides are occasionally so strong they can be detected almost globally (Figure 29), this opens for using arrays also on other continents.

Ocean bottom sensors and DAS can provide a better data coverage in the gulf. Sensors that are closer to the actual source location, can improve the detection of the seismic signals and be used to get a more precise source location. Sensors in the gulf can also be used to image the subsurface, which can give valuable information about the resonating structure, as physical dimensions and depth, if there is one. Observations from seismic studies can help identify deformation and subsurface features that are related to degassing, such as mudvolcanoes, pockmarks, fluid-fault-hydrate systems, which could also help localizing the source.

Different methods for source location can be used. Previously, Shapiro et al. [2006] used seismic interferometry to localize the source. Chen et al. [2022] used polarization analysis. In this work we used 3-component beamforming. We also compared the source location for the 26 and 27 source using beamforming and matched field processing. Here, preliminary results are presented.

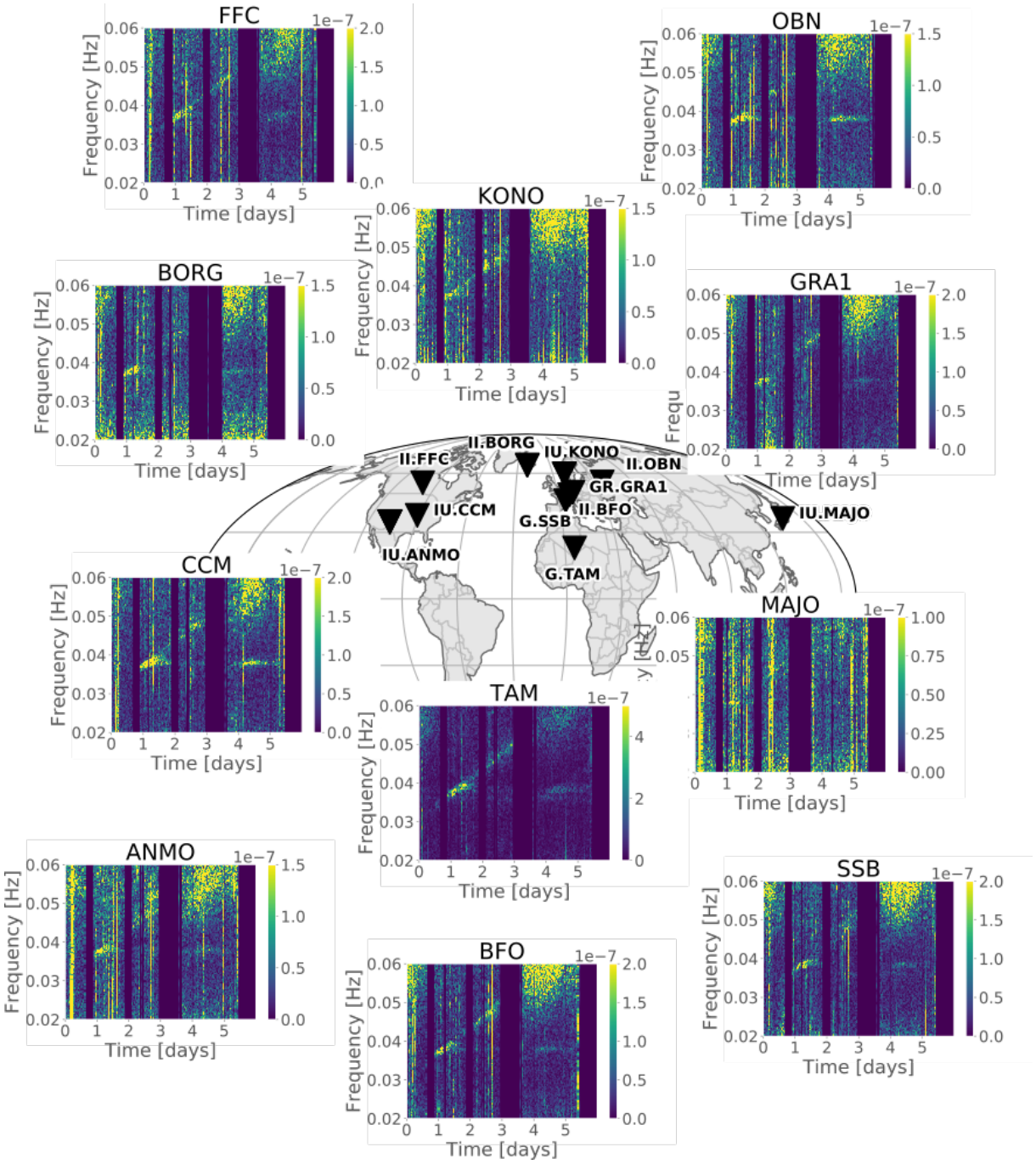

Figure 29: cool or messy? Glide on 2013-04-11 detected on stations nearly globally.

7.1.1 Source locations from beamforming vs matched field processing

First we compare the source location of the 26 s and 27 s source from 3-component beamforming using the Cameroon array data from May 2006. The results are calculated for 10 day intervals and for frequency, $f = 0.038 \pm 0.001$Hz and $f = 0.036 \pm 0.001$Hz to separate between the two narrow band sources. Figure 30 shows the beamforming output for the 26 s and the 27 s source for the entire month of May 2006. For each stacked 10-day beamformer output, the slowness and backazimuth corresponding to the maximum beamformer power is selected, which is presented in Table 4. Our beamforming results yield slightly different results for the 26 s and 27 s signal for the data from the Cameroon array, with backazimuths of about 252 degrees and about 250 degrees, respectively. We get slownesses of 0.26-0.27, which is the same for both sources.

Table 4: Beamforming results for 26 vs 27 s tremor from Cameroon data

Frequency	Date	backazimuth	Slowness	Maximum beampower
0,038	2006-05-01	252	0.27	0.00048
	2006-05-11	254	0.27	0.00062
	2006-05-21	250	0.26	0.00037
0.036	2006-05-01	250	0.27	0.00035
	2006-05-11	250	0.27	0.00046
	2006-05-21	248	0.26	0.00037

Since the Cameroon array is relatively close to the source area, we also investigate the location of the two tremors using matched field processing. Matched field processing is a generalization of beamforming, which allows for curved wavefronts [Baggeroer et al., 1993] . The results are calculated for frequencies, $f = 0.038 \pm 0.005$ Hz ang $f = 0.036 \pm 0.005$ Hz. In order to compute the synthetic wavefield, we use simple analytical Green's function and assume a constant velocity $v = 3.7$ km/s. This velocity is obtained from the plane wave beamforming. For the 26 s source, we get a source location at 7.47E, 2.85N. For the 27 s source we get the location at 7.57E, 3.66N. The locations are calculated for the

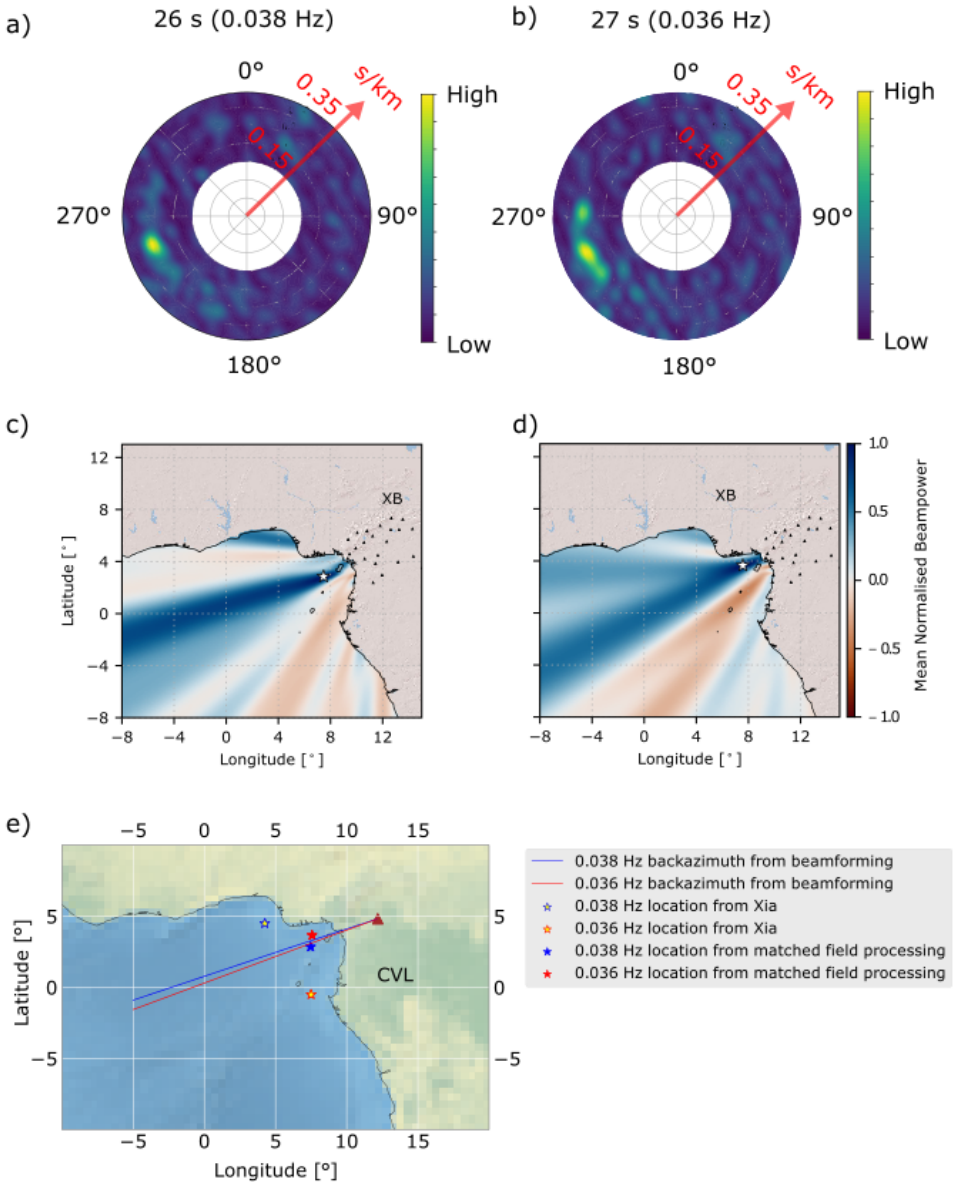

Figure 30: Source location of the 26 s and 27 s source from three component beamforming. a) and b) show beamforming results for the 26 and 27 s source respectively. Results for the 26 s and 27 s signal from matched field processing is displayed in c) and d). In d) we compare the source locations from the different methods to the results from Xia and Chen [2020].

approximately the whole year of 2006.

The locations are pretty consistent for both methods, but slightly off from the backazimuth from three component beamforming for the same array. The difference could suggest that the plane wave assumptions is violated, but due to the large uncertainties of the methods, the differences are not significant enough to draw a clear conclusion. We locate both sources close to each other and the Cameroon line. Comparing our results with source locations from previous studies, our resolved source location for the 26 s source is closer to the Cameroon volcanic line, and the two sources close together.

7.2 Ocean wave state in the gulf

From buoy data we can get information about wave period, waveheight and directional wave spectra. Buoy data from the gulf could be used to see if the glide activity is reflected in the ocean wave state in the gulf. From buoy data we can also see if there is actually 26 or 52 s waves in the gulf, needed to generate 26 s ocean microseisms. Since we do not have buoy data, we use an ocean wave model (WW3) [Tolman et al., 2009, Ardhuin et al., 2014] to estimate the ocean wave activity in the gulf. Here we show the significant waveheight integrated over an area of the gulf (Figure 27) with the spectrogram in Figure 31 for months March, April, May and June. There is no clear correlation between the glides and the significant waveheight in the gulf. Here we are using both wind and swell waves. These results could be improved by isolating the long period ocean waves.

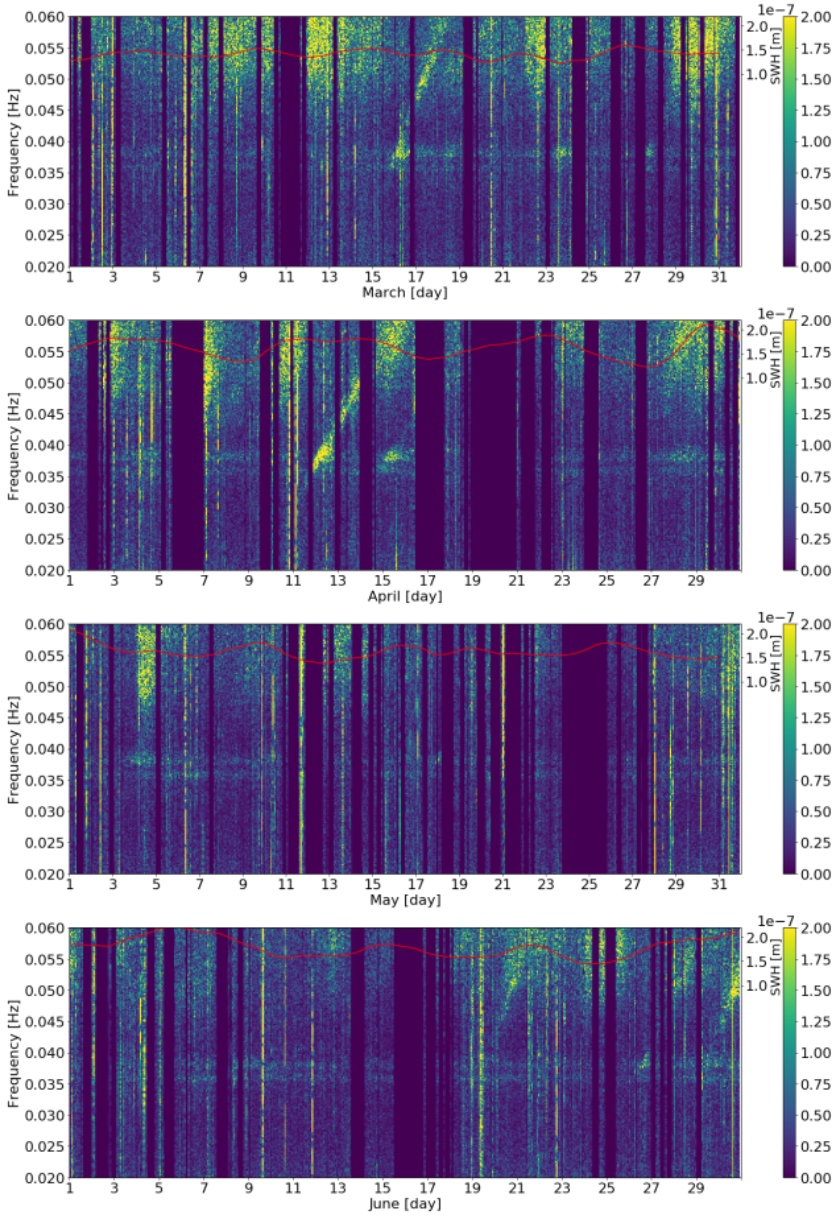

Figure 31: Spectrograms for months March, April, May and June 2013. The red line represents the significant waveheight for wind and swell waves in the gulf from ocean wave model Wavewatch III.

7.3 Hydrophone data

The hydroacoustic signals detected by hydrophones could also be used to identify submarine volcanism. Since seismic waves are attenuated more than hydroacoustic signals, so they cannot propagate as far or

as efficiently as hydroacoustic signals. Volcanic activity is also generally associated with weak seismicity, and is mostly not detectable at longer distances than 100-200 km. Hydroacoustic signals on the other hand, could be detected at far greater distances. This is partly because of the SOFAR channel, and because of the low attenuation of sound in water, which allows the hydroacoustic signals to across and between ocean basins. [Tepp and Dziak, 2021]. There are even observations of submarine eruptions being detected at distances greater than 14,000 km [Dziak and Fox, 2002, Metz et al., 2016, Tepp et al., 2019]. These hydroacoustic waves could either be generated directly, from for example an explosion in a volcanic vent generating both seismic waves travelling in the subsurface and hydroacoustic waves travelling in the water, or through shaking or depth changes of a hydrophone mooring, or through conversion from seismic waves.

What would volcanic signals look like in hydrophone data?

Submarine volcanoes are associated with signals from earthquakes and eruptions, such as explosions, lava extrusions and lava flows. Hydroacoustic signals could also be generated from magmatic fluids moving in the subsurface, referred to as 'non-eruptive' tremor. Short, impulsive explosions typically produce broadband (up to 100 Hz) hydroacoustic signals with short duration (seconds). For example, gas accumulating under a quenched cap produces explosive eruptive signals when the gas is released, called Rotian eruptions. The signals produced by such eruptions are characterized by repetitive broad band pulses of energy that increase in amplitude before abruptly stopping. The pulses have durations of seconds to minutes, either with energy in a broad or narrow frequency band. Gliding inside on pulses and from one pulse to another has been observed. Dziak and Fox [2002] reported upward gliding tremor sequences with multiple overtones on hydrophones in the Pacific, although with shorter duration and higher frequency than the gliding tremor in the Gulf of Guinea. Sequences can last for months to years without a significant pause in activity. Variations in gas flow, size of gas bubbles, magma viscosity, and size of vent, among other parameters, is believed to determine the duration and frequency content of the signals. The signals have only been recorded hydroacoustically, on local and regional distances. It is not clear whether such signals would be detectable on seismic sensors. Very-short-duration impulses (< 1s) have also been recorded by instruments close to the vent (within 2 km) during these eruptions, which have been attributed to gas bubble bursts [Tepp and Dziak, 2021, Chadwick Jr et al., 2008].

At South Sarigan, a narrow band tremor with a linear increase in frequency was observed leading up to

a large explosion. Although at higher frequencies (5-10 Hz) and shorter duration (2 minutes), this is similar to the behavior of our gliding tremor. This is observed on both hydrophones and seismometers [Searcy, 2013, Green et al., 2013]. In cases where such behavior is observed leading up to explosive eruptions, it is typically attributed to pressure build-up in the conduit, but can also be a result of series of earthquakes with an increasing rate merging into a gliding tremor [Tepp et al., 2019, Searcy, 2013, Tepp and Haney, 2019].

Are there hydroacoustic signals accompanying the gliding tremor?

The upward gliding tremors from South Sarigan are both visible on hydroacoustic and seismic sensors. The closest hydrophone is situated in Ascension Island. Unfortunately, this instrument is not sensitive to such low frequencies as the glides, and we are therefore not able to see if the glide signal is visible on hydrophone data.

Gas escaping from the ocean floor combined with bubbles bursting, could have an acoustic signature detectable on hydrophones. To see if there is any hydroacoustic signals accompanying the gliding tremor, we use data from the time of the glides and compare with hydrophone data from station H10N1, Ascension Island. We show the hydroacoustic data for 2 glides on 2015-03-07 and 2016-07-30, shown with the glide on seismic data from TAM. We did not detect anything unusual at the time of the glides. Given that such signals are typically only observed on stations close to the vent, the station is likely too far from the hypothesized source location to detect the high frequency signals from bubbles bursting. We therefore need hydroacoustic data from sensors closer to the source.

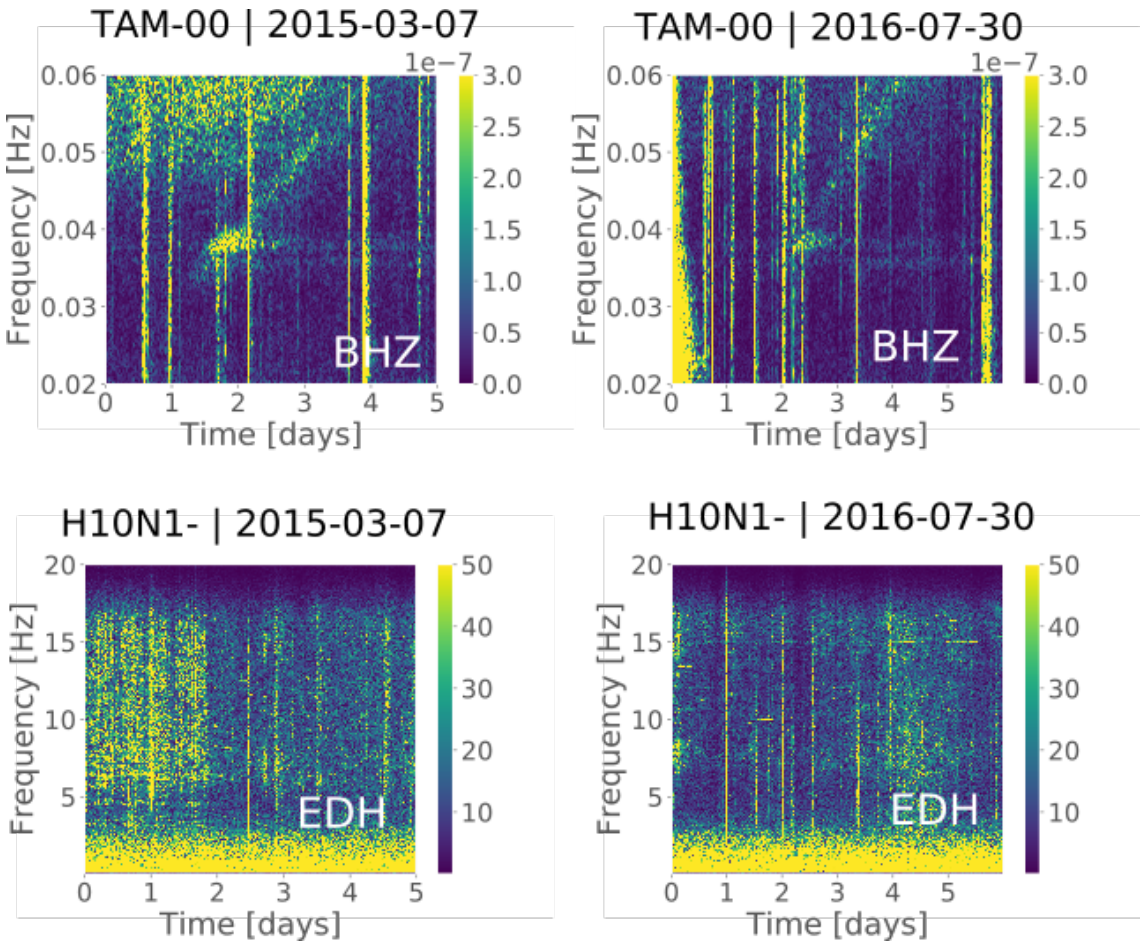

Figure 32: Seismic and hydroacoustic data for two glide events on 2015-03-07 and 2016-07-30 from Z component on TAM and H component of H10N1. The spectrograms are calculated for a window length of 1 hour and 50 percent overlap.

7.4 Satellite data

Because of the lack of data from the research area, an option to study this phenomenon remotely using satellite data. If there is degassing on the sea bottom, this could produce surface manifestations, as disturbances of the sea surface, temperature anomalies and discoloration on the sea surface. To investigate this, we used satellite data (sea surface height from Jason-3, Sentinel-3A, HY-2A, Saral/AltiKa, Cryosat-2, Jason-2, Jason-1, T/P, ENVISAT, GFO, ERS1/2 [CLS (France), 2012] and sea surface temperature from OSTIA SST analysis combining satellite data from the GHRSST project and in-situ observations to determine sea surface temperature [CNR (Italy), 2009]). We searched for evidence of any sea surface

disturbance by rising bubbles at the time of several glides, and did not detect anything. However, this does not exclude that there is actually degassing going on at depth. Seeing as the source location for our 26 s microseism and glides are beneath $a > 3$ km layer of water, we might not be able to see the effects at the sea surface.

7.5 Crack dimensions: Numerical (and theoretical) studies

To get better estimates for the shape and size of resonators that can produce the 26 s signal and the glides, we can use numerical studies. For example models as Julian [1994]'s fluid flow or Chouet [1986, 1988]'s fluid-filled crack could provide approximate dimensions needed for the system, and if such signals could physically be explained by such models. Maeda and Kumagai [2017] found theoretically a generalized equation for the resonance frequencies of a fluid-filled crack, which could also be applied. For such applications, we need to know the resonance frequencies of the system. We have previously shown that the slope of the fundamental gliding peak frequency does not change significantly over the years investigated in this work. The overtone typically exhibits regular harmonic spacing, with the overtone at two times the fundamental. This is previously shown on seismic data from Cameroon 2006. This, however, is not always the case. In the next section we show variations in harmonic spacing and additional harmonics. The observed neighboring peaks is similar to the results from numerical studies of the dynamics of two fluid-filled cracks placed in a series, which produces an inharmonic spectra [Dahm, 1992]. These changes in inharmonic spacing could hold information about how the system evolves over time.

7.5.1 Complexity of the glide signals

Here, we increase the signal to noise ratio by delay and sum of the traces of 15 stations from the Morocco array according to the backazimuth (152 degrees)and velocity (3.7 km/s) obtained from the beamforming results. This is done for all glides detected on the Morocco array from 2011 to 2012. The stacked spectrograms are shown in Figure 33.

For all the glides detected on the Morocco array, the overtone appears to have been shifted upwards. For the glide from 2012-06-08, we check if this shift is consistent on another seismic station (TAM), shown in Figure 34. This is also the case, suggesting that this change is related to changes in the actual source, not propagation effects. The frequency and slope of the fundamental is not changing, the temporal variation is just in the (in)harmonic spacing. Occasionally, two neighboring gliding peaks are observed, which resembles the frequency of the previously described overtones (Figure 34).

This is not an isolated case. Other examples of multiple overtones on station TAM are shown in Figure 35. On one occasion, 2012-07-30, two simultaneous glides around the fundamental frequency were also observed (Figure 35). In some cases, the frequency band appears to widen as the frequency glides into the microseism frequency band. This is especially the case for the overtone, for example the glide on 2012-07-30 in Figure 35 and 33 for TAM and MM array, respectively. In other cases it is very narrow band, as the fundamental (Figure 33 2011-01-06 and 2012-05-16). The temporal variation in (in)harmonic spacing could provide information about how the system is evolving. The inharmonic overtones point towards a more complex system than previously suggested. More sophisticated methods for spectral estimates can help detect possible weaker overtones. It could also help constrain the frequency and duration of the glide, to see when the signal starts and ends, in both time and frequency.

7.5.2 Spectral estimates

We can increase the time-frequency resolution by for example using a Multi-Taper approach. Figure 36 shows the spectrogram for the glide 2012-07-30, spectra are calculated for 2 hour windows, with no overlap using mtspec [Prieto et al., 2009, Krischer, 2016]. There are two distinct gliding spectral lines around the fundamental frequency. We also show an example of a glide using mtspec to produce the Wigner-Ville Distribution of the glide signal using multitaper spectral estimates. The time-frequency representation is shown in Figure 37. The multitapers enhances the glide. We can see a faint double overtone for the glide on May 12th 2006 for a station in the Cameroon array (CM09). For future work,

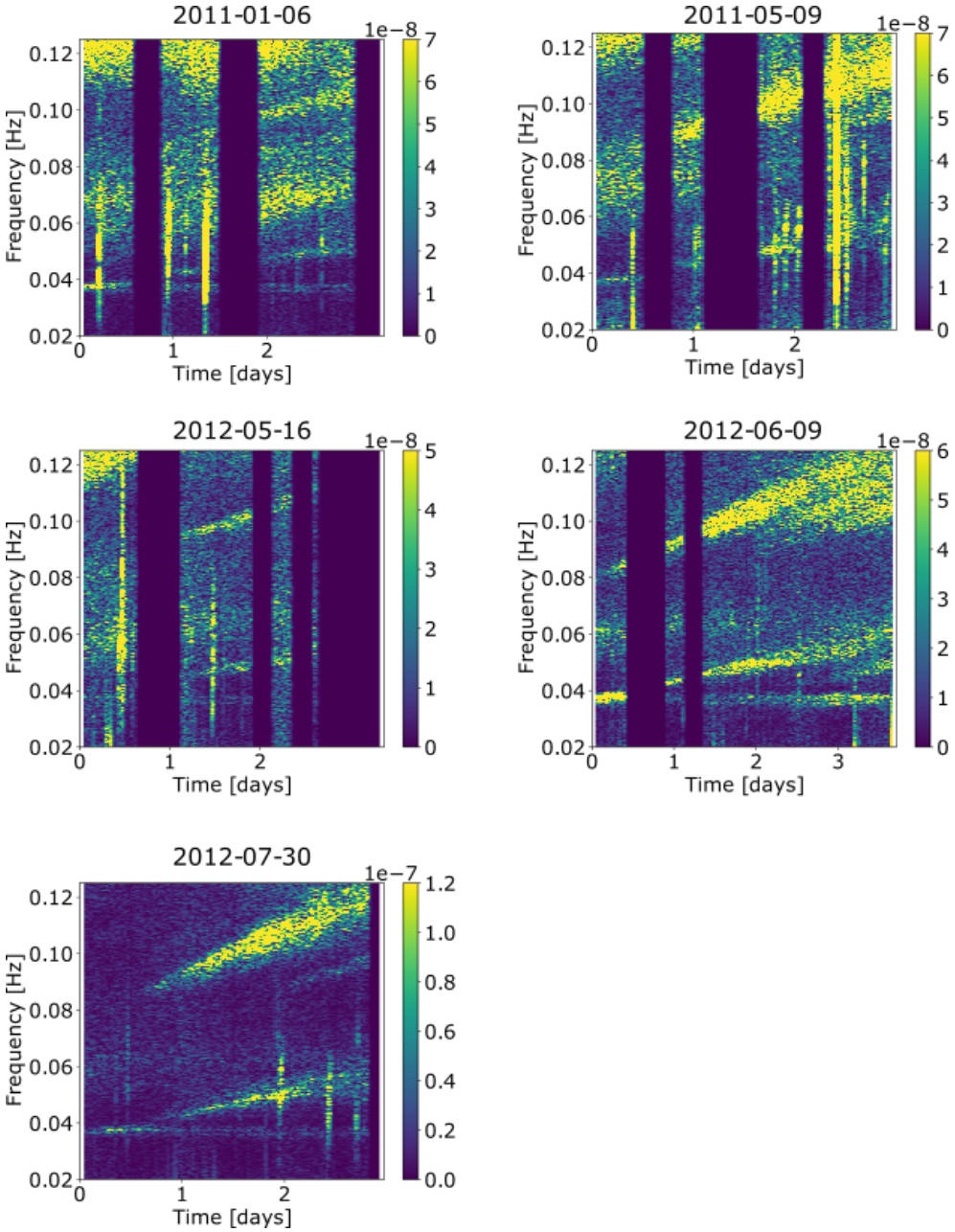

Figure 33: Spectrogram of the delayed and summed seismic traces use the velocity (3.7 km/s) and the backazimuth (152 degrees) obtained from beamforming from the stations of the Morocco array for all glides detected from 2011 to 2012.

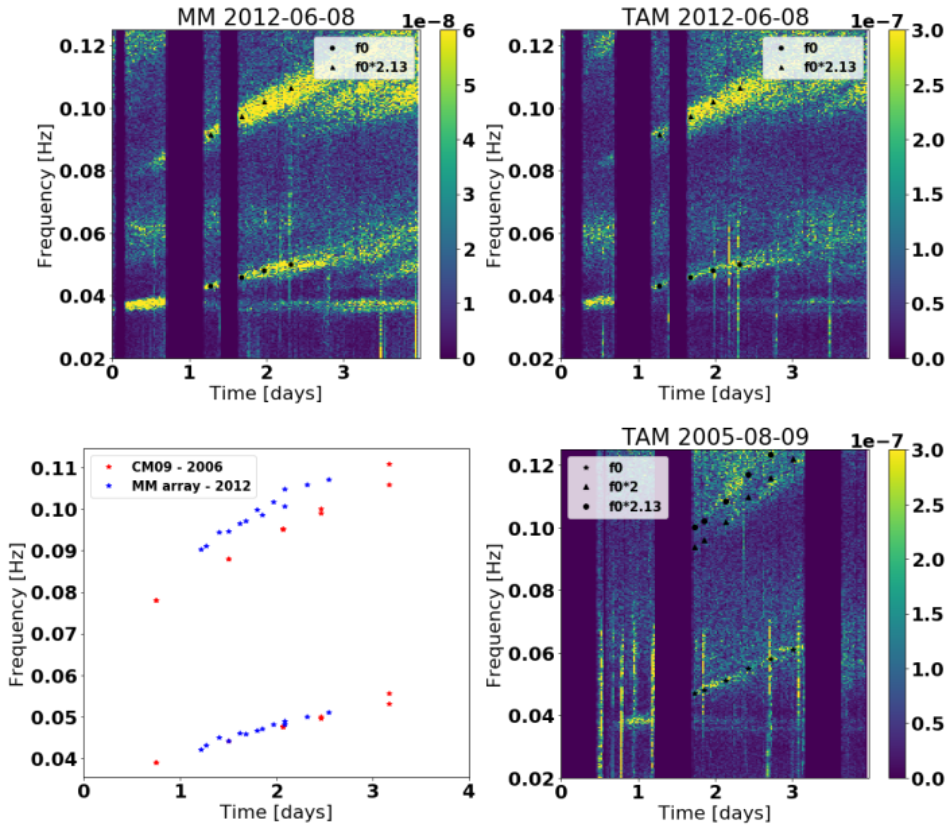

Figure 34:

a) Inharmonic overtone on MM array: The overtone appears to be shifted upwards, with the frequency of the overtone now being more than twice the frequency of the fundamental. The frequency picks from the spectral peaks are projected onto the data from TAM in b).

b) **Spectrogram from TAM compared to spectrogram from MM.** Picks from spectral peaks on MM is shown together and displays a great fit with the TAM data. Since frequency of the glide and the overtone is consistent for the two stations, the inharmonic spacing is likely not a path effect, but rather connected to the source of the tremor.

c) **Comparison of frequency of overtone for gliding observed at the MM array (Morocco) in 2012 and CM09 (Cameroon) in 2006.** For the Cameroon data (red), we observe regular harmonic spacing. For the Morocco data (blue) the spacing between the fundamental and the overtone is no longer harmonic. The overtone is consistently higher that what is predicted for regular harmonic spacing. The slopes for the fundamental is stable for all glide events. There are no clear changes between the two glides from May 2006 or the glides from May to July 2012.

d) **Double overtone:** Occasionally two neighboring peaks are observed at around twice the frequency of twice the overtone, here on TAM data from 2005. The lower glide is close to f0*2, while the upper is close to f0*2.13, which is close the spacing that is observed in the data from Cameroon from 2006 and Morocco 2012 respectively.

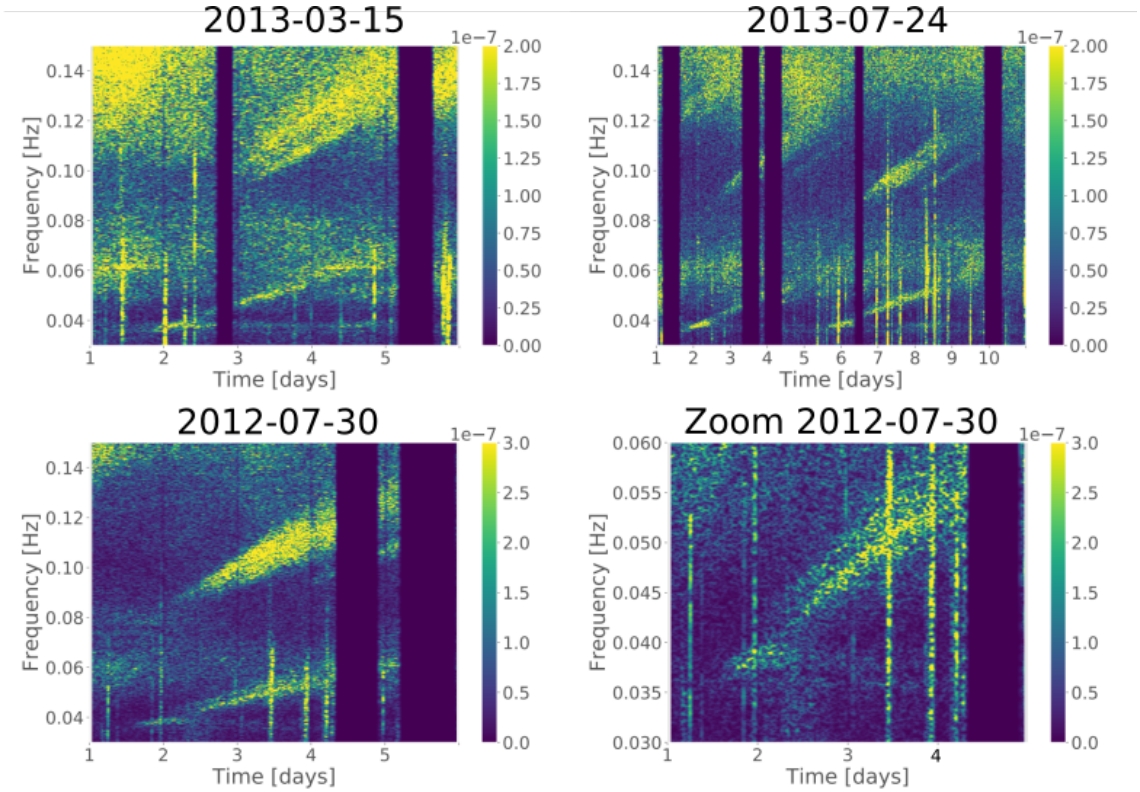

Figure 35: Examples of inharmonic overtones on TAM.

this, and other spectral estimates may be more appropriate to show the frequency of the signal over time, however, it is more computationally expensive.

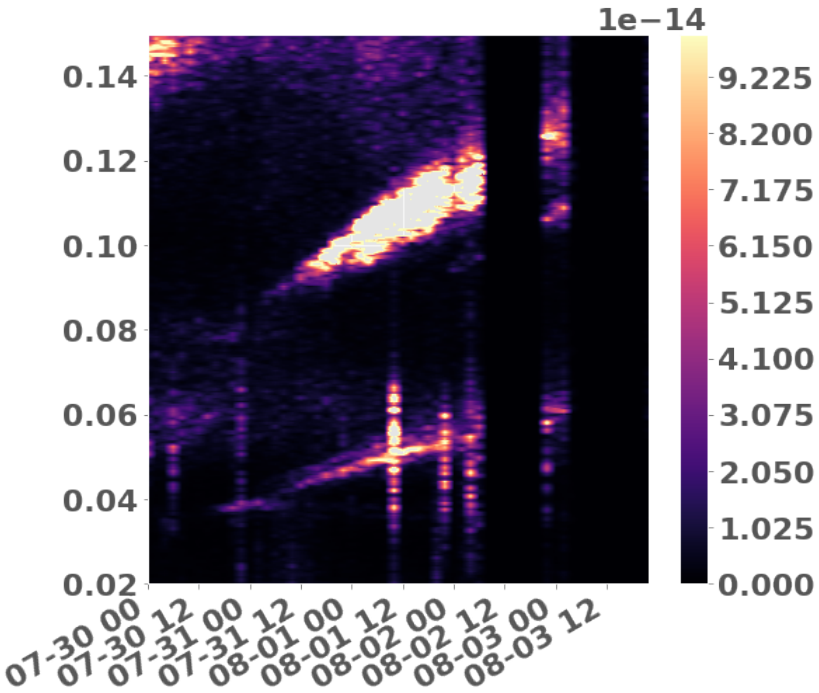

Figure 36: Spectrogram calculated for the glide 2012-07-30, spectra are calculated using a multitaper for 2 hour windows, with no overlap.

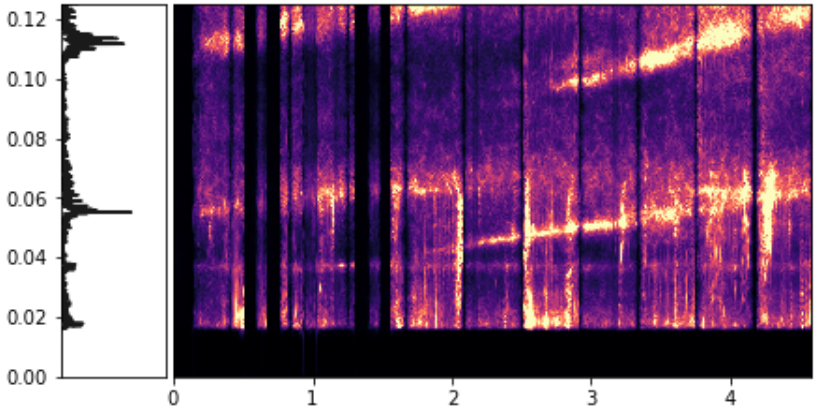

Figure 37: Example for the glide in May 12th 2006 on a station in the Cameroon array(CM09) using a multitaper approach. The right panel shows the resulting time frequency representation. The left panel shows the frequency for calculated for the first 12 hours.

7.6 Where to go next?

Many of the suggestions for future investigations involve new data, but what can we do with the data we already have? For future studies, getting a better estimate for the size of the resonator using the resonance frequencies would be a great starting point for designing an imaging study. Modelling the system could also give insights into what geometric changes or changes in the fluid properties that can produce the gliding tremor. Modelling the changes in resonance frequencies of the system could tell us something about how the system is evolving over time.

For oceanic studies, ocean wave models (such as WW3) for looking at the ocean wavestate when isolating longer period waves, will show if and where we would expect 26 s microseism generation to happen. Such studies could reveal if the volcanic and oceanic mechanisms that we have discussed are physically possible.

A Supporting Information

Table 5: List of broadband 3-C stations used in this study

Station	Array	Country	Latitude	Longitude
TAM	G	Algeria	22.79149	5.52838
SSB	G	France	45.279	4.542
BFO	GR	Germany	48.3301	8.3296
GRA1	GR	Germany	49.691888	11.22172
CM15	XB	Cameroon	5.034	9.933

Table 6: Description of array used for 3-C beamforming

FDSN code	3D
Network name	MM
Timespan	2011
Number of stations	15
Aperture (km)	383
Country	Morocco
Latitude	30.79255
Longitude	-7.59595

Table 7: Backazimuth for glides and 26 s microseism

Tremor type	Date	BAZ [degrees]
26 s microseism	2011-2012	152
Glide	2011-01-08	148
Glide	2011-05-10	148
Glide	2012-05-17	148
Glide	2012-06-10	148
Glide	2012-07-30	148

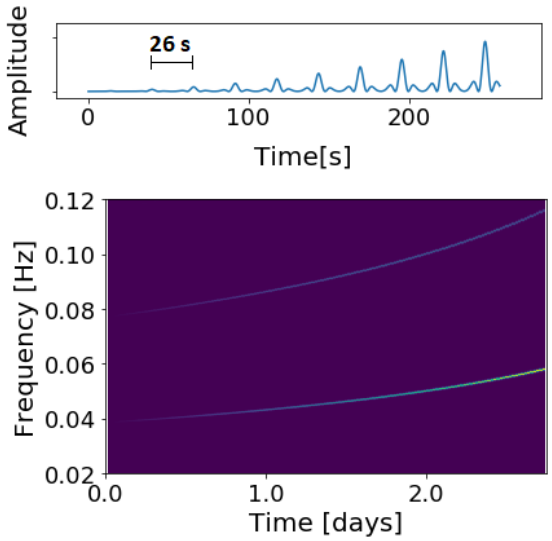

Figure 38: Synthetic model of repeated pulses. Harmonic tremor can arise from regularly repeated pulses, here shown using Ricker wavelets with a gradually increasing amplitude and a time lag gradually decreasing between the pulses from 26 s to 16 s. The top shows a zoom of the first 4 minutes of the signal in time. The spectrogram is calculated with a window length of 2 hours and an overlap of 0.5, and reproduces our observed gliding frequencies reasonably well.

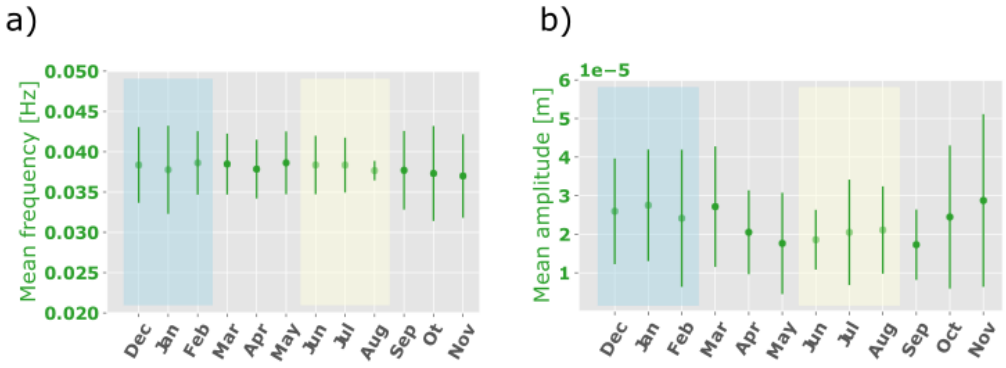

Figure 39: Mean spectral amplitude and frequency of detections: a) Monthly mean spectral amplitude of detections shown with standard deviation. The spectral amplitude is higher in winter months than summer months, and the values for spectral amplitude vary more in the winter months. b) Monthly mean frequency shown with standard deviation . The peak frequency is stable, but the detections are more scattered in frequency for winter months.

Table 8: Permanent broadband 3-C stations used in this study

Station	Array	Country	Latitude	Longitude
TAM	G	Algeria	22.79149	5.52838
SSB	G	France	45.279	4.542
BFO	GR	Germany	48.3301	8.3296
GRA1	GR	Germany	49.691888	11.22172

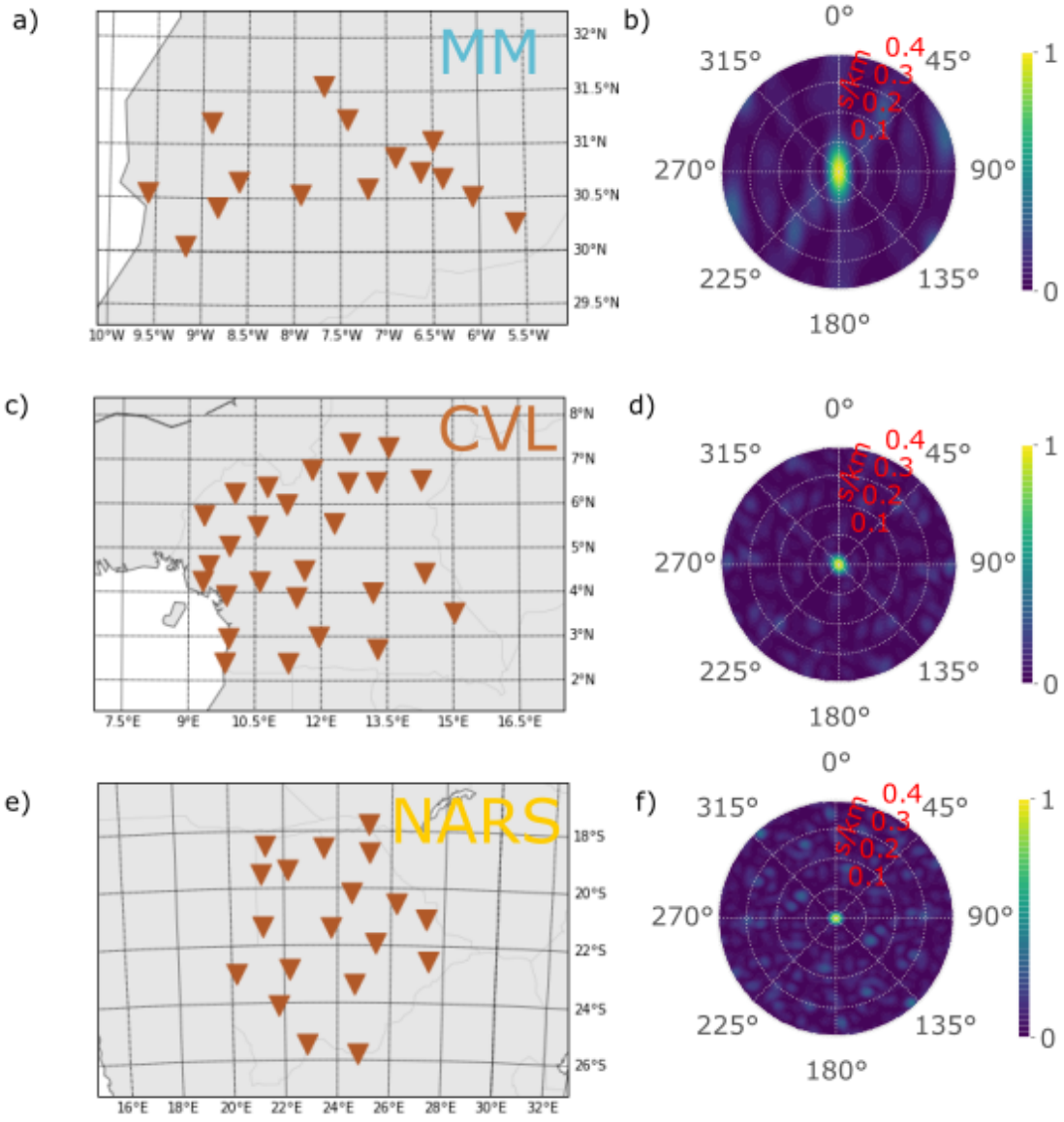

Figure 40: Resolution for arrays in Africa used for 3-C beamforming: The beamforming resolution is affected by the number of stations, spatial configuration and array aperture. To evaluate the performance of the different arrays, we study the beam power in the case of a single monochromatic plane wave coming from right below the array. The resolution capability of MM, NARS and CVL for at a frequency of 0.038 Hz for the given array geometry (a),c),e)) is shown in b), d) and f).

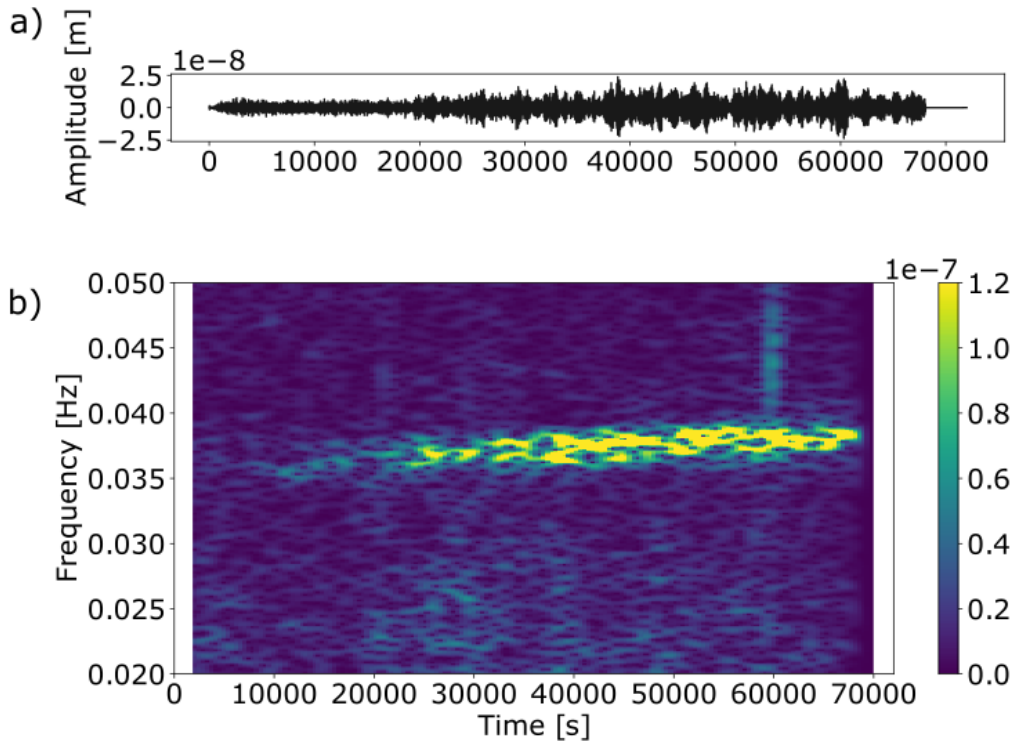

Figure 41: Emergent signal: We use the velocity (3.7 km/s) and the backazimuth (152 degrees) obtained from beamforming to delay and sum the traces from the stations of the Morocco array to look at the beginning of the glide signal in time for the glide on 2011-05-09. The resulting stacked waveform filtered between 0.02 and 0.05 Hz is shown in a). The signal is emergent, with no clear beginning. b) shows a spectrogram from the same time period with window length of 1 hour.

Table 9: Description of arrays used for 3-C beamforming

FDSN code	3D	NR	XB
Network name	MM	NARS	CVL
Timespan	2011-2013	2016	2006
Number of stations	15	19	27
Aperture (km)	383	888	679
Country	Morocco	Botswana	Cameroon
Latitude	30.79255	-21.80601	-19.401535
Longitude	-7.59595	23.82118	11.94225

References

The frequency dependence and locations of short-period microseisms generated in the southern Ocean and West Pacific, author=Gal, Martin and Reading, Anya M and Ellingsen, SP and Gualtieri, L and Koper, KD and Burlacu, R and Tkalčić, Hrvoje and Hemer, MA, journal=Journal of Geophysical Research: Solid Earth, volume=120, number=8, pages=5764–5781, year=2015, publisher=Wiley Online Library.

K. Aki and R. Koyanagi. Deep volcanic tremor and magma ascent mechanism under Kilauea, Hawaii. *Journal of Geophysical Research: Solid Earth*, 86(B8):7095–7109, 1981.

J. Almendros, J. Ibáñez, G. Alguacil, E. Del Pezzo, and R. Ortiz. Array tracking of the volcanic tremor source at Deception Island, Antarctica. *Geophysical Research Letters*, 24(23):3069–3072, 1997.

F. Ardhuin, E. Stutzmann, M. Schimmel, and A. Mangeney. Ocean wave sources of seismic noise. *Journal of Geophysical Research: Oceans*, 116(C9), 2011.

F. Ardhuin, A. Rawat, and J. Aucan. A numerical model for free infragravity waves: Definition and validation at regional and global scales. *Ocean Modelling*, 77:20–32, 2014.

F. Ardhuin, L. Gualtieri, and E. Stutzmann. How ocean waves rock the Earth: Two mechanisms explain microseisms with periods 3 to 300 s. *Geophysical Research Letters*, 42(3):765–772, 2015.

R. C. Aster, D. E. McNamara, and P. D. Bromirski. Multidecadal climate-induced variability in microseisms. *Seismological Research Letters*, 79(2):194–202, 2008.

R. C. Aster, D. E. McNamara, and P. D. Bromirski. Global trends in extremal microseism intensity. *Geophysical Research Letters*, 37(14), 2010.

A. B. Baggeroer, W. A. Kuperman, and P. N. Mikhalevsky. An overview of matched field methods in ocean acoustics. *IEEE Journal of Oceanic Engineering*, 18(4):401–424, 1993.

P. Bernard. Historical sketch of microseisms from past to future. *Physics of the earth and planetary interiors*, 63(3-4):145–150, 1990.

M. Beyreuther, R. Barsch, L. Krischer, T. Megies, Y. Behr, and J. Wassermann. ObsPy: A Python toolbox for seismology. *Seismological Research Letters*, 81(3):530–533, 2010.

B. Brandsdóttir and P. Einarsson. Volcanic tremor and low-frequency earthquakes in Iceland. In *Volcanic seismology*, pages 212–222. Springer, 1992.

F. Brenguier, N. M. Shapiro, M. Campillo, V. Ferrazzini, Z. Duputel, O. Coutant, and A. Nercessian. Towards forecasting volcanic eruptions using seismic noise. *Nature Geoscience*, 1(2):126–130, 2008.

F. Brenguier, D. Clarke, Y. Aoki, N. M. Shapiro, M. Campillo, and V. Ferrazzini. Monitoring volcanoes using seismic noise correlations. *Comptes Rendus Geoscience*, 343(8-9):633–638, 2011.

P. D. Bromirski. Earth vibrations. *Science*, 324(5930):1026–1027, 2009.

P. D. Bromirski and F. K. Duennebier. The near-coastal microseism spectrum: Spatial and temporal wave climate relationships. *Journal of Geophysical Research: Solid Earth*, 107(B8):ESE–5, 2002.

P. D. Bromirski and P. Gerstoft. Dominant source regions of the Earth's "hum" are coastal. *Geophysical Research Letters*, 36(13), 2009.

P. D. Bromirski, F. K. Duennebier, and R. A. Stephen. Mid-ocean microseisms. *Geochemistry, Geophysics, Geosystems*, 6(4), 2005.

K. Burke. Origin of the Cameroon line of volcano-capped swells. *The Journal of Geology*, 109(3): 349–362, 2001.

S. Bussat and S. Kugler. Offshore ambient-noise surface-wave tomography above 0.1 hz and its applications. *The Leading Edge*, 30(5):514–524, 2011.

S. Cesca, J. Letort, H. N. Razafindrakoto, S. Heimann, E. Rivalta, M. P. Isken, M. Nikkhoo, L. Passarelli, G. M. Petersen, F. Cotton, et al. Drainage of a deep magma reservoir near Mayotte inferred from seismicity and deformation. *Nature geoscience*, 13(1):87–93, 2020.

R. K. Cessaro. Sources of primary and secondary microseisms. *Bulletin of the Seismological Society of America*, 84(1):142–148, 1994.

R. K. Cessaro and W. W. Chan. Wide-angle triangulation array study of simultaneous primary microseism sources. *Journal of Geophysical Research: Solid Earth*, 94(B11):15555–15563, 1989.

W. Chadwick Jr, K. Cashman, R. Embley, H. Matsumoto, R. Dziak, C. De Ronde, T. Lau, N. Deardorff, and S. Merle. Direct video and hydrophone observations of submarine explosive eruptions at NW Rota-1 volcano, Mariana arc. *Journal of Geophysical Research: Solid Earth*, 113(B8), 2008.

Y. Chen, J. Xie, and S. Ni. Generation mechanism of the 26 s and 28 s tremors in the Gulf of Guinea from statistical analysis of magnitudes and event intervals. *Earth and Planetary Science Letters*, 578: 117334, 2022.

S. Chevrot, M. Sylvander, S. Benahmed, C. Ponsolles, J. Lefevre, and D. Paradis. Source locations of secondary microseisms in western Europe: Evidence for both coastal and pelagic sources. *Journal of Geophysical Research: Solid Earth*, 112(B11), 2007.

B. Chouet. Excitation of a buried magmatic pipe: a seismic source model for volcanic tremor. *Journal of Geophysical Research: Solid Earth*, 90(B2):1881–1893, 1985.

B. Chouet. Dynamics of a fluid-driven crack in three dimensions by the finite difference method. *Journal of Geophysical Research: Solid Earth*, 91(B14):13967–13992, 1986.

B. Chouet. Resonance of a fluid-driven crack: Radiation properties and implications for the source of long-period events and harmonic tremor. *Journal of Geophysical Research: Solid Earth*, 93(B5): 4375–4400, 1988.

CLS (France). GLOBAL OCEAN GRIDDED L4 SEA SURFACE HEIGHTS AND DERIVED VARIABLES REPROCESSED (1993-ONGOING), 2012. URL `https://doi.org/10.48670/moi-00148`.

CNR (Italy). Global Ocean OSTIA Sea Surface Temperature and Sea Ice Analysis, 2009. URL `https://doi.org/10.48670/moi-00165`.

T. Dahm. Numerical Studies of the Dynamics of Fluid-Filled Cracks Placed in Series: A Model for Inharmonic Peaked Tremor Spectra. In *Volcanic Seismology*, pages 190–200. Springer, 1992.

R. J. Davies, C. J. MacLeod, R. Morgan, and S. E. Briggs. Termination of a fossil continent-ocean fracture zone imaged with three-dimensional seismic data: The chain fracture zone, eastern equatorial Atlantic. *Geology*, 33(8):641–644, 2005.

C. Davy, G. Barruol, F. R. Fontaine, K. Sigloch, and E. Stutzmann. Tracking major storms from microseismic and hydroacoustic observations on the seafloor. *Geophysical Research Letters*, 41(24): 8825–8831, 2014.

P. B. Dawson, M. Benitez, B. A. Chouet, D. Wilson, and P. G. Okubo. Monitoring very-long-period seismicity at Kilauea Volcano, Hawaii. *Geophysical Research Letters*, 37(18), 2010.

S. De Ridder, B. Biondi, and R. Clapp. Time-lapse seismic noise correlation tomography at Valhall. *Geophysical Research Letters*, 41(17):6116–6122, 2014.

A. N. Douglas Wiens. Broadband Seismic Investigation of the Cameroon Volcanic Line, 2005. URL `http://www.fdsn.org/doi/10.7914/SN/XB_2005`.

J. J. Dvorak and A. T. Okamura. Variations in tilt rate and harmonic tremor amplitude during the January–August 1983 East Rift eruptions of Kilauea volcano, Hawaii. *Journal of volcanology and geothermal research*, 25(3-4):249–258, 1985.

R. P. Dziak and C. G. Fox. Evidence of harmonic tremor from a submarine volcano detected across the Pacific Ocean basin. *Journal of Geophysical Research: Solid Earth*, 107(B5):ESE–1, 2002.

C. W. Ebeling. Inferring ocean storm characteristics from ambient seismic noise: A historical perspective. In *Advances in geophysics*, volume 53, pages 1–33. Elsevier, 2012.

E. P. Eibl, I. Lokmer, C. J. Bean, E. Akerlie, and K. S. Vogfjörd. Helicopter vs. volcanic tremor: Characteristic features of seismic harmonic tremor on volcanoes. *Journal of Volcanology and Geothermal Research*, 304:108–117, 2015.

D. Ereditato and G. Luongo. Volcanic tremor wave field during quiescent and eruptive activity at Mt. Etna (Sicily). *Journal of volcanology and geothermal research*, 61(3-4):239–251, 1994.

C. Esmersoy, V. Cormier, M. Toksoz, and A. Kerr. Three-component array processing. *The VELA Program. A Twenty-Five Year Review of Basic Research*, 78(5):1725–1743, 1985.

J. D. Fairhead. Mesozoic plate tectonic reconstructions of the central South Atlantic Ocean: the role of the West and Central African rift system. *Tectonophysics*, 155(1-4):181–191, 1988.

W. Fan, J. J. McGuire, C. D. de Groot-Hedlin, M. A. Hedlin, S. Coats, and J. W. Fiedler. Stormquakes. *Geophysical Research Letters*, 46(22):12909–12918, 2019.

Federal Institute for Geosciences and Natural Resources. German Regional Seismic Network (GRSN), 1976. URL `https://www.seismologie.bgr.de/doi/grsn/`.

M. Fehler. Observations of volcanic tremor at Mount St. Helens volcano. *Journal of Geophysical Research: Solid Earth*, 88(B4):3476–3484, 1983.

V. Ferrazzini and K. Aki. Slow waves trapped in a fluid-filled infinite crack: Implication for volcanic tremor. *Journal of Geophysical Research: Solid Earth*, 92(B9):9215–9223, 1987.

V. Ferrazzini, K. Aki, and B. Chouet. Characteristics of seismic waves composing Hawaiian volcanic tremor and gas-piston events observed by a near-source array. *Journal of Geophysical Research: Solid Earth*, 96(B4):6199–6209, 1991.

M. Ferrick, A. Qamar, and W. St. Lawrence. Source mechanism of volcanic tremor. *Journal of Geophysical Research: Solid Earth*, 87(B10):8675–8683, 1982.

J. Fitton. The Benue trough and Cameroon line—a migrating rift system in West Africa. *Earth and Planetary Science Letters*, 51(1):132–138, 1980.

J. Fitton. The Cameroon line, West Africa: a comparison between oceanic and continental alkaline volcanism. *Geological Society, London, Special Publications*, 30(1):273–291, 1987.

J. Fitton and H. Dunlop. The Cameroon line, West Africa, and its bearing on the origin of oceanic and continental alkali basalt. *Earth and Planetary Science Letters*, 72(1):23–38, 1985.

P. Franek, J. Mienert, S. Buenz, and L. Géli. Character of seismic motion at a location of a gas hydrate-bearing mud volcano on the SW Barents Sea margin. *Journal of Geophysical Research: Solid Earth*, 119(8):6159–6177, 2014.

A. Friedrich, F. Krüger, and K. Klinge. Ocean-generated microseismic noise located with the Gräfenberg array. *Journal of Seismology*, 2(1):47–64, 1998.

B. Froment, M. Campillo, P. Roux, P. Gouedard, A. Verdel, and R. L. Weaver. Estimation of the effect of nonisotropically distributed energy on the apparent arrival time in correlations. *Geophysics*, 75(5): SA85–SA93, 2010.

F. Fuchs and G. Bokelmann. Equidistant spectral lines in train vibrations. *Seismological Research Letters*, 89(1):56–66, 2018.

Y. Fukao, E. Fujita, S. Hori, and K. Kanjo. Response of a volcanic conduit to step-like change in magma pressure. *Geophysical research letters*, 25(1):105–108, 1998.

Y. Fukao, K. Nishida, N. Suda, K. Nawa, and N. Kobayashi. A theory of the Earth's background free oscillations. *Journal of Geophysical Research: Solid Earth*, 107(B9):ESE–11, 2002.

Y. Fukao, K. Nishida, and N. Kobayashi. Seafloor topography, ocean infragravity waves, and background Love and Rayleigh waves. *Journal of Geophysical Research: Solid Earth*, 115(B4), 2010.

M. Gal and A. M. Reading. Beamforming and polarisation analysis. *Seismic Ambient Noise*, pages 32–72, 2019.

P. Gasparini, R. Scarpa, and K. Aki. Preliminary results from a field experiment on volcanic events at Kilauea using an array of digital seismographs. In *Volcanic Seismology*, pages 168–189. Springer, 1992.

P. Gouédard, P. Roux, M. Campillo, and A. Verdel. Convergence of the two-point correlation function toward the Green's function in the context of a seismic-prospecting data set. *Geophysics*, 73(6): V47–V53, 2008.

K. Graue. Mud volcanoes in deepwater Nigeria. *Marine and Petroleum Geology*, 17(8):959–974, 2000.

D. N. Green, L. G. Evers, D. Fee, R. S. Matoza, M. Snellen, P. Smets, and D. Simons. Hydroacoustic, infrasonic and seismic monitoring of the submarine eruptive activity and sub-aerial plume generation at South Sarigan, May 2010. *Journal of Volcanology and Geothermal Research*, 257:31–43, 2013.

I. Grevemeyer, R. Herber, and H.-H. Essen. Microseismological evidence for a changing wave climate in the northeast Atlantic Ocean. *Nature*, 408(6810):349–352, 2000.

L. Gualtieri, E. Stutzmann, Y. Capdeville, F. Ardhuin, M. Schimmel, A. Mangeney, and A. Morelli. Modelling secondary microseismic noise by normal mode summation. *Geophysical Journal International*, 193(3):1732–1745, 2013.

L. Gualtieri, S. J. Camargo, S. Pascale, F. M. Pons, and G. Ekström. The persistent signature of tropical cyclones in ambient seismic noise. *Earth and Planetary Science Letters*, 484:287–294, 2018.

C. Hadziioannou, P. Gaebler, U. Schreiber, J. Wassermann, and H. Igel. Examining ambient noise using colocated measurements of rotational and translational motion. *Journal of seismology*, 16(4): 787–796, 2012.

M. Hagerty, S. Y. Schwartz, M. Garces, and M. Protti. Analysis of seismic and acoustic observations at Arenal Volcano, Costa Rica, 1995–1997. *Journal of Volcanology and Geothermal Research*, 101(1-2): 27–65, 2000.

K. Hasselmann. A statistical analysis of the generation of microseisms. *Reviews of Geophysics*, 1(2): 177–210, 1963.

R. Haubrich, W. Munk, and F. Snodgrass. Comparative spectra of microseisms and swell. *Bulletin of the Seismological Society of America*, 53(1):27–37, 1963.

R. A. Haubrich and K. McCamy. Microseisms: Coastal and pelagic sources. *Reviews of Geophysics*, 7 (3):539–571, 1969.

M. Hellweg. Physical models for the source of Lascar's harmonic tremor. *Journal of Volcanology and Geothermal Research*, 101(1-2):183–198, 2000.

A. Helmstetter, L. Moreau, B. Nicolas, P. Comon, and M. Gay. Intermediate-depth icequakes and harmonic tremor in an Alpine glacier (Glacier d'Argentière, France): Evidence for hydraulic fracturing? *Journal of Geophysical Research: Earth Surface*, 120(3):402–416, 2015.

G. Hillers, N. Graham, M. Campillo, S. Kedar, M. Landès, and N. Shapiro. Global oceanic microseism sources as seen by seismic arrays and predicted by wave action models. *Geochemistry, Geophysics, Geosystems*, 13(1), 2012.

A. Hofstetter and S. D. Malone. Observations of volcanic tremor at Mount St. Helens in April and May 1980. *Bulletin of the Seismological Society of America*, 76(4):923–938, 1986.

L. G. Holcomb. Microseisms: A twenty-six-second spectral line in long-period earth motion. *Bulletin of the Seismological Society of America*, 70(4):1055–1070, 1980.

L. G. Holcomb. Spectral structure in the Earth's microseismic background between 20 and 40 seconds. *Bulletin of the Seismological Society of America*, 88(3):744–757, 1998.

A. J. Hotovec, S. G. Prejean, J. E. Vidale, and J. Gomberg. Strongly gliding harmonic tremor during the 2009 eruption of Redoubt Volcano. *Journal of Volcanology and Geothermal Research*, 259:89–99, 2013.

Institut De Physique Du Globe De Paris (IPGP) and Ecole Et Observatoire Des Sciences De La Terre De Strasbourg (EOST). GEOSCOPE, French Global Network of broad band seismic stations, 1982. URL `http://geoscope.ipgp.fr/networks/detail/G/`.

ISC On-line Bulletin. International Seismological Centre, 2021. URL https://doi.org/10.31905/D808B830.

J. Johnson and J. Lees. Plugs and chugs—seismic and acoustic observations of degassing explosions at Karymsky, Russia and Sangay, Ecuador. *Journal of Volcanology and Geothermal Research*, 101(1-2): 67–82, 2000.

B. R. Julian. Volcanic tremor: Nonlinear excitation by fluid flow. *Journal of Geophysical Research: Solid Earth*, 99(B6):11859–11877, 1994.

C. Juretzek and C. Hadziioannou. Where do ocean microseisms come from? A study of Love-to-Rayleigh wave ratios. *Journal of Geophysical Research: Solid Earth*, 121(9):6741–6756, 2016.

C. Juretzek and C. Hadziioannou. Linking source region and ocean wave parameters with the observed primary microseismic noise. *Geophysical Journal International*, 211(3):1640–1654, 2017.

S. Kaneshima, H. Kawakatsu, H. Matsubayashi, Y. Sudo, T. Tsutsui, T. Ohminato, H. Ito, K. Uhira, H. Yamasato, J. Oikawa, et al. Mechanism of phreatic eruptions at Aso Volcano inferred from near-field broadband seismic observations. *Science*, 273(5275):642–645, 1996.

H. Kawakatsu, S. Kaneshima, H. Matsubayashi, T. Ohminato, Y. Sudo, T. Tsutsui, K. Uhira, H. Yamasato, H. Ito, and D. Legrand. Aso94: Aso seismic observation with broadband instruments. *Journal of Volcanology and Geothermal Research*, 101(1-2):129–154, 2000.

Y. Kawano, T. Isse, A. Takeo, H. Kawakatsu, D. Suetsugu, H. Shiobara, H. Sugioka, A. Ito, Y. Ishihara, S. Tanaka, et al. Persistent Long-Period Signals Recorded by an OBS Array in the Western-Central Pacific: Activity of Ambrym Volcano in Vanuatu. *Geophysical Research Letters*, 47(19):e2020GL089108, 2020.

S. Kedar, B. Sturtevant, and H. Kanamori. The origin of harmonic tremor at Old Faithful geyser. *Nature*, 379(6567):708–711, 1996.

S. Kedar, M. Longuet-Higgins, F. Webb, N. Graham, R. Clayton, and C. Jones. The origin of deep ocean microseisms in the North Atlantic Ocean. *Proceedings of the Royal Society A: Mathematical, Physical and Engineering Sciences*, 464(2091):777–793, 2008.

S. W. Kieffer. Seismicity at Old Faithful Geyser: An isolated source of geothermal noise and possible analogue of volcanic seismicity. *Journal of Volcanology and Geothermal Research*, 22(1-2):59–95, 1984.

W. Kimman, X. Campman, and J. Trampert. Characteristics of seismic noise: fundamental and higher mode energy observed in the northeast of the netherlands. *Bulletin of the Seismological Society of America*, 102(4):1388–1399, 2012.

K. R. Knapp, S. Applequist, H. J. Diamond, J. P. Kossin, M. Kruk, and C. Schreck. NCDC international best track archive for climate stewardship (IBTrACS) project, version 3. *See https://data. noaa. gov/dataset/ncdc-international-best-track-archive-forclimate-stewardship-ibtracs-project-version-3*, 2010a.

K. R. Knapp, M. C. Kruk, D. H. Levinson, H. J. Diamond, and C. J. Neumann. The international best track archive for climate stewardship (IBTrACS) unifying tropical cyclone data. *Bulletin of the American Meteorological Society*, 91(3):363–376, 2010b.

N. Kobayashi and K. Nishida. Continuous excitation of planetary free oscillations by atmospheric disturbances. *Nature*, 395(6700):357–360, 1998.

K. I. Konstantinou and V. Schlindwein. Nature, wavefield properties and source mechanism of volcanic tremor: a review. *Journal of Volcanology and Geothermal Research*, 119(1-4):161–187, 2003.

L. Krischer. mtspec Python wrappers 0.3. 2. *Dataset, doi*, 10, 2016.

L. Krischer, T. Megies, R. Barsch, M. Beyreuther, T. Lecocq, C. Caudron, and J. Wassermann. ObsPy: A bridge for seismology into the scientific Python ecosystem. *Computational Science & Discovery*, 8 (1):014003, 2015.

D. Kurrle and R. Widmer-Schnidrig. Spatiotemporal features of the Earth's background oscillations observed in central Europe. *Geophysical research letters*, 33(24), 2006.

M. Landès, F. Hubans, N. M. Shapiro, A. Paul, and M. Campillo. Origin of deep ocean microseisms by using teleseismic body waves. *Journal of Geophysical Research: Solid Earth*, 115(B5), 2010.

C. W. Landsea and J. L. Franklin. Atlantic hurricane database uncertainty and presentation of a new database format. *Monthly Weather Review*, 141(10):3576–3592, 2013.

J. M. Lees, E. I. Gordeev, and M. Ripepe. Explosions and periodic tremor at Karymsky volcano, Kamchatka, Russia. *Geophysical Journal International*, 158(3):1151–1167, 2004.

R. C. Leet. Saturated and subcooled hydrothermal boiling in groundwater flow channels as a source of harmonic tremor. *Journal of Geophysical Research: Solid Earth*, 93(B5):4835–4849, 1988.

P. Lesage, M. M. Mora, G. E. Alvarado, J. Pacheco, and J.-P. Métaxian. Complex behavior and source model of the tremor at Arenal volcano, Costa Rica. *Journal of Volcanology and Geothermal Research*, 157(1-3):49–59, 2006.

K. Löer, N. Riahi, and E. H. Saenger. Three-component ambient noise beamforming in the Parkfield area. *Geophysical Journal International*, 213(3):1478–1491, 2018.

M. S. Longuet-Higgins. A theory of the origin of microseisms. *Philosophical Transactions of the Royal Society of London. Series A, Mathematical and Physical Sciences*, 243(857):1–35, 1950.

D. MacAyeal, E. Okal, R. Aster, and J. Bassis. Seismic and hydroacoustic tremor generated by colliding icebergs. *Journal of Geophysical Research: Earth Surface*, 113(F3), 2008.

D. R. MacAyeal, E. A. Okal, R. C. Aster, and J. N. Bassis. Seismic observations of glaciogenic ocean waves (micro-tsunamis) on icebergs and ice shelves. *Journal of Glaciology*, 55(190):193–206, 2009.

Y. Maeda and H. Kumagai. A generalized equation for the resonance frequencies of a fluid-filled crack. *Geophysical Journal International*, 209(1):192–201, 2017.

T. Matsuzawa, K. Obara, T. Maeda, Y. Asano, and T. Saito. Love-and rayleigh-wave microseisms excited by migrating ocean swells in the North Atlantic detected in Japan and Germany. *Bulletin of the Seismological Society of America*, 102(4):1864–1871, 2012.

S. R. McNutt. Observations and analysis of B-type earthquakes, explosions, and volcanic tremor at Pavlof volcano, Alaska. *Bulletin of the Seismological Society of America*, 76(1):153–175, 1986.

S. R. McNutt. Volcanic tremor. *Encyclopedia of earth system science*, 4:417–425, 1992.

S. R. McNutt. Seismic monitoring and eruption forecasting of volcanoes: a review of the state-of-the-art and case histories. *Monitoring and mitigation of volcano hazards*, pages 99–146, 1996.

M. Meschede, É. Stutzmann, V. Farra, M. Schimmel, and F. Ardhuin. The effect of water column resonance on the spectra of secondary microseism p waves. *Journal of Geophysical Research: Solid Earth*, 122(10):8121–8142, 2017.

J.-P. Métaxian, P. Lesage, and J. Dorel. Permanent tremor of Masaya Volcano, Nicaragua: Wave field analysis and source location. *Journal of Geophysical Research: Solid Earth*, 102(B10):22529–22545, 1997.

D. Metz, A. B. Watts, I. Grevemeyer, M. Rodgers, and M. Paulatto. Ultra-long-range hydroacoustic observations of submarine volcanic activity at Monowai, Kermadec Arc. *Geophysical Research Letters*, 43(4):1529–1536, 2016.

J. B. Meyers, B. R. Rosendahl, C. G. Harrison, and Z.-D. Ding. Deep-imaging seismic and gravity results from the offshore Cameroon Volcanic Line, and speculation of African hotlines. *Tectonophysics*, 284 (1-2):31–63, 1998.

A. Mordret, M. Landès, N. Shapiro, S. Singh, P. Roux, and O. Barkved. Near-surface study at the Valhall oil field from ambient noise surface wave tomography. *Geophysical Journal International*, 193 (3):1627–1643, 2013.

M. M. Morrissey and B. A. Chouet. A numerical investigation of choked flow dynamics and its application to the triggering mechanism of long-period events at Redoubt Volcano, Alaska. *Journal of Geophysical Research: Solid Earth*, 102(B4):7965–7983, 1997.

A. Nayak, M. Manga, S. Hurwitz, A. Namiki, and P. B. Dawson. Origin and properties of hydrothermal tremor at Lone Star Geyser, Yellowstone National Park, USA. *Journal of Geophysical Research: Solid Earth*, 125(12):e2020JB019711, 2020.

J. Neale, N. Harmon, and M. Srokosz. Monitoring remote ocean waves using P-wave microseisms. *Journal of Geophysical Research: Oceans*, 122(1):470–483, 2017.

J. Neuberg. Characteristics and causes of shallow seismicity in andesite volcanoes. *Philosophical Transactions of the Royal Society of London. Series A: Mathematical, Physical and Engineering Sciences*, 358(1770):1533–1546, 2000.

V. Ngako, E. Njonfang, F. T. Aka, P. Affaton, and J. M. Nnange. The north–south paleozoic to quaternary trend of alkaline magmatism from niger–nigeria to cameroon: complex interaction between hotspots and precambrian faults. *Journal of African Earth Sciences*, 45(3):241–256, 2006.

K. Nishida. Ambient seismic wave field. *Proceedings of the Japan Academy, Series B*, 93(7):423–448, 2017.

K. Nishida and Y. Fukao. Source distribution of Earth's background free oscillations. *Journal of Geophysical Research: Solid Earth*, 112(B6), 2007.

K. Nishida and K. Shiomi. Enigmatic very low frequency tremors beneath the Shonai Plain in northeastern Japan. *Journal of Geophysical Research: Solid Earth*, 117(B11), 2012.

K. Nishida, H. Kawakatsu, Y. Fukao, and K. Obara. Background Love and Rayleigh waves simultaneously generated at the Pacific Ocean floors. *Geophysical Research Letters*, 35(16), 2008.

J. Niu and T.-R. A. Song. Real-time and in-situ assessment of conduit permeability through diverse long-period tremors beneath aso volcano, japan. *Journal of Volcanology and Geothermal Research*, 401:106964, 2020.

M. Obrebski, F. Ardhuin, E. Stutzmann, and M. Schimmel. Detection of microseismic compressional (P) body waves aided by numerical modeling of oceanic noise sources. *Journal of Geophysical Research: Solid Earth*, 118(8):4312–4324, 2013.

T. Ohminato. Characteristics and source modeling of broadband seismic signals associated with the hydrothermal system at Satsuma–Iwojima volcano, Japan. *Journal of volcanology and geothermal research*, 158(3-4):467–490, 2006.

T. Ohminato and D. Ereditato. Broadband seismic observations at Satsuma-Iwojima volcano, Japan. *Geophysical research letters*, 24(22):2845–2848, 1997.

J. Oikawa, Y. Ida, K. Yamaoka, H. Watanabe, E. Fukuyama, and K. Sato. Ground deformation associated with volcanic tremor at Izu-Oshima volcano. *Geophysical Research Letters*, 18(3):443–446, 1991.

J. Oliver. A worldwide storm of microseisms with periods of about 27 seconds. *Bulletin of the Seismological Society of America*, 52(3):507–517, 1962.

W. J. Pierson Jr and L. Moskowitz. A proposed spectral form for fully developed wind seas based on the similarity theory of SA Kitaigorodskii. *Journal of geophysical research*, 69(24):5181–5190, 1964.

T. Powell and J. Neuberg. Time dependent features in tremor spectra. *Journal of Volcanology and Geothermal Research*, 128(1-3):177–185, 2003.

G. A. Prieto, R. Parker, and F. Vernon Iii. A Fortran 90 library for multitaper spectrum analysis. *Computers & Geosciences*, 35(8):1701–1710, 2009.

L. Retailleau and L. Gualtieri. Toward high-resolution period-dependent seismic monitoring of tropical cyclones. *Geophysical research letters*, 46(3):1329–1337, 2019.

A. Reusch, A. A. Nyblade, D. Wiens, P. Shore, B. Ateba, C. Tabod, and J. Nnange. Upper mantle structure beneath Cameroon from body wave tomography and the origin of the Cameroon Volcanic Line. *Geochemistry, Geophysics, Geosystems*, 11(10), 2010.

J. Rhie and B. Romanowicz. Excitation of Earth's continuous free oscillations by atmosphere–ocean–seafloor coupling. *Nature*, 431(7008):552–556, 2004.

J. Rhie and B. Romanowicz. A study of the relation between ocean storms and the Earth's hum. *Geochemistry, Geophysics, Geosystems*, 7(10), 2006.

N. Riahi, G. Bokelmann, P. Sala, and E. H. Saenger. Time-lapse analysis of ambient surface wave anisotropy: A three-component array study above an underground gas storage. *Journal of Geophysical Research: Solid Earth*, 118(10):5339–5351, 2013.

S. Rost and C. Thomas. Array seismology: Methods and applications. *Reviews of geophysics*, 40(3): 2–1, 2002.

K. G. Sabra, P. Gerstoft, P. Roux, W. Kuperman, and M. C. Fehler. Extracting time-domain Green's function estimates from ambient seismic noise. *Geophysical Research Letters*, 32(3), 2005a.

K. G. Sabra, P. Gerstoft, P. Roux, W. Kuperman, and M. C. Fehler. Surface wave tomography from microseisms in Southern California. *Geophysical Research Letters*, 32(14), 2005b.

T. Saito. Love-wave excitation due to the interaction between a propagating ocean wave and the sea-bottom topography. *Geophysical Journal International*, 182(3):1515–1523, 2010.

D. T. Sandwell and W. H. Smith. Marine gravity anomaly from Geosat and ERS 1 satellite altimetry. *Journal of Geophysical Research: Solid Earth*, 102(B5):10039–10054, 1997.

K. Sassa. Volcanic micro-tremors and eruption-earthquakes. *Mem. Coll. Sci., Kyoto Imp. Univ. Series A*, 18:255–293, 1935.

S. Schippkus and C. Hadziioannou. Matched field processing for complex Earth structure. 2021.

S. Schippkus, M. Garden, and G. Bokelmann. Characteristics of the ambient seismic field on a large-N seismic array in the Vienna basin. *Seismological Society of America*, 91(5):2803–2816, 2020.

V. Schlindwein, J. Wassermann, and F. Scherbaum. Spectral analysis of harmonic tremor signals at Mt. Semeru volcano, Indonesia. *Geophysical research letters*, 22(13):1685–1688, 1995.

C. Searcy. Seismicity associated with the may 2010 eruption of South Sarigan Seamount, northern Mariana Islands. *Seismological Research Letters*, 84(6):1055–1061, 2013.

D. Seidl, S. Kirbani, and W. Brüstle. Maximum entropy spectral analysis of volcanic tremor using data from Etna (Sicily) and Merapi (central Java). *Bulletin of volcanology*, 52(6):460–474, 1990.

N. M. Shapiro and M. Campillo. Emergence of broadband Rayleigh waves from correlations of the ambient seismic noise. *Geophysical Research Letters*, 31(7), 2004.

N. M. Shapiro, M. Ritzwoller, and G. Bensen. Source location of the 26 sec microseism from cross-correlations of ambient seismic noise. *Geophysical Research Letters*, 33(18), 2006.

J. Soubestre, B. Chouet, and P. Dawson. Sources of Volcanic Tremor Associated With the Summit Caldera Collapse During the 2018 East Rift Eruption of Kı¯ lauea Volcano, Hawaii. *Journal of Geophysical Research: Solid Earth*, page e2020JB021572, 2021.

W. St. Lawrence and A. Qamar. Hydraulic transients: A seismic source in volcanoes and glaciers. *Science*, 203(4381):654–656, 1979.

L. Stehly, B. Fry, M. Campillo, N. Shapiro, J. Guilbert, L. Boschi, and D. Giardini. Tomography of the Alpine region from observations of seismic ambient noise. *Geophysical Journal International*, 178(1): 338–350, 2009.

E. Stutzmann, M. Schimmel, G. Patau, and A. Maggi. Global climate imprint on seismic noise. *Geochemistry, Geophysics, Geosystems*, 10(11), 2009.

E. Stutzmann, F. Ardhuin, M. Schimmel, A. Mangeney, and G. Patau. Modelling long-term seismic noise in various environments. *Geophysical Journal International*, 191(2):707–722, 2012.

E. Suriñach Cornet, I. Vilajosana Guillén, G. Khazaradze, B. Biescas Górriz, G. Furdada i Bellavista, and J. M. Vilaplana. Seismic detection and characterization of landslides and other mass movements. *Natural Hazards and Earth System Sciences, 2005, Vol. 5, p. 791-798*, 2005.

T. Tanimoto. Excitation of normal modes by atmospheric turbulence: source of long-period seismic noise. *Geophysical Journal International*, 136(2):395–402, 1999.

T. Tanimoto. Excitation of microseisms: views from the normal-mode approach. *Geophysical Journal International*, 194(3):1755–1759, 2013.

T. Tanimoto, C.-J. Lin, C. Hadziioannou, H. Igel, and F. Vernon. Estimate of Rayleigh-to-Love wave ratio in the secondary microseism by a small array at Piñon Flat Observatory, California. *Geophysical Research Letters*, 43(21):11–173, 2016.

T. O. D. Team. Obspy 1.2.0, Mar. 2020. URL `https://doi.org/10.5281/zenodo.3674646`.

G. Tepp and R. P. Dziak. The Seismo-acoustics of Submarine Volcanic Eruptions. *Journal of Geophysical Research: Solid Earth*, 126(4):e2020JB020912, 2021.

G. Tepp and M. M. Haney. Comparison of short-term seismic precursors and explosion parameters during the 2016–2017 Bogoslof eruption. *Bulletin of Volcanology*, 81(11):1–15, 2019.

G. Tepp, W. W. Chadwick Jr, M. M. Haney, J. J. Lyons, R. P. Dziak, S. G. Merle, D. A. Butterfield, and C. W. Young III. Hydroacoustic, seismic, and bathymetric observations of the 2014 submarine eruption at Ahyi seamount, Mariana Arc. *Geochemistry, Geophysics, Geosystems*, 20(7):3608–3627, 2019.

C. Thomas. Morocco-Muenster, 2010. URL `http://www.fdsn.org/doi/10.7914/SN/3D`$_2010$.

M. N. Toksöz and R. T. Lacoss. Microseisms: Mode structure and sources. *Science*, 159(3817):872–873, 1968.

H. L. Tolman et al. User manual and system documentation of WAVEWATCH III TM version 3.14. *Technical note, MMAB Contribution*, 276(220), 2009.

J. Traer, P. Gerstoft, P. D. Bromirski, and P. M. Shearer. Microseisms and hum from ocean surface gravity waves. *Journal of Geophysical Research: Solid Earth*, 117(B11), 2012.

V. C. Tsai. On establishing the accuracy of noise tomography travel-time measurements in a realistic medium. *Geophysical Journal International*, 178(3):1555–1564, 2009.

V. C. Tsai. Understanding the amplitudes of noise correlation measurements. *Journal of Geophysical Research: Solid Earth*, 116(B9), 2011.

K. Tsuruga, K. Yomogida, S. Honda, H. Ito, T. Ohminato, and H. Kawakatsu. Spatial and temporal variations of volcanic earthquakes at Sakurajima Volcano, Japan. *Journal of volcanology and geothermal research*, 75(3-4):337–358, 1997.

K. C. Unglert. *Towards a global classification of volcanic tremor*. PhD thesis, University of British Columbia, 2016.

Utrecht University (UU Netherlands). Nars, 1983. URL `https://www.fdsn.org/networks/detail/NR/`.

S. Watada and H. Kanamori. Acoustic resonant oscillations between the atmosphere and the solid earth during the 1991 Mt. Pinatubo eruption. *Journal of Geophysical Research: Solid Earth*, 115(B12), 2010.

S. Watada and G. Masters. Oceanic excitation of the continuous oscillations of the Earth. In *AGU Fall Meeting Abstracts*, volume 2001, pages S32A–0620, 2001.

U. Wegler and D. Seidl. Kinematic parameters of the tremor wave field at Mt. Etna (Sicily). *Geophysical research letters*, 24(7):759–762, 1997.

U. Wegler and C. Sens-Schönfelder. Fault zone monitoring with passive image interferometry. *Geophysical Journal International*, 168(3):1029–1033, 2007.

H. W. Wijesekera, D. W. Wang, W. J. Teague, and E. Jarosz. High sea-floor stress induced by extreme hurricane waves. *Geophysical research letters*, 37(11), 2010.

K. F. Woolfe, S. Lani, K. G. Sabra, and W. A. Kuperman. Monitoring deep-ocean temperatures using acoustic ambient noise. *Geophysical Research Letters*, 42(8):2878–2884, 2015.

Y. Xia and X. Chen. Observation of a New Long-Period (16-s) Persistent Tremor Originating in the Gulf of Guinea. *Geophysical Research Letters*, 47(15):e2020GL088137, 2020.

Y. Xia, S. Ni, and X. Zeng. Twin enigmatic microseismic sources in the Gulf of Guinea observed on intercontinental seismic stations. *Geophysical Journal International*, 194(1):362–366, 2013.

J. Xie, Y. Luo, and Y. Yang. Retrieving PmP travel times from a persistent localized microseismic source. *Geophysical Research Letters*, 48(21):e2021GL094827, 2021.

M. Yamamoto, H. Kawakatsu, S. Kaneshima, T. Mori, T. Tsutsui, Y. Sudo, and Y. Morita. Detection of a crack-like conduit beneath the active crater at Aso Volcano Japan. *Geophysical research letters*, 26(24):3677–3680, 1999.

X. Zeng and S. Ni. Evidence for an independent 26-s microseismic source near the Vanuatu Islands. *Pure and Applied Geophysics*, 171(9):2155–2163, 2014.

Y. Zheng, W. Shen, L. Zhou, Y. Yang, Z. Xie, and M. H. Ritzwoller. Crust and uppermost mantle beneath the North China Craton, northeastern China, and the Sea of Japan from ambient noise tomography. *Journal of Geophysical Research: Solid Earth*, 116(B12), 2011.